

The design and lifetime calculation of MHD generator walls based on subcritical crack growth in ceramics

Citation for published version (APA):

Lierop, van, H. R. M. (1992). *The design and lifetime calculation of MHD generator walls based on subcritical crack growth in ceramics*. [Phd Thesis 1 (Research TU/e / Graduation TU/e), Chemical Engineering and Chemistry]. Technische Universiteit Eindhoven. <https://doi.org/10.6100/IR375704>

DOI:

[10.6100/IR375704](https://doi.org/10.6100/IR375704)

Document status and date:

Published: 01/01/1992

Document Version:

Publisher's PDF, also known as Version of Record (includes final page, issue and volume numbers)

Please check the document version of this publication:

- A submitted manuscript is the version of the article upon submission and before peer-review. There can be important differences between the submitted version and the official published version of record. People interested in the research are advised to contact the author for the final version of the publication, or visit the DOI to the publisher's website.
- The final author version and the galley proof are versions of the publication after peer review.
- The final published version features the final layout of the paper including the volume, issue and page numbers.

[Link to publication](#)

General rights

Copyright and moral rights for the publications made accessible in the public portal are retained by the authors and/or other copyright owners and it is a condition of accessing publications that users recognise and abide by the legal requirements associated with these rights.

- Users may download and print one copy of any publication from the public portal for the purpose of private study or research.
- You may not further distribute the material or use it for any profit-making activity or commercial gain
- You may freely distribute the URL identifying the publication in the public portal.

If the publication is distributed under the terms of Article 25fa of the Dutch Copyright Act, indicated by the "Taverne" license above, please follow below link for the End User Agreement:

www.tue.nl/taverne

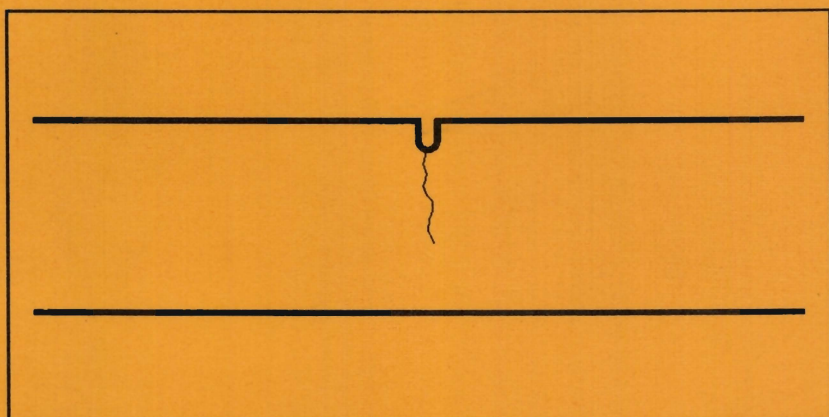
Take down policy

If you believe that this document breaches copyright please contact us at:

openaccess@tue.nl

providing details and we will investigate your claim.

The Design and Lifetime
Calculation of MHD Generator
Walls Based on Subcritical
Crack Growth in Ceramics



H.R.M. van Lierop

**The Design and Lifetime
Calculation of MHD Generator
Walls Based on Subcritical
Crack Growth in Ceramics**

The Design and Lifetime Calculation of MHD Generator Walls Based on Subcritical Crack Growth in Ceramics

PROEFSCHRIFT

ter verkrijging van de graad van doctor aan de
Technische Universiteit Eindhoven, op gezag van
de Rector Magnificus, prof. dr. J.H. van Lint,
voor een commissie aangewezen door het College
van Dekanen in het openbaar te verdedigen
op dinsdag 23 juni 1992 om 16.00 uur

door

Hubertus Renier Maria van Lierop

geboren te Weert

Dit proefschrift is goedgekeurd door de promotoren:

prof. dr. J.A. Klostermann

en

prof. dr. L.H.Th. Rietjens

Co-promotor:

dr. A. Veefkind

**CIP-GEGEVENS KONINKLIJKE BIBLIOTHEEK,
DEN HAAG**

Lierop, Hubertus Renier Maria van

**The design and lifetime calculations of
MHD generator walls based on subcritical
crack growth in ceramics/**

Hubertus Renier Maria van Lierop.

- [S.l. : s.n]. - Fig., tab.

Proefschrift Eindhoven. Met lit. opg., reg.

ISBN 90-9004009-9

NUGI 832

**Trefw.: magnetohydrodynamische generatoren;
keramiek.**

aan Marleen

**This work was performed as a part of research program of the group
Electrical Energy Systems of Eindhoven University of Technology,
The Netherlands.**

C O N T E N T S

i

SUMMARY	iv
SYMBOLS	vi

1. INTRODUCTION	
1.1 Background	1
1.2 State of the art on generator design	4
1.3 Present work	5
1.3.1 Construction	5
1.3.2 Material properties	6
1.4 MHD generator wall requirements	7
1.5 Wall materials for the designed construction	11
1.6 Wall construction	13
1.7 Ceramic material description	14
1.7.1 Reaction Bonded Silicon Nitride	14
1.7.2 Aluminium oxide	15
1.7.3 Fibers	15
1.8 Test design of modular wall segment	16
References	19
2. EXPERIMENTAL SET-UP	
2.1 Introduction	21
2.2 Oven	22
2.3 Vibration generator	24
2.4 Interferometer	24
2.4.1 Michelson-interferometer	24
2.4.2 Application of the interferometer	25
2.5 Strain gauge measurement	27
2.6 Data-acquisition	30
2.6.1 Introduction to the data-acquisition	30
2.6.2 Data-acquisition by the CAMAC-crate	31
2.6.3 Data-acquisition by hand	33
References	33

3. MODELLING	
3.1 Introduction	35
3.2 Dynamic behaviour	36
3.2.1 Modelling of the dynamic behaviour	36
3.2.2 TUTSIM modelling	36
3.2.3 Coupled differential equations	39
3.3 Thermal modelling	40
3.4 Crack growth modelling	45
3.4.1 Subcritical crack growth	45
3.4.2 Crack velocity versus stress intensity	46
3.4.3 Subcritical crack growth under static load	48
3.4.4 Subcritical crack growth under increasing load	50
3.4.5 Subcritical crack growth under cyclic load	53
3.5 Finite element methode	58
3.6 Problablistic modelling	59
3.6.1 Stress volume integral	59
3.6.2 Algor stress volume integral	63
3.6.3 Algor stress surface integral	64
3.6.4 Lifetime calculations	66
References	74
4. MEASUREMENTS	
4.1 Introduction	77
4.2 Results of lifetime-measurements	78
4.3 Dynamical behaviour of the wall segment	86
4.4 Thermal measurements	88
4.5 Grinding	89
4.6 Proof tensile tests	91
4.7 Vickers indentation and saw slit	92
4.7.1 Vickers indentation	92
4.7.2 Saw slit	94
4.8 Thermal and chemical attack of RBSN	96
4.8.1 Description of problem	96
4.9 Forces on the bolt	102
4.9.1 Thermal expansion	103
4.9.2 Bending moment tests	104
4.9.3 Screw-thread	106
4.9.4 Constructions to decrease the transverse force	107
References	111

5. CONCLUSIONS	112
Appendix A	115
Appendix B	116
Appendix C	120
Appendix D	122
Appendix E	129
Appendix F	132
Samenvatting	138
Dankwoord	140
Curriculum vitae	141

SUMMARY

An analysis has been made of the requirements of the walls of closed cycle MHD generators. One of the requirements is that, in order to obtain a low heat flux through the wall, the inner wall should be able to withstand a high temperature. Ceramics can be used as inner wall materials. A number of ceramics, which can be used, is presented. Combination of the possibilities of the ceramics and of the requirements for the wall resulted in a pre-design of a module of a MHD generator wall. The design is based on a modular construction of the MHD wall. Each modular wall segment consists of an inner wall tile, a thermal resistant layer, a cooling layer and a supporting construction. The inner three layers are connected to each other by means of a ceramic bolt. A model of such a wall segment has been made. The model, with the ceramic bolt, as a critical part of the construction, has been subjected to lifetime tests.

To perform the lifetime tests a test-rig has been built. The test-rig consists of a number of systems, each with its own specific purpose. An oven has been built to expose the wall segment to the "MHD temperature". A vibration excitator has been used to simulate the mechanical load on the bolt. By means of a strain gauge system and a laser-interferometer the mechanical load has been measured. To acquire and to process the measured data two computer systems have been coupled.

A model has been presented by which the lifetime of a ceramic bolt can be calculated. Before the lifetime can be calculated, the stress distribution in the bolt has to be known first. Because the Youngs moduli are temperature dependent, it is necessary to calculate the temperature distribution before the stress distribution can be calculated. For the calculation of the temperature distribution a model has been presented. The mechanical load on the bolt consists of a cyclic load superimposed on a static load. A model has been presented to calculate the dynamical load. At this point it is possible, by means of a finite element method, to calculate the stress distribution in the bolt. The model by which the lifetime of the bolt can be calculated is based on a known relation to describe the subcritical crack growth in ceramics. The model to describe the subcritical crack growth under constant load has been extended over a quasi-static load to a dynamic load. By means of the dynamical model it is possible to calculate the lifetime of construction elements subjected to a dynamical load. To simplify the calculation of the dynamic lifetime an

effective stress is introduced. According to the quasi-static crack growth model, the parameters describing this growth, can be deduced from the results of experiments in which the rates of stress increases are varied significantly. A stress volume integral and a stress surface integral has been presented by which the allowable stress can be determined, based on the material data of the manufacturer. The lifetime of a generator wall has been calculated. For this calculation different constructions have been compared. The influence on the lifetime of the material data and of the testing method has been determined.

For a number of bolts the lifetime has been measured at 1773 K and at a mechanical load. Initially most bolt broke at a very low stress and at unexpected places. Further research has been performed on the composition of the ceramic to explain the low failure stress. Two different solutions have been applied to let the bolt breake at the expected place. First the saw slit, at which the bolt should breake, has been deepened and sharpened. Secondly, three systems have been added to the wall segment to decrease the transverse force on the bolt. From an analysis it appeared that the bending stress in the bolt, as a result of these transverse forces, is sometimes larger than the applied tensile stress. A leaf spring system, a ball-and-cup system and a universal joint have been added to decrease the transverse forces. At 1573 K and with the above systems the bolts broke at the saw slit and at much higher stresses. From the results of the quasi-static measurements, the crack growth parameters were determined. The measured lifetimes of the dynamically loaded bolts showed a large spread around the expected lifetime.

SYMBOLS

symbol	description	units
A	amplitude	[-]
A	crack growth constant	[-]
A	surface	[m ²]
B	magnetic field	[T]
B	stress increase velocity	[Pa/s]
C	stiffness	[N/m]
E	electrical field	[V/m]
E	Youngs modulus	[Pa]
F	force	[N]
I	current	[A]
I	surface inertness moment	[m ⁴]
K	total heat conduction factor	[W/K]
K _I	stress intensity factor mode 1	[N/m ^{3/2}]
K _{Ic}	critical stress intensity factor mode 1	[N/m ^{3/2}]
M	mass	[kg]
P	failure probability	[-]
Q	activation energy	[J/mol]
R	gas constant	[J/molK]
R	heat resistance	[K/W]
R	resistance	[Ohm]
S.S.I.	stress surface integral	[-]
S.V.I.	stress volume integral	[-]
T	temperature	[K, °C]
U	velocity	[m/s]
U	voltage	[V]
V	volume	[m ³]
Y	shape factor of crack	[-]
a	acceleration	[m/s ²]
a	crack length	[m]
d	damper	[kg/s]
e	excentricity	[m]
h	height	[m]
l	length	[m]
m	Weibull modulus	[-]
n	crack growth exponent	[-]
n	refractive index	[-]
p	pressure	[Pa, Torr]
q	heat flux	[J/s]
q	heat flux	[w/m ²]

r	radius	[m]
s	position	[m]
t	time	[s]
u	outer fibre distance	[m]
v	velocity	[m/s]
x	position	[m]
z	position	[m]
δ	distance	[m]
λ	heat conduction coefficient	[W/mK]
λ	wave length	[m]
ϕ	humidity	[%]
ϕ	angle	[rad]
ϕ	angle	[rad]
ω	angular velocity	[rad/s]
η	efficiency	[-]
σ	stress	[Pa]
μ	Poisson ratio	[-]
ϵ	strain	[-]

1 INTRODUCTION

1.1 Background

The problematic nature of the conversion of energy from one form to another is supported by a broad field of research and engineering activities. At present the production of electrical energy requires not only the application of new energy sources and alternative conversion processes but also the application of sophisticated purification units to minimize the environmental pollution. The most common process to produce electrical energy is the conversion of chemical energy of fuels into electricity by means of a thermal process. According to Carnot the maximum attainable efficiency of such a process is given by

$$\eta_c = 1 - (T_1/T_2) \quad (1.1)$$

T_2 is the temperature at which thermal energy is supplied to the process and T_1 is the temperature at which the thermal energy is carried of. The conventional way to convert the heat into electrical energy on a large scale is by using a steam power plant. The steam turbine inlet temperature T_2 is limited to a value of 800 K. The temperature T_1 is the temperature of the cooling water which is about 300 K. The Carnot efficiency of this steam power plant is 63 %. Due to thermal and mechanical losses the efficiency of an advanced steam power plant reaches a value of 40 % [ref. 1.1].

Increasing the efficiency of the conversion process will reduce the consumption of fuel (coal, oil, gas). It will also reduce the environmental pollution (heat, flue gas). The efficiency of these steam power plants can be increased by increasing the inlet temperature of the turbine. An increase of 50 K has only a small influence on the Carnot efficiency and on the overall efficiency. If a Magneto Hydro Dynamic (MHD) topping cycle is used in combination with a conventional steam cycle it is possible to increase the Carnot efficiency significantly from 63 % to 85 or 89 %. An overall efficiency of 50 % can be achieved [ref. 1.2, 1.3]. The two MHD systems most used are the open system ($T_2=2700$ K) and the closed system ($T_2=2000$ K). In both systems the conversion process is based on the fact that a Lorentz force is acting on a moving conductor (ionized gas) in a magnetic field (fig. 1.1). This Lorentz force will

separate the charged particles in the gas which results in an electrical field in the generator. By means of electrodes and a load, electrical energy can be extracted. In a power plant the load is replaced by a power extracting system which delivers the generated electrical power to the grid.

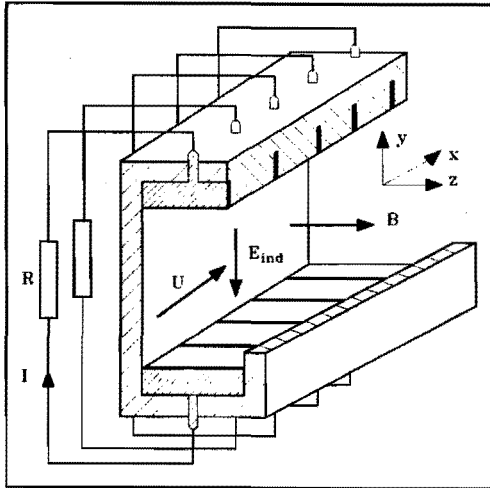


Figure 1.1 Principle of the MHD proces. Gas velocity U , magnetic field B , induced electrical field E_{ind} generated current I and load R .

In the open cycle MHD generators (fig. 1.2) the working medium consists of the gaseous fuel combustion products. The combustion products, at a temperature of 2700 K, are seeded with an alkali metal to obtain a plasma with sufficiently high electrical conductivity. After leaving the MHD generator the plasma is used to produce steam for a conventional steam power plant.

In a closed cycle MHD generator an alkali seeded noble gas is used as a working medium. After leaving the MHD generator the gas passes a heat exchanger between the topping cycle and the steam turbine. The gas is recompressed and fed back to the heat source, the primary heat exchanger. In this type of generators the gas temperature can be approximately 700 K lower than in open cycle generators because of the effect of non-equilibrium ionization [ref. 1.4]. By means of non-equilibrium ionization, the electrons in the gas can reach a higher temperature than the surrounding gas. The electrical conductivity of the medium used in these systems reaches the same values as that in the hotter open systems.

The MHD research program at the Eindhoven University of Technology has been concentrated on closed cycle MHD conversion. In 1975 an enthalpy extraction of 20 % was reported as result of shock tube experiments with linear generators [ref. 1.5]. This shock tube facility is able to produce a stagnation

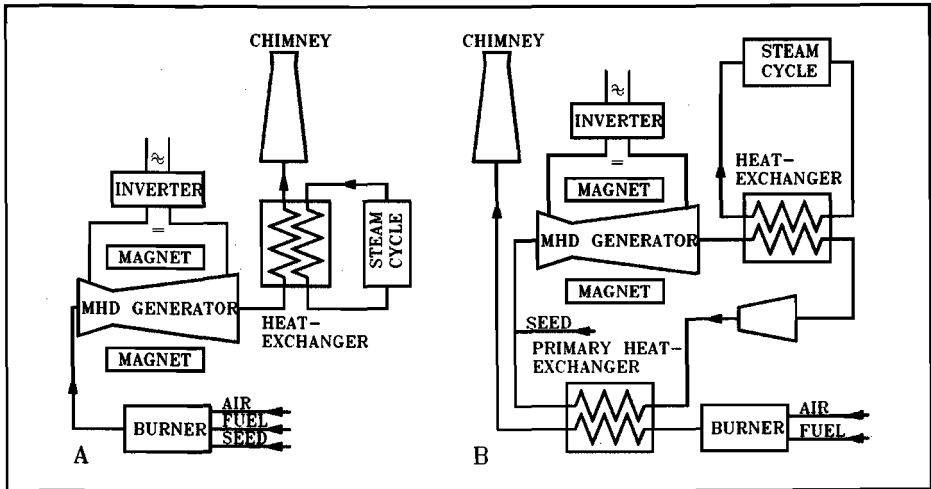


Figure 1.2 Open cycle (A) and closed cycle (B) MHD topping systems in combination with steam cycles.

temperature of 3000 K and a magnetic field of 3.5 T. The test time is limited to 5 ms. In 1986 an enthalpy extraction of 13% was reported as result of blow down experiments [ref. 1.6]. The blow down facility could produce a stagnation temperature of 2000 K and a magnetic field of 5 T. The test time was 10 seconds. For both experiments linear MHD generators, with a nominal electrical output of 1MW_{el} , have been used. The generators are channels with a mean inner cross section of $10 \times 10 \text{ cm}^2$ and a length of 80 - 100 cm.

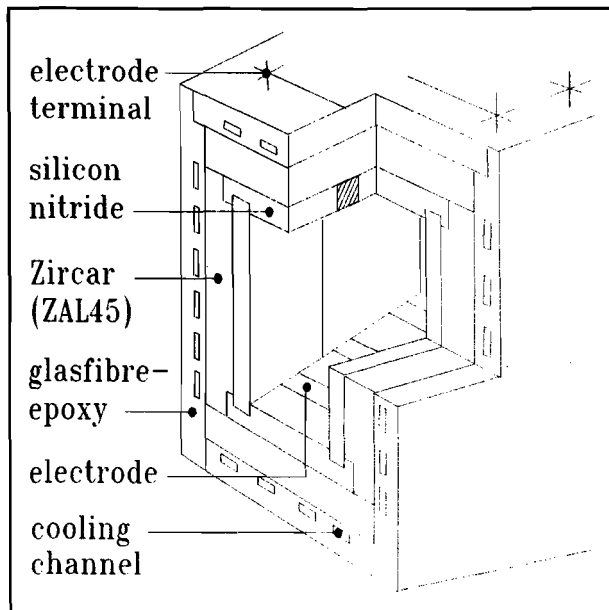


Figure 1.3 View into a MHD generator with shape closed inner walls. The ceramic tiles of the side walls are kept in place by means of grooves in the inter electrode ceramic strips.

In noble gas MHD generators the current density is not uniformly distributed, but concentrated in arcs, which are called streamers [ref. 1.7]. These streamers move downstream the generator with approximately the gas velocity. In and around the streamers there is a pressure gradient [ref. 1.8]. These moving pressure gradients exert fluctuating forces on the generator walls. In the blow down channels the fluctuating forces are supported by the design of the inner ceramic tiles of the generator. These tiles make up a shape closed construction which is embedded in prestressed fiber insulating material (fig. 1.3).

1.2 State of the art on generator design

Nowadays large scale MHD generators are mainly designed with enforced cooling to keep the temperature of the wall low. Thermal losses through the wall up to 400 kW/m² are normal [ref. 1.9]. The low wall temperature permits the application of metal for the channel walls. The walls are built up of metal pegs of a frontal size of approx. 25x25 mm². Each peg has its own cooling channel. The pegs are mutual isolated by means of ceramic (boron nitride) washers. To reduce the heat flux through the wall a ceramic insert can be placed on top of the peg. Nowadays the inserts are replaced by a total ceramic covering of the peg. These small ceramic tiles are soldered to the copper cooling layer. Special attention is payed to the thermal stress free connection between the metal peg and the ceramic cover, figure 1.4 [ref. 1.10]. The combination of several pegs to a bar decreases the number of seals, which are possible sources of water leakages.

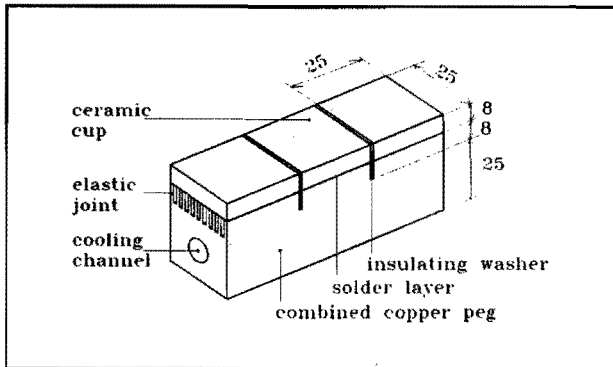


Figure 1.4 Copper pegs with ceramics cups soldered on elastic joints.

1.3 Present work

The aim of the present work is to compile information needed for the design of a segmented MHD generator. Large scale MHD generators ($P_{el} > 50$ MW) have to be built up with many tiles on the inner walls. The shape closed construction of figure 1.3 can not be applied to these generators due to the limited size of the available ceramic tiles and the large forces resulting from pressure fluctuations. The wall segment designed in this thesis is to be placed in insulating walls. They can also be used as inter-electrode walls.

In industrial application of MHD power systems the separate parts of the system have to meet a certain lifetime. For the first generation of MHD generator channels a lifetime of 1000 hours is acceptable.

The work described in this thesis can be divided in two main subjects, that is:

- design of a construction
- investigation of material properties.

1.3.1 Construction

Because of the large number of inner tiles a MHD wall will have, in our opinion, to be built modular. A number of tiles (inner layer) will be connected together with a thermal insulating layer to a cooling plate (fig. 1.5). A number of

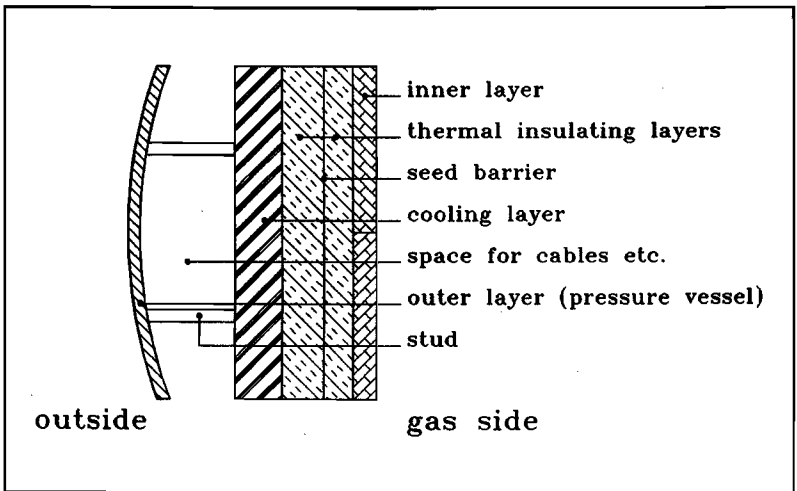


Figure 1.5 Cross section of part of a MHD generator wall, with the distinctive layers.

cooling plates, forming one wall of the generator, will be placed, together with the other walls, inside a pressure vessel. The space between cooling plate and pressure vessel can be used for the cables and the cooling system. The construction designed in this thesis covers only a small segment of the modular MHD generator wall. The modular segment (fig 1.11) has a frontal size of one tile. The thickness of the designed construction reaches only to the cooling layer. Since design criteria for pressure vessels are well known no further attention will be paid to this part of the construction. As will be explained in section 1.6 the tiles are connected to the cooling plate by means of ceramic bolts. To expose the segment to vibration (as explained in section 2.3), the inner tile is connected to the cooling plate by means of two bolts to prevent rotation of the inner tile. The connection by two bolts could cause some problems. Preventing these problems - related to thermal expansion - deepened the insight in the construction of a MHD generator wall. A number of tests have been performed in which the bending moment in the bolt, due to the thermal expansion, was measured. These tests were performed with and without the designed subsystems (universal joint, leafspring and ball-and-cup) which decreased the bending moment. To increase the stress in the bolt, by which the lifetime is decreased as explained in section 3.4, the diameter of the bolt shaft is locally decreased.

1.3.2 Material properties

For a critical part of this construction, the bolt, the lifetime is calculated based on the subcritical crack growth in ceramics and the available material data of the ceramics used. An existing crack growth model for constant load is transformed to describe the crack growth under a cyclic load. An effective stress is introduced to simplify the lifetime calculations for bodies under a cyclic stress. The available material data were not sufficient to perform the calculations. For the chosen material (section 1.6) no data were available on the subcritical crack growth. This data had to be measured. The best way to determine material data is to measure this data on simple objects. In the case of the subcritical crack growth properties, a bending bar ($3.5 \times 4.5 \times 50 \text{ mm}^3$) is often used. The stress distribution in such a bending bar is relatively simple and the bars are relatively cheap. With the modular wall segment, including the two bolts, it is also possible to measure these material data. The stress distribution in the bolts is more complicated than in a bending bar. The bolts are

more expensive and the total test set-up is more complicated. It was decided to measure the material data by means of the bolts of the wall segment. In this way it is possible to kill two birds with one stone. The construction could be tested and the material data could be measured.

The designed modular wall segment has been built. A test-rig has been built to expose the wall segment of a closed cycle MHD generator to a simulation of the combined thermal and mechanical load. Two diagnostic techniques have been developed to measure the mechanical load on the segment. These techniques will be described in detail in chapter 2. The designed wall segment is tested several times, with a number of the heaviest loaded part, the bolt, in the experimental set-up, to verify the developed model and to acquire more specific material data.

1.4 MHD generator wall requirements

MHD generator walls have to meet a number of requirements. Not all of these requirements can be met by one material. A generator wall can be built up of several layers. Each layer will be able to meet one of the requirements in particular, but all layers should be transparent to the magnetic field. Figure 1.5 gives an impression of the layered generator wall.

The requirements, for the plasma sided materials of the insulating walls, are summarized below:

- a - corrosion resistant
- b - high temperature resistant
- c - thermoshock resistant
- d - erosion resistant
- e - vibration resistant
- f - high electrical resistance.

a) Although the working medium of a closed cycle MHD generator is a noble gas there are some corrosive agents present. The first one is the seed, Cs, used to improve the electrical conductivity of the plasma. Small amounts of O_2 , N_2 , H_2O and CO_2 will be present as well. Little information is available on the influence of Cs on the strength and the crack growth mechanism of ceramics.

b) A good cooling system can decrease the wall temperature to very low levels (400 K). This cooling system will extract a high thermal power from the plasma. This power, at a low

temperature, can be used downstream in the steam cycle. By reducing the inner wall temperature, the use of metals as wall material, can be considered. In our opinion the wall temperature should be kept as high as possible to decrease the thermal losses from the generator. The first aim is to keep the wall temperature at a value of 1800 K.

c) During the start-up procedure of the generator the temperature increase per unit of time can be kept at a level prescribed by the materials used. During normal use there are some failures possible that will cause a thermal shock. A general failure of the burner will result in a temperature difference of 1500 K at the entrance of the primary heat exchanger (fig. 1.2). Due to the thermal mass of this heat exchanger the thermal shock in the generator will be 200 K/min [ref 1.11]. A general failure in the magnet will result in an instantaneous reduction of the extracted power. This will, at the downstream part of the generator, result in an instantaneous increase of the temperature, with a value of 500 K [ref. 1.11]. A segmented Faraday generator is equipped with a number of inverters. A general failure in one of these inverters will only result in a small change in extracted power and in the plasma temperature. A Hall generator has only one inverter. A general failure in this inverter has the same effect as a failure in the magnet.

d) It is possible that small solid particles in the high temperature heat exchanger will get loose from the wall. These particles will flow through the generator and may cause erosive degradation of the generator wall. No values for the number of particles or the hardness of these particles are available at this time.

e) In closed cycle MHD generators the current flows through contracted channels called streamers. The streamers do not fill the entire generator. In and around these streamers there is a pressure gradient. The streamers and pressure gradients pass the generator with approximately the gas velocity. The inner wall is subject to a fluctuating pressure which will result in vibration of the inner wall [ref. 1.12].

f) The designed wall segments, which are described in this thesis, are to be placed between the positive and negative electrode walls. An electrical conducting wall between these electrode walls would short circuit the generated power inside the generator. No external power would be generated. The insulating wall, at its working temperature, should have a

high electrical resistance to minimize the internal leakage currents.

The cold outer side of the generator has to meet the following requirements:

- a - withstand the system pressure
- b - be gas tight.

a) The system pressure of a MHD generator will be 1.2 MPa. In normal use the pressure will decrease to a value of 80 kPa at the end of the channel. To make a safe design the pressure throughout the generator will be supposed to be the system pressure of 1.2 MPa.

b) Although there might be a gas tight layer between the inner wall and the outer wall, as a redundancy the outer wall will be made gas tight as well.

Between the inner layer and the outer layer there will be two more layers each with their specific properties. The most important property of the second inner layer will be the thermal resistance. The main property of the next layer will be the possibility to cool.

Requirements for the thermal resistant layer are the following:

- a - thermal insulating
- b - corrosion resistance
- c - electrical resistance
- d - seed barrier
- e - creep resistance.

a) The materials available for the inner layer have a relative high thermal conductivity to prevent thermal stresses. The heat flux from the plasma to the cooling layer should be reduced to an acceptable level ($q = 40 \text{ kW/m}^2$). To reach this low heat flux a thermal insulating layer is needed.

b) The hot gas in the generator can penetrate into the thermal insulating layer by way of the thermal expansion slits between the inner wall segments. Carried in this gas are particles of the seed. The seed can attack the physical properties of the insulating material.

c) Since the plasma can reach the thermal insulating layer, this layer has to have a high electrical resistance to decrease the internal leakage currents.

d) At a certain depth into this layer the seed will condense. If this condensed seed can form an electrical conductive trace between the two electrode walls, there will be again internal leakage currents. To prevent this condensation of the seed, the thermal resistant layer should include a cesium barrier. The cesium barrier should be located at a place in the layer where the temperature is above the condensation temperature of the seed.

e) For large scale MHD generators the walls will be built up of many tiles. Each tile will be connected by means of a bolt to the outer wall. To ensure a positive contact between the several layers, the tiles must be preloaded. During the lifetime of the generator, the preload should not be reduced below the pressure fluctuation. Creep of the thermal insulating layer is a possible cause of the decrease of this preload.

Requirements for the cooling layer are the following:

- a - corrosion resistancy
- b - electrical resistant
- c - water tight
- d - gas tight.

a) If the seed barrier, in the thermal resistant layer, failed the condensed seed can reach the cooling layer. If no other provision is taken the cooling layer has to be made of seed resistant material.

b) Through the condensed seed the conducting plasma can reach the cooling layer. To prevent internal short-circuiting the cooling layer has to be made out of material with a high electrical resistance.

c) The cooling medium will be water. Diffusion of water through the cooling layer into the thermal insulating layer will reduce the thermal insulation properties of this layer. Contamination of the plasma with more than 500 ppm water will stop the MHD conversion process [ref. 1.13].

d) Along the generator length, during normal use, the pressure decreases from 1.2 MPa to 80 kPa. The pressure in the pressure vessel enclosure is constant along the generator length. To prevent the plasma to flow in the volume between the cooling layer and the pressure enclosure, from generator inlet to the generator outlet, the cooling layer has to be gas tight.

1.5 Wall materials for the designed construction

To choose the materials for the separate layers a number of considerations has to be made. The chosen materials have to meet the requirements, mentioned in the above chapter, for the specified layer. The chosen materials have to be easily machinable, or to be delivered in net shape. To be independent from manufacturers, the materials have to be made by several manufacturers, free available on the world market and ought to be certified by the manufacturers. The material, should not be harmful to mankind. Experience in the use of certain materials is often, and will be in this case, of great influence on the choice. Research in the field of high tech ceramics will, in

Table 1.1 Comparison of applicable MHD wall materials. The property of a material to meet a certain requirement is indicated by --, -, 0, +, ++, ranging from bad to good.

	<i>corrosion resistance</i>	<i>electrical resistance</i>	<i>allowable temperature</i>	<i>thermal shock resistance</i>	<i>strength</i>
<i>Boron Nitride</i>	0	++	++	++	0
<i>Reaction Bonded Silicon Nitride</i>	0	++	+	+	+
<i>Hot-Pressed Silicon Nitride</i>	+	++	0	++	++
<i>Aluminum Oxide</i>	0	++	+	0	++
<i>Silicon Carbide</i>	+	--	++	++	++
<i>Zirkonium Oxide</i>	0	--	+	0	++
<i>Fibrous Alumina</i>	--	++	+	++	-

future, influence the choice made hereafter. Present research in the field of developing cesium resistant coatings has influenced the choices. Data of the ceramics used are given in appendix A. A number of applicable materials are compared in table 1.1.

Inner layer.

A number of requirements for the inner layer are intrinsically related to the material properties. High temperature resistance and thermoshock resistance are some of these material properties. Corrosion-, erosion- and electrical resistance of the material can, if necessary, be improved by a number of coatings. Since cesium barrier coatings are studied in an other group, our selection procedure is based on the temperature and thermal shock properties of the material in combination with electrical properties and own experience. As a result of these considerations it is decided to use Reaction Bonded Silicon Nitride (RBSN) as the material for the inner wall layer.

Outer layer.

The outer layer will be made out of stainless steel 316.

Thermal resistant layer.

For the thermal resistant layer ZAL 45 from ICI is chosen. This is an alumina fiber board with high thermal insulating properties. It is relatively strong. The corrosion resistance of this material must be improved by a coating. Special attention has to be paid to the ability of the coating to follow the thermal expansion of the material. Since this material has a large shrinkage at high temperatures it should be pre-shrunk before machining to net shape.

Cooling layer.

We have chosen to use glass fibre reinforced epoxy as the material for the cooling layer. This material has to be protected by a coating (e.g. RTV silicone of GE) from the seed. By orientating the glass fibers parallel to the inner wall, a good water tight construction can be achieved.

1.6 Wall construction

The various layers of the wall have to be attached to each other to make up the desired wall construction. The separate layers can be glued or cemented together. For high temperature application there is a broad range of cements available from AREMCO. Until now no information on the long term behaviour of these cements in MHD applications nor on the dynamic strength of the insulating material is available. Our design proposal is to clamp the inner three layers (fig. 1.4) together by means of a ceramic bolt. Because it is not possible to produce tiles of the height of the channel, the inner layer is divided in small tiles. Bending forces in large tiles will exceed the strength of the material. Expansion slits between the tiles should be provided to accept the thermal expansion. There may be other ways, to attach the large number of inner tiles to the cooling layer, which can insure a positive contact force between the several layers, but we will further work out our design proposal. The positive force is needed to prevent hammering of the inner tiles which results from the pressure fluctuations in the channel. If during any time, of these fluctuations, there will become a clearance between the several layers, the force at moment of renewed contact, will exceed the normal force, depending on the stiffness of the construction [ref. 1.14]. This is called hammering.

We have chosen RBSN as the material for the bolt since RBSN has some properties which makes it an attractive material.

These properties are the following:

- constant maximum allowable stress until 1800 K
- constant stress intensity factor until 1800 K
- there is no glassy phase in the material
- it can be delivered at net shape.

Its relatively low strength can be regarded as negative property.

This bolt will be the subject of major interest in this thesis. For the bolt the lifetime will be calculated using the material data delivered by the manufacturer and the data resulting from the experiments. In several tests this lifetime will be verified. The pressure forces on the cooling layer are transformed to the outer layer (the pressure vessel) by means of studs or ridges (fig. 1.5).

1.7 Ceramic material description

1.7.1 Reaction Bonded Silicon Nitride

The production process of reaction bonded silicon nitride is performed at atmospheric pressure. Pure silicon compacts, with a binder, are formed at or close to the final shape. These compacts are reacted in a nitrogen atmosphere at temperatures up to 1770 K for times varying from 2 - 5 days depending on the size of the component. Nitriding below 1670 K results in α - Si_3N_4 . Nitriding above this temperature results in β - Si_3N_4 . A normal composition is 60 % α - Si_3N_4 , 40% β - Si_3N_4 and 2 % Si [ref. 1.15]. Partially nitrided compacts (green compacts) can be machined with normal workshop tools. After machining to net shape the compacts are then nitrided to 100 %. Shrinkage due to the elimination of the pores is closely matched by the volume expansion of silicon to silicon nitride. The net volume shrinkage can be less than 0.05 % which enables net shape forming of the green bodies. Densities of reaction bonded silicon nitride varies from 2.3 - 2.65 g/cc. The porosity of the material is approximately 20 %. A mean pore-size of 20 μm is given (fig. 1.6). Most pores are smaller, but isolated pores up to a size of 500 μm were found (fig. 1.7). Due to the process (the gaseous nitrogen has to penetrate into the silicon compacts by the pores) the maximum wall thickness is limited to 12.5 mm. Due to the variation of pores and other defects in the material, the strength properties of reaction bonded silicon nitride are expressed as Weibull distributions. The strength figures are derived from three- or four point bend tests. The kind of test, the density of the material, the machining of the testpiece, the volume of the testpiece and the heat treatment of the testpiece have an influence on the measured strength. Oxidation of the material at high temperature would result in higher strength at room temperature due to the formation of a layer of silicon oxide, with a larger volume which results in a compressive stress at the surface [ref. 1.16]. The strength as well as the critical stress intensity factor of reaction bonded silicon nitride are almost constant over the temperature range of 300 - 1770 K.

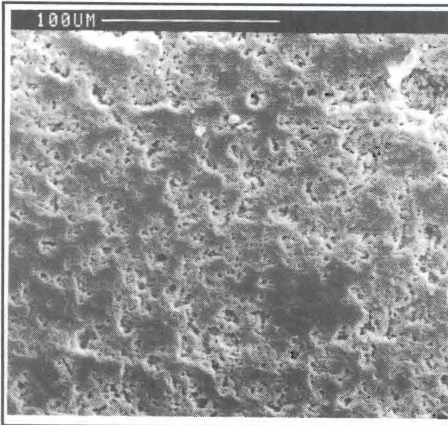


Figure 1.6 Reaction bonded silicon nitride of AME, normal pore size.

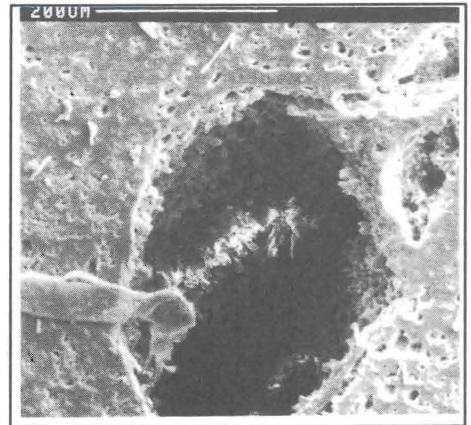


Figure 1.7 Reaction bonded silicon nitride of AME, large pore size.

1.7.2 Aluminium oxide

To increase the density of the sintered alumina a pressure can be applied during the process. Pure alumina powder particles are mixed with a sintering aid (MgO or ZrO_2). Under high pressure up to 4 GPa and at temperatures up to 1800 K alumina compacts are sintered to final density. It is not possible to make a green body which can be machined. After sintering, the machining to net shape has to be performed with diamond tools. There is no limitation to the thickness of the material. During sintering the shrinkage of the compact is 5 - 20 %. The porosity of the final product can be up to nil % (fig. 1.8). In high purity alumina the content of the sintering aid will be less than 0.5 %. Due to this sintering aid the strength of alumina decreases above the melting temperature of the reaction products of the sintering aid. The material data of alumina also have to be given as a Weibull distribution.

1.7.3 Fibers

The fibers for the insulating material are made by a spinning process. Droplets of alumina fall onto a rotating disc. By means of the centripetal force they leave the disc forming a fiber. Outside the cylinder the molten fibers are solidified by a gas stream. The fiber diameter is 3 μm . Fibers, mixed

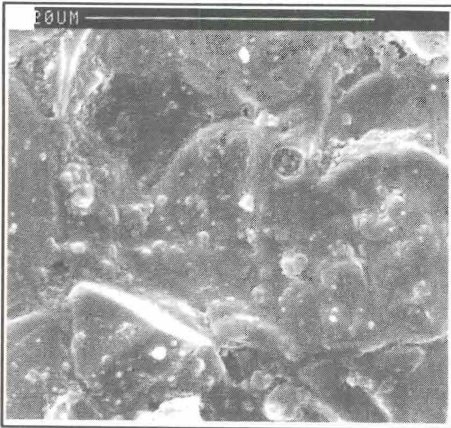


Figure 1.8 Aluminium oxide ceramic of ESK.

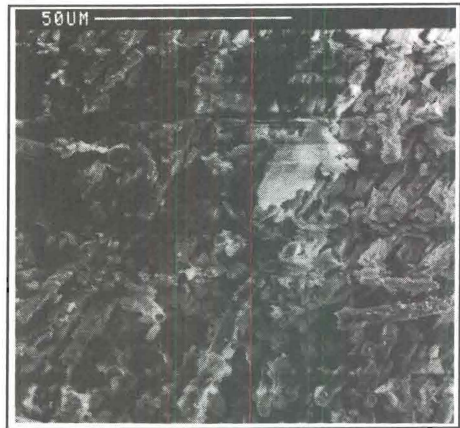


Figure 1.9 Alumina based fibrous insulating board, Zal 45 of ICI.

with an organic binder form an alumina blanket. The blanket is compressed to form the alumina board (fig. 1.9). By a firing procedure the organic binder is removed.

1.8 Test design of modular wall segment

A schematic overall drawing of the test-rig is given in figure 2.1. The excitator, coupling beam, wall segment and oven can be seen in figure 1.10. The segment design is given in figure 1.11. A drawing of the measuring cylinder will be given in figure 2.6. The leafspring system is explained in more detail by figure 4.39. The numbers of some parts, (between brackets) used hereafter, correspond with a figure number and the position number within that figure. The frontal size of the test-piece is taken to be $125 \times 200 \text{ mm}^2$. The inner three layers of the wall will be used in the testpiece. The effect of the pressure vessel is neglected. The inner layer (11.7) should be made out of RBSN. This material can only be produced with a thickness of 12.5 mm. The mass of the inner layer will be used to simulate the vibrating load (section 2.3), due to the pressure fluctuations, on the bolt. Since a RBSN tile of $125 \times 200 \times 12.5 \text{ mm}^3$, in combination with the excitator, can not simulate this load we have chosen to use alumina as a tile material. This tile has a thickness of 25 mm. To obtain a heat flux of 40 kW/m^2 through the wall, the thickness of the insulating layer (11.8 11.9 11.10) has to be 32 mm. This value is calculated using and extrapolating the material properties indicated by the manufacturer. These properties will be verified (chapter 3 & 4).

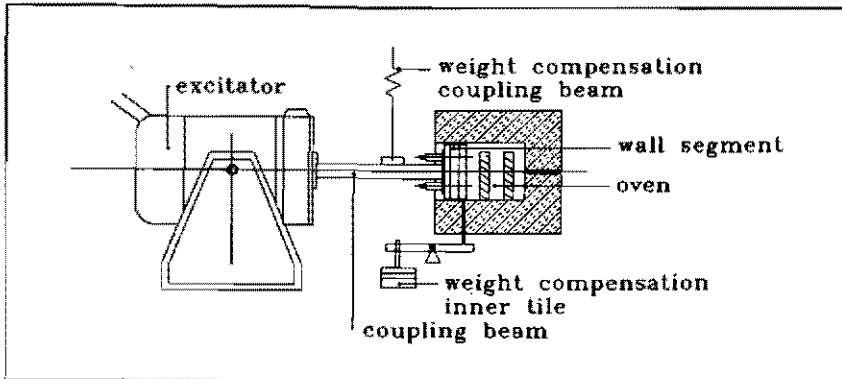


Figure 1.10 Schematic overview of excitor, coupling beam, wall segment and oven.

The cooling layer consists of a 16 mm thick and a 8 mm thick plate of glass fiber reinforced epoxy. The 16 mm thick plate (11.11) has to transmit the pressure forces to the studs. Grooves (11.4) are machined in the thin plate (11.11). Water, as a cooling medium, flows through these grooves. A thin wall between cooling medium and insulating fiber permits the desired heat flux to flow through the epoxy without exceeding the allowable temperature of this material.

By means of two RBSN bolts (11.6) these layers are connected to the end-plate of the coupling beam to an excitor. The pressure fluctuations in the MHD generator will be simulated by means of the vibration generator. We have chosen to use two bolts to prevent the inner tile from rotating. The weight of the inner tile is balanced. This will reduce transverse forces on the bolts. On the cold side of the construction, the bolts are lengthened to accept a force measuring system (11.14). To provide a fine control of the applied force, a steel cylinder (11.17) with fine screw-thread is glued and clamped to the end of each bolt. To make sure that no bending moment is introduced at the end of the bolts, cardanic joints (11.2) are placed between the force measuring systems and the endplate (11.3) of the coupling beam (11.16). The leaf spring system (11.13) at the cold side and the ball and cup (11.5) at the hot side reduce the bending moment as well. Over a length of 20 mm the diameter of the bolt is reduced to increase the tensile stress to a range which will decrease the lifetime significantly.

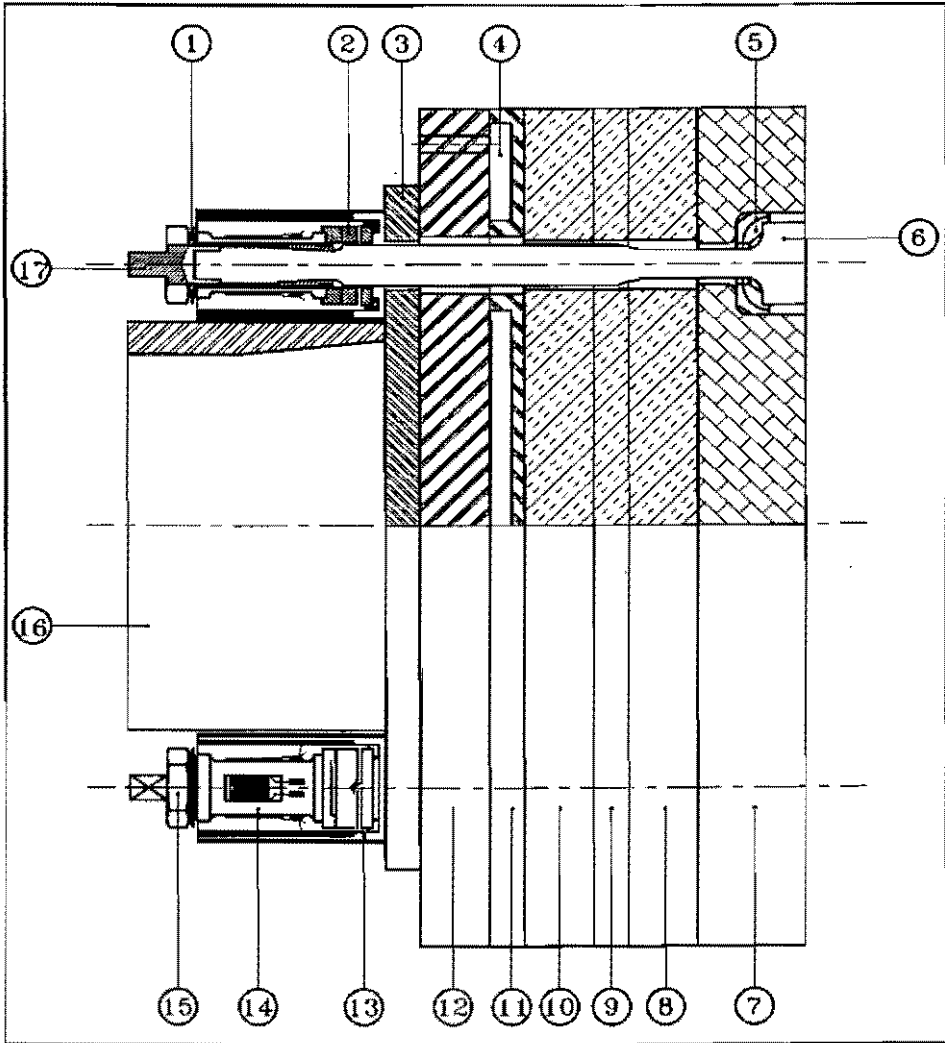


Figure 1.11 Cross section of the designed wall segment with testbolts.

Description of the parts of the testpiece of figure 1.11.

no.		no.	
1	steel spring washer	10	Zal 45 board
2	cardanic joint	11	glasfibre/epoxy board
3	end plate	12	glasfibre/epoxy board
4	water cooling channel	13	leaf spring system
5	ball-and-cup	14	measuring tube
6	silicon nitride bolt	15	nut
7	alumina tile	16	coupling beam
8	Zal 45 board	17	thread clamp
9	Zal 45 board		

References chapter 1

- 1.1 Rietjens L.H.Th., "Status and perspectives of MHD generators", Physics Bulletin 39, nr. 7, 1983, p.207.
- 1.2 Seikel G.R., e.a., "A summary of ECAS performance and cost results for MHD systems", Proc. of the 15th Symp. on Eng. Asp. of MHD, Philadelphia (PA), 1976, p. III.4.1.
- 1.3 Masee P. e.a., "Predesign of an experimental (5-10 MW_t) disk MHD facility and prospects of commercial (1000 MW_t) MHD/steam systems", Eindhoven University of Technology, Eindhoven, 1990.
- 1.4 Kerrebrock J.L., "Conduction in gases with elevated electron temperature.", 2nd Symp. on Eng. Asp. of MHD, Philadelphia (PA), 1961, p.327.
- 1.5 Blom J.H., e.a., "High power density experiments in the Eindhoven shock tunnel MHD generator", Proc. of the 6th Int. Conf. on MHD Electrical Power Generation, Washington (DC), 1975, p. III.73.
- 1.6 Balemans, W.J.M. e.a., "High enthalpy extraction experiments with the Eindhoven Blow-Down facility", Proc. of the 9th Int. Conf. on MHD Electrical Power Generation, Tsukuba, 1986, Vol. II, p. 330.
- 1.7 Wetzler, J.M., "Spatially resolved determination of plasma parameters of a noble gas linear MHD generator", PhD thesis, Eindhoven University of Technology, 1984.
- 1.8 Bosma, J.C.N., "Gasdynamics effects in linear MHD generators", PhD thesis, Eindhoven University of Technology, 1987.
- 1.9 Okuo, T. e.a., "Improvement of SiC - CuG - Cu insulator performance in MHD generator channels" , Proc. of the 27th Symp. Eng. Aspects of Magnetohydrodynamics, Reno, Nevada, 1989, p. 5.1.1-5.1.12
- 1.10 Petty, S.W. e.a., "Prototypical channel design and material studies", Proc. of the 27th Symp. Eng. Aspects of Magnetohydrodynamics, Reno, Nevada, 1989, p. 6.4.1-6.4.11.

- 1.11 Buter, J.E., "Ontwerpstudies CC MHD generatoren", F.D.O. Eng. Cons., Amsterdam, 1983.
- 1.12 Rietjens, L.H.Th., "Onderzoek MHD Blow-Down generator", Eindhoven University of Technology, 1984.
- 1.13 Veldhuizen, E.M. van e.a., "Methods and Results of Diagnosis in a Closed-Cycle Blow-Down Generator", Journal of Propulsion and Power, vol. 3, p.542-551, 1987.
- 1.14 Hoek, W. van der, "Het voorspellen van het dynamisch gedrag en positioneringsnauwkeurigheid van constructies en mechanismen", Technische Hogeschool Eindhoven, 1984.
- 1.15 Edington J.W. e.a., "The Mechanical Properties of Silicon Nitride and Silicon Carbide, part 1", Powder Metallurgy International vol.7, no. 2, 1975.
- 1.16 Wolf, L. Internal report, Eindhoven University of Technology, 1987.

2 EXPERIMENTAL SET-UP

2.1 Introduction

The most realistic way to test MHD generator walls is to place them in a MHD generator and to expose them to the working gas and temperatures of a real MHD system. This is a realistic but expensive way of testing. Another good way to test the wall segments is to build a test-rig in which several of the MHD conditions can be simulated. An overall view of such a set-up is given in figure 2.1. In the set-up it is not possible to simulate all the conditions of the generator.

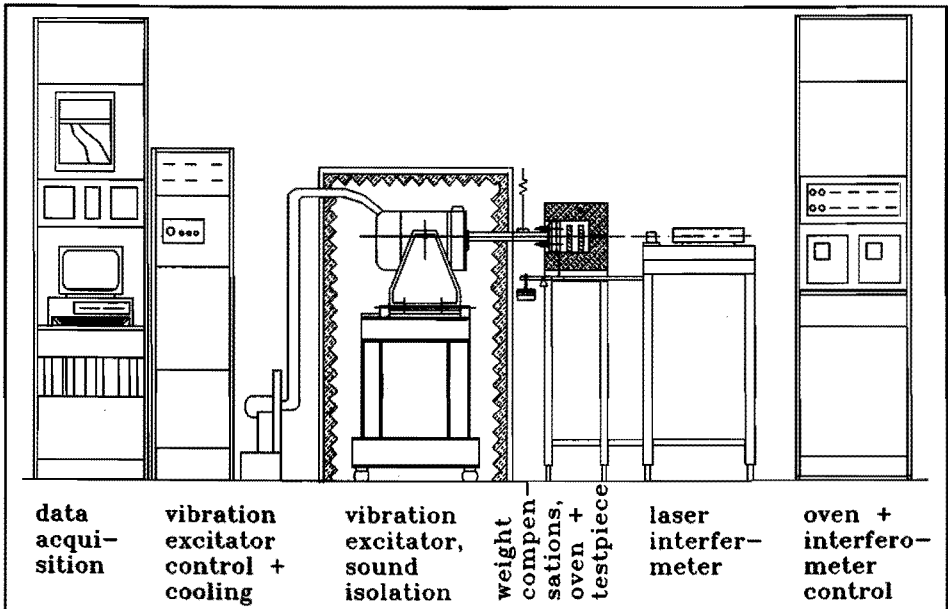


Figure 2.1 Schematic view of the test rig.

In a real MHD generator the wall segments will be exposed to a variety of loads, as described in chapter 1. These loads are the following:

- thermal
- electrical
- gas tight
- mechanical
- corrosive
- erosive.

It is decided to simulate, in the test-rig, the thermal and mechanical load on the wall segment. The segment will not be exposed to electrical arcs. The reactive cesium in an argon

cesium mixture as the atmosphere in the oven will not be used. For the experiments the alumina insulating materials can be used in the oven [ref. 2.1]. An argon purge will be used along the testbolts to minimize oxidation. The thermal load on the segment will be simulated by means of an oven. The oven is described in section 2.2. The fluctuating mechanical load on the wall segment will be simulated by means of the inertial force of an accelerating heavy plate. The vibration excitator to produce this acceleration is described in section 2.3. The mechanical load on the testpiece will be measured by means of two different systems. The first system is an interferometer which measures the acceleration of the heavy plate. This system is described in section 2.4 and appendix B. The second system is a strain gauge system which measures the forces in the testbolts. Section 2.5 describes the strain gauge system. The data from both measuring systems and from thermocouples in the oven are acquired by means of a computer system. This system is described in section 2.6.

2.2 Oven

The heat input, into a MHD wall segment, can be simulated in various ways. Possible heating systems are:

- an infrared radiation source
- a natural gas burner
- an electrical oven.

For the ease of control it is chosen to heat the wall segment by means of an electrical oven. The wall segment should not be placed inside the oven but it should be incorporated as part of the wall of the oven. Most commercial available ovens are constructed in such a way that the heating system is part of the wall. Such an oven can not be used. So we designed and built our own oven. The requirements are the following:

- an inner wall (testpiece) temperature of 1500 °C
- be able to supply a heat flux of 40 kW/m² into the test-piece
- have an inner chamber of 200×200×200 mm³
- include two diagnostics ports
- have a wall opening of 125×200 mm² for the testpiece

To meet these requirements the oven presented in figure 2.2 has been build. The inner chamber is surrounded by Zircar ZAL 45, the alumina fiber insulating board. The outer wall of the oven is aluminium. The space between the outer and inner wall is filled with Saffil, an alumina fiber insulating wool. Three silicon carbide heating elements are placed inside the inner chamber. These silicon carbide heating elements type Globar of Carborundum

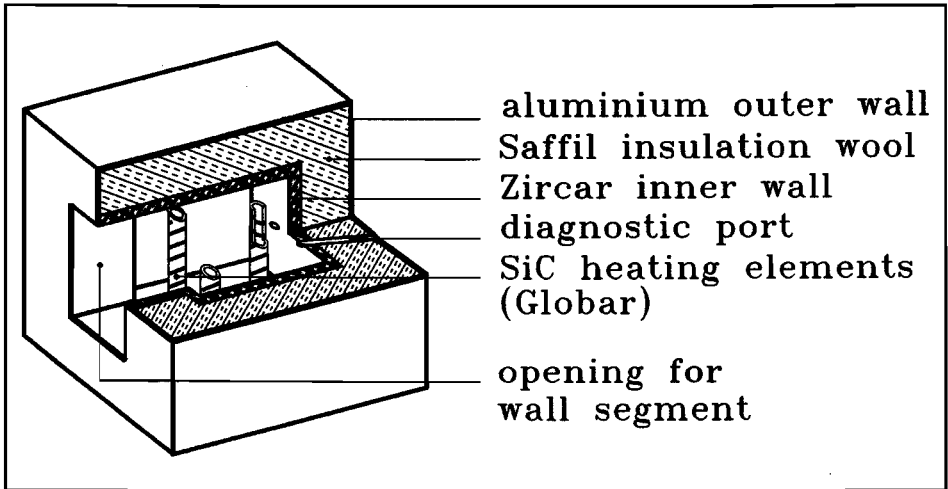


Figure 2.2 Designed oven with two diagnostic ports in the reverse side and with a opening in the front to accept the testpiece.

can transmit the desired power at a temperature of 1600 °C. Because of the fact that the terminals of the elements should be kept at a low temperature, the elements are inserted from the bottom. The temperature in the oven is controlled by a West 2050 programmable controller which activates a thyristor in the power supply. Besides the controller there are two safety systems to prevent overheating of the oven. This control and safety system is given by figure 2.3.

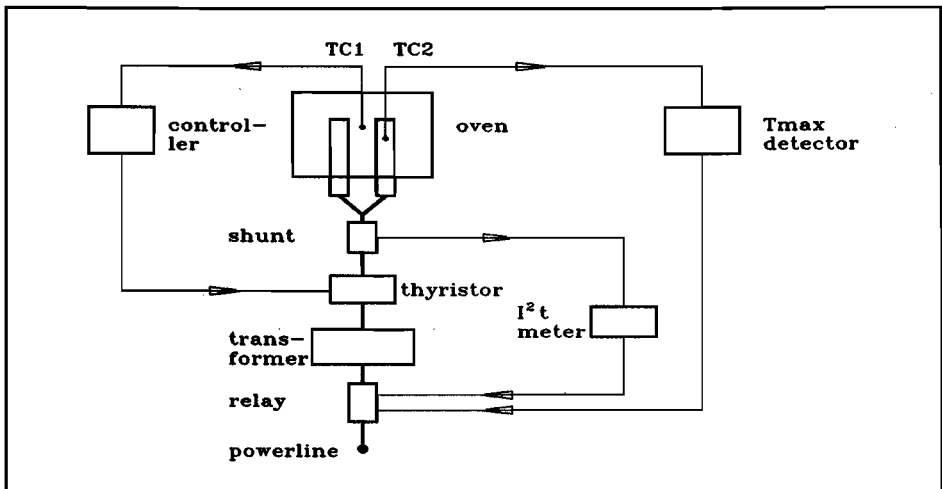


Figure 2.3 Control and safety systems of the oven. Normally the temperature in the oven is controlled by means of TC1 and the controller. A too high temperature in the heating elements results in a shut down of the oven. If the power consumption is too high the oven will also be shut down.

In the oven there are a number of thermocouples measuring the temperature distribution. The measurements from these thermocouples will be used to calculate some thermal properties of the materials used.

2.3 Vibration generator

The testbolts are to be exposed, in the test-rig, to stress fluctuations, which are similar to those in the MHD generator. One way to do this is to incorporate the testpiece in the wall of a pressure vessel and to change the pressure in this vessel. However to change the pressure in such a volume over 50 kPa at a frequency of 1000 Hz would not be easy. Another way to achieve these stress fluctuations is the following. Place a heavy plate under the boltheads. Vibrate the total testpiece. Due to the inertia of the heavy plate the testbolts will be loaded with a fluctuating force. We will use this method in our test-rig.

The size of the inner plate is $125 \times 200 \text{ mm}^2$. With a pressure fluctuation of 50 kPa this will result in a force fluctuation of 1250 N. If we assume the mass of the inner plate to be 2 kg, the acceleration we need is 625 m/s^2 . This is correct if we assume a phase difference of 90 degrees between the movement of the inner plate and the movement of the steel back plate. Both hydraulic and electrodynamic vibration generators can deliver this force (acceleration) at the frequency of 1000 Hz. If we would like to increase the frequency the only available generators are the electrodynamic generators. Because of flexibility it is decided to use an electrodynamic vibration generator. We have chosen type 716 of Ling Dynamic Systems with a frequency range of 5 - 5000 Hz, a maximum acceleration of 700 m/s^2 and a maximum force of 3100 N.

2.4 Interferometer

2.4.1 Michelson-interferometer

In the experiment some properties of the materials used will be verified. To do this the dynamic model of section 3.2, the force measurement, to be described in chapter 2.5 and the acceleration of the steel back plate will be used. Also needed is the acceleration of the inner hot plate. Since this plate is hot ($1500 \text{ }^\circ\text{C}$) a normal acceleration probe can not be used. A laser-interferometer is used, because it has the possibility to measure movements

with a resolution of $0.15 \cdot 10^{-6}$ m. This is sufficient as will be shown later in this section. The laser-interferometer used is the Michelson-interferometer [ref. 2.3 - 2.5]. The basic set-up of this interferometer is given in fig. 2.4.

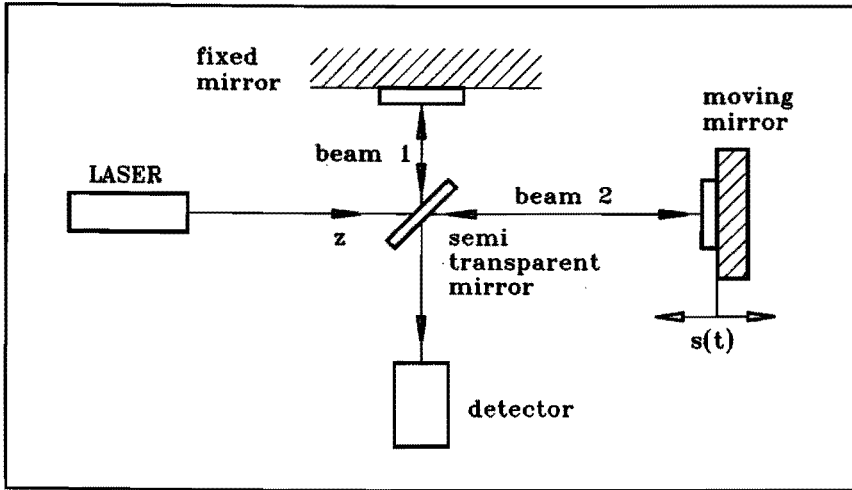


Figure 2.4 Basic set-up of a Michelson interferometer.

The light of the laser is split by means of a semi transparent mirror into two beams. One beam is reflected on a fixed mirror. The other beam is reflected on the moving mirror. Both reflected beams are collected in a detector. A comprehensive description of the Michelson-interferometer is given in appendix B.

2.4.2 Application of the interferometer

The experimental setup of the laser-interferometer is given in figure 2.5. Due to the positions of the heating elements in the oven, the incident laser beam can not be placed perpendicular on the moving mirror. We will compensate the calculated displacement for this oblique measurement. Instead of a fixed mirror we use a couple of beam-splitters to direct one beam into the detector and one beam through the oven. This can cause some problems. The first problem is related to the fact that the wavelength depends on the temperature of the medium, through which the beam passes. Since we measure displacements in wavelengths we have to know the wavelength to express the displacement in m. The second problem is due to the fact that the air inside the oven is moving. So the temperature at a certain place can change in time. We will discuss the influence, of these two problems, on the calculated displacement.

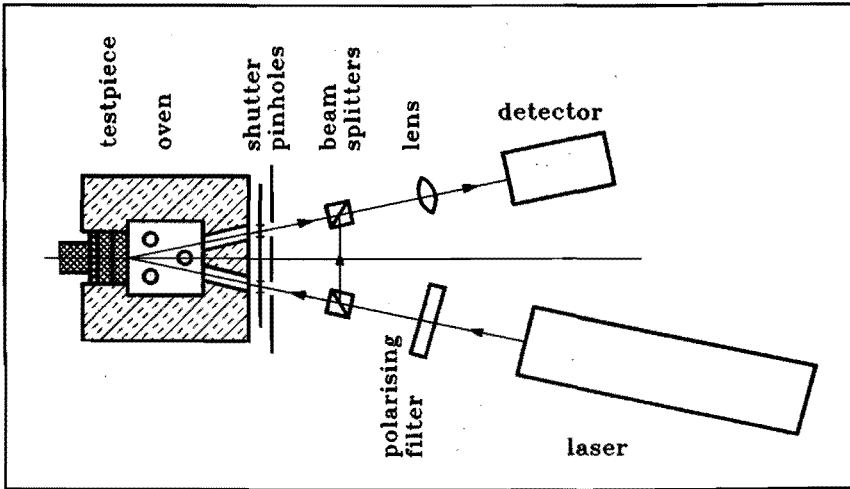


Figure 2.5 Experimental laser-interferometer set-up.

The frequency of the light is independent of the medium. The wavelength of this light depends on the refractive index of the medium. According to Popela [ref. 2.6] this dependency is given by formula 2.1 - 2.3.

$$\lambda_{air} = \frac{\lambda_{vac}}{n} \quad (2.1)$$

$$n = f(T, p, \phi, \lambda_{vac}) \quad (2.2)$$

$$\Delta\lambda = f(T, p, \phi) \quad (2.3)$$

$$= (0.095pT - 0.05T - 60p + 0.05\phi T - 0.215\phi + 23936) 10^{-15}m$$

n - refractive index [-]

T - temperature [°C]

p - pressure [Torr]

ϕ - humidity [%]

At a pressure p of 760 Torr., a temperature of 20 °C and a humidity ϕ of 0 % this gives a temperature dependency of the wavelength according to formula 2.4.

$$\frac{1}{\lambda_{air}} \left(\frac{\partial \lambda}{\partial T} \right) = 9.2810^{-7} / K \quad (2.4)$$

For the HeNe-laser this results in the following wavelengths.

$$\begin{aligned} \lambda_{vac} &= 0.63299138 \cdot 10^{-6} \text{ m} \\ \lambda_{15 \text{ K, } 760 \text{ Torr}} &= 0.6328 \cdot 10^{-6} \text{ m} \\ \lambda_{1773 \text{ K, } 760 \text{ Torr}} &= 0.6337 \cdot 10^{-6} \text{ m.} \end{aligned}$$

The front of the testpiece is at 1773 K. The movement of the testpiece is very small ($20 \cdot 10^{-6}$ m). Within this small region there will be no change in temperature. So we can state that the wavelength near the testpiece equals $0.6337 \cdot 10^{-6}$ m.

The air in the oven will be heated near the heating elements and will flow up there. At some distance (the inner wall of the oven) from the elements the air will flow down. If we model this problem as two concentric cylinders with the element as the central cylinder, we can calculate the air velocity near the outer cylinder [ref. 2.7, 2.8]. The air velocity near the outer cylinder - the moving mirror - will be equal to 0.6 m/s. At a beam diameter of $6 \cdot 10^{-3}$ m the number of fringes on the detector will be 11. If the temperature difference, of the air flowing over the mirror, equals 1.5 K, this will result in two extra fringes on the detector. It will take 0.01 seconds for the hot air to cover the whole beam. During one period of the oscillating movement the error in the calculated displacement will be $1.5 \cdot 10^{-8}$ m. This is acceptable.

2.5 Strain gauge measurement

The forces in the testbolts have to be measured. This will be done by means of strain gauge measurements. We could attach the strain gauges direct on to the silicon nitride bolt. But to calculate the force in the bolt, given a certain strain, you have to know the diameter and the Youngs modulus of the bolt. The diameter can easily be measured. The Youngs modulus of the silicon nitride material is not exactly known. Strain gauges directly bonded to the ceramic can be used if each bolt is calibrated, at the temperature at which it will be used. To perform a good calibration the calibration force should be aligned with the axis of the bolt. It takes a lot of time to calibrate all bolts at the used temperature and with an aligned force. It is easier to use separate measuring shells with strain gauges. These separate shells have to be calibrated only once. The measuring shells can be placed on the cold side of the testpiece so there is no temperature influence on the Youngs

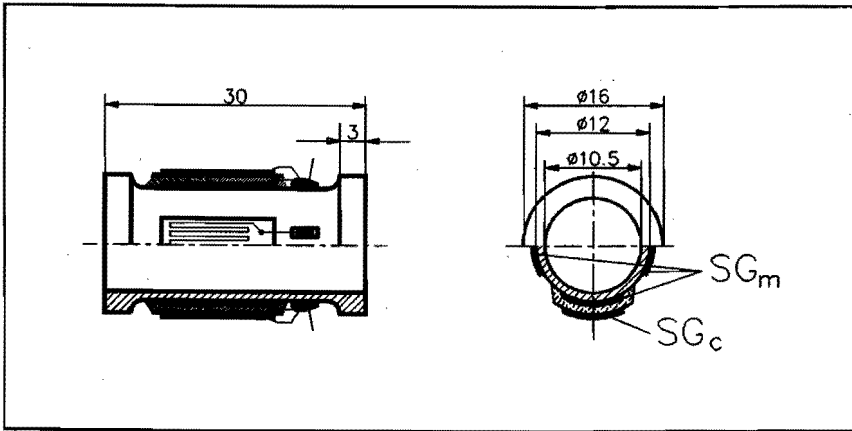


Figure 2.6 Stainless steel measuring shell with four measuring strain gauges (SG_m) and two temperature compensating strain gauges (SG_c).

modulus of the shell material or on the strain gauge. A drawing of a shell is given in figure 2.6.

The shells are made out of stainless steel 316. Four strain gauges (CFLA.6.350.11 of Tokyo Sokki) are directly bonded to the shell. Two strain gauges, of the same type, are bonded to thin stainless steel plates. These curved plates are bonded with heat sink compound to the measuring shell. The latter two are temperature compensating strain gauges. Only two of the four gauges on each shell in combination with the two compensating gauges per shell are used during the measurements. By changing the wiring at the amplifier the gauges to be used can be selected. The amplifiers used are Vishay amplifiers type 2100. These are direct voltage amplifiers.

Known the dimensions of the shell, its Youngs modulus, the gauge factor of the strain gauges and the gain of the amplifier the force - voltage relation can be calculated [ref. 2.9]. This will be done. But the shells will be calibrated as well. The calculations of the force - voltage relation will be given in appendix C.

If two opposite strain gauges on the shell are used, both axial force and transverse bending moment can be calculated. The total axial force is given by formula 2.5 and the bending stress can be deduced from that formula. The definition of the symbols used is given in figure 2.7.

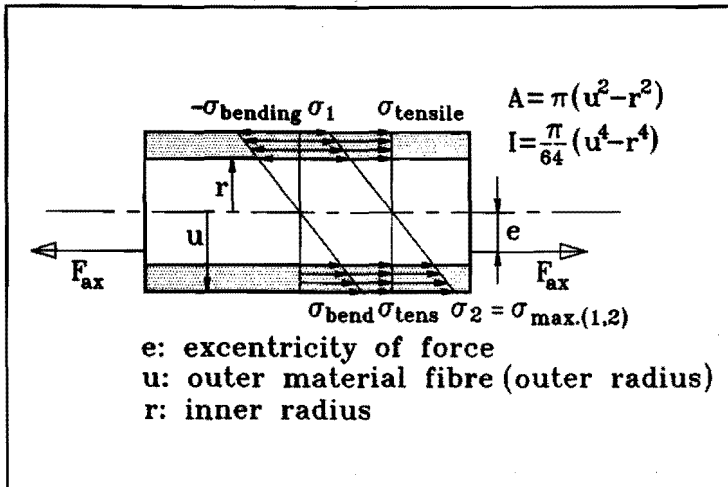


Figure 2.7 Definition of stresses in the measuring shell.

$$F_{ax} = A \frac{\sigma_1 + \sigma_2}{2} \quad (2.5)$$

$$\frac{F_{ax}}{A} = \sigma_{tensile} \quad (2.6)$$

$$\sigma_{bending} = \sigma_{max.(1,2)} - \sigma_{tensile} \quad (2.7)$$

$$\sigma_{bending} = \frac{ueF_{ax}}{I} \Rightarrow e = \frac{\sigma_{bending} I}{uF_{ax}} \quad (2.8)$$

So with two strain gauges the bending moment can be measured.

The strain gauge shells were calibrated in the range from 0 - 500 kgf. This was done by means of another force measuring system. This calibration force measuring system consists of a force transducer, mark Peekel, type TD00500, and an excitation and amplifier system, mark Peekel, type MCA 130 (CA 100, CCA 100). Both the Peekel force transducer and the shell, to be calibrated, in series, were loaded with a force. The output voltage, from two opposite strain gauges, amplified by the Vishay system was plotted as function of the force measured by the Peekel system. Such a plot is given in figure 2.8. From these plots the relations given in table 2.1 were derived.

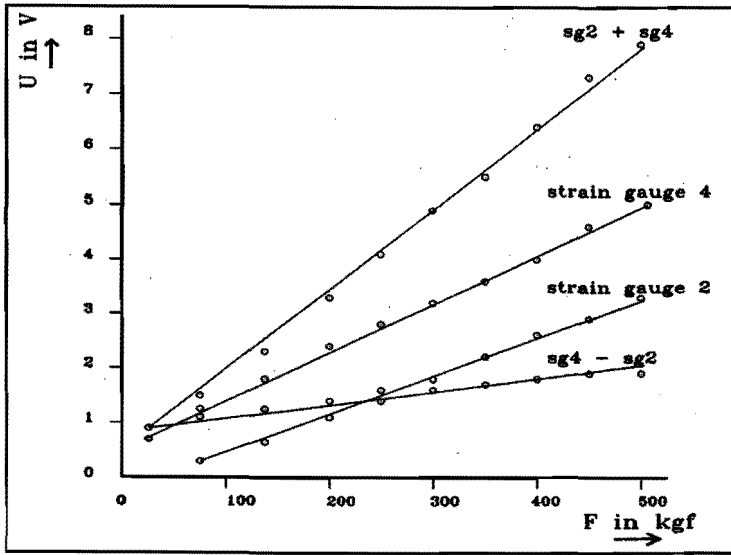


Figure 2.8 Voltage from strain gauges on shell as function of the load measured by force transducer.

Table 2.1 Force-voltage relations for the used strain gauges.

0-500 kgf	strain gauges 1,3	strain gauges 2,4	strain gauges 5,7	strain gauges 6,8	mean strain	variance
$y = f(x)$ $10^{-2}V/kgf$	1.6083	1.5881	1.5155	1.4379	1.5374	0.0670
cor.coef	0.9999	0.9996	0.9997	0.9994		
$x = f(y)$ kgf/V	62.177	62.968	65.985	69.546	65.169	2.89

2.6 Data-acquisition

2.6.1 Introduction to the data-acquisition

From the experiment a large number of data can be extracted. These data will be divided in several groups. The first group of data come from the temperature probes in the oven and in the testpiece. The second group of data are formed by the signals from the strain gauge measurements. A third group of data come

from the laser-interferometer. These three groups of data are frequently sampled by a CAMAC-crate based computer system. A fourth group of data come from the acceleration measurements on the cold side of the testpiece. These data are visualised on an oscilloscope. The fifth group of data come from several flow meters. These data are regularly acquired by hand.

2.6.2 Data-acquisition by the CAMAC-crate

The CAMAC-crate is a system in which several measure-modules can be placed without the need of separate interfaces. The CAMAC-crate is described in IEEE standard 583 [ref. 2.10]. CAMAC is short for Computer Automated Measurement And Control. The standard describes the mechanical and electrical interfaces between the crate and the plug-in modules. The CAMAC-crate is controlled by a controller which can be connected to a computer. The used CAMAC-crate is controlled by a CAPRO-68K computer. This CAPRO is connected to a CADMUS mini-computer.

The temperatures in the oven and in the testpiece are measured by means of thermocouples. The following three kind of thermocouples are used for the described temperature range.

- Chromel - Alumel 0 - 1000 °C
- Pt - PtRh10% 0 - 1700 °C
- PtRh6% - PtRh30% 100 - 1800 °C.

The signals (0 - 30 mV) from these thermocouples are fed into a Programmable Gain Amplifier (PGA), model 5302 of BiRa, which is placed in the crate. Between the experiment and the crate, there is, in a constant temperature box, a change from thermocouple-wire into Cu-wire. In the PGA the signals are amplified (gain depending on the type of thermocouple) before they are fed into a 12 bits A/D convertor. The digital results are stored in the PGA for some time. The controller is programmed to send, every 30 seconds, a signal to the PGA to start a sampling sequence. After this sequence the binary data are transported from the PGA to the CAPRO. The CAPRO stores these results for one hour. Each hour the results are sent to the CADMUS computer for further processing. The data on the CADMUS are, normally every day, translated into time-temperature plots [ref. 2.11, 2.12].

The signals from the strain gauges are also sampled by the PGA in the CAMAC-crate. These signals fluctuate in time with a frequency of 1000 Hz. The signals consist of a DC-part and an AC-part superimposed on the DC-part. By means of a filter (figure 2.9) these two signals are separated into two constant signals. So it is possible to sample those signals with the same system and procedures as the temperature sampling system.

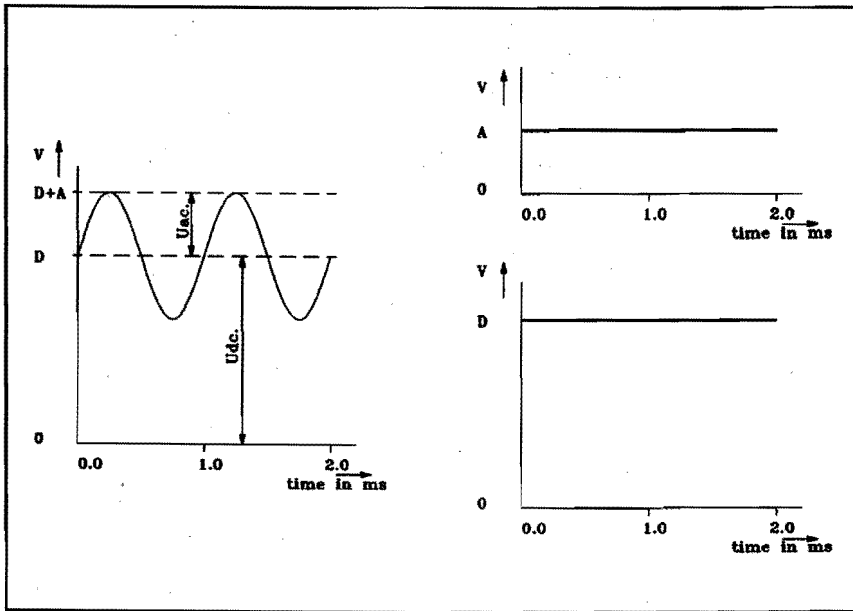


Figure 2.9 Strain gauge signals before and after filtering system.

The acceleration of the inner plate is measured by the CAMAC-system as well. The data-processing of this signal is done in a different way as the processing of the temperature and strain gauge signals. For the acceleration of the inner plate, which is measured by the laser-interferometer described in section 2.4, the fringes that pass over the detector have to be counted. The acceleration has a period time of 1 ms. So counting the fringes for one millisecond would be good enough. As a compromise between poor determination of small acceleration signals (few fringes) and disturbance of the optical path due to convection and turbulence in the oven, the fringes are counted during 5 ms. This will be repeated ten times with an interval of 5 ms. The mean value of these ten measurements is taken as the acceleration. The fringes, passing over the detector, are counted by a quad BCD scaler type 9021 A&B of Nuclear Enterprises LTD. The inhibit signals to start the scaler are generated by a programmable clock generator, model 8501 of Le Croy. Every 30 sec, at the end of the temperature and strain gauge cycle, the acceleration measuring cycle is started. The results of the acceleration measurements are stored on the CAPRO, they are daily processed by the CADMUS.

2.6.3 Data-acquisition by hand

The signal from the acceleration probe on the cold side of the testpiece is regularly acquired by hand. This signal together with the signals of the strain gauges and of the laser-interferometer are used to determine the Youngs moduli of the used materials. The used acceleration probe is a piëzo-electric probe type 4384 of Brüel & Kjær. The output from this probe is amplified by a Brüel & Kjær piëzo-electric amplifier type 5001. There are five flow meters incorporated in the experiment. Three flow meters are placed in air cooling systems. Two of these systems are used to cool the thermocouple connections boards near the oven. The third system is connected to the air flow through the excitator. These three systems are only monitored on a daily base. Flow meter number four is placed in an Argon purge system. The Argon purge is used to minimise the oxidation of the testbolts in the oven. This purge is kept at a constant flow of 0.070 nm³/h. The fifth flow meter is placed in the water cooling system of the testpiece. The measurement of this flow meter, together with the temperature measurement of the inlet- and outlet temperature of the cooling water, is used to calculate the heat flux through the testpiece. Together with temperature measurements in the testpiece the heat conduction coefficients of the insulating layer, at different temperatures will be calculated. The flow of the cooling water is controlled in such a way that the temperature, of the hot side of the epoxy cooling plate, will not exceed 180 °C. Twice a day this flow meter data are acquired.

References chapter 2

- 2.1 Hoek, J. van, "Cesium attack on ceramics", internal notice, Eindhoven University of Technology, 1987.
- 2.2 Drain, L.E., "The laser Doppler technique", John Wiley & Sons, Chichester, 1980,
- 2.3 Ready, J.F., "Industrial application of lasers", Academic Press, New York, 1978.
- 2.4 Sládková, J., "Interference of light", Iliffe Books Ltd., London, 1968.

- 2.5 Schellekens, P.H.J., "Absolute meetnauwkeurigheid van technische laserinterferometers", PhD thesis, Eindhoven University of Technology, 1986.
- 2.6 Popela, B., "The influence of the atmosphere on the wavelength of the HeNe laser and the solutions of the corrections of the laser interferometer.", Optica Acta, vol. 19, no.7, 1972.
- 2.7 -, "V.D.I.- Wärmeatlas", VDI - Verlag GmbH, Düsseldorf, 1977.
- 2.8 Schram, P.P.J.M. e.a., "Fysische transportverschijnselen", dictaat, Technische Hogeschool Eindhoven, 1976.
- 2.9 -, "Kursus rekstrookjes en rekmetingen", Philips Nederland BV, Eindhoven.
- 2.10 -, " CAMAC Instrumentation an Interface Standards ", The Institute of Electrical and Electronic Engineers, New York, 1976.
- 2.11 Toom, E. den, "Ontwikkelen van software voor het opnemen en verwerken van temperaturen op het CAMAC systeem", internal report, EG/88/443, Eindhoven University of Technology, 1988.
- 2.12 Kok, W., "Uitbreiden van software voor het opnemen en verwerken van temperaturen en versnellingen op het CAMAC-systeem", internal report, Eindhoven University of Technology, 1988.

3 MODELLING

3.1 Introduction

To obtain the necessary information for the design of a modular MHD generator wall element, several problems will be solved. These problems are relative to the following items:

- the dynamic behaviour of the generator wall due to the pressure fluctuations
- the temperature distribution in the wall segment in relation with the Youngs modulus of the materials
- the stress distribution in the bolt
- the finite lifetime of the wall segment due to the crack growth in the bolt
- the maximum allowable stress in the bolt given a probability of failure.

These problems will be dealt with separately using some models. The first model will describe the coupling of all the elements that make up the testpiece. It is a simple model that will calculate the dynamic force acting on the testbolt. This first model makes use of the simulation program TUTSIM. Due to the poor dynamic resolution of this program a new program had to be made. This model will be described in section 3.2. In section 3.3 the second model, a kind of finite element method calculation for the heat transfer in the testpiece, is presented. With the third model, a mechanical finite element method, the stress distribution in the testbolt is calculated, given the result of the models mentioned before and the physical dimensions of the bolt. The finite element method will be dealt with in section 3.4. The fourth model will describe the slow crack growth in ceramics. The description of this model is gradually presented, starting at a constant load, over a slowly increasing load to a dynamic changing load. The model is presented in section 3.5. The fifth model, in section 3.6, presents a tool to calculate the allowable stress in our bolt at a given probability of failure, the stress volume integral. Combination of these models results in a method to calculate the lifetime of an MHD generator wall. This will be done in section 3.7.

3.2 Dynamic behaviour

3.2.1 Modelling of the dynamic behaviour

The testbolts will mainly be loaded by a combination of a static and a dynamic force, as is explained in section 1.6. The dynamic force represents the pressure fluctuations in the MHD channel. We assume that these fluctuations are periodical. The frequency of these fluctuations is 1 kHz and the amplitude can be as high as 50 kPa [ref. 3.1]. Given these values and known the dimensions of the testpiece it is possible to calculate the forces, due to the pressure fluctuations, that act on the bolts according to:

$$F = \Delta p \times A \quad (3.1)$$

The static force acting on the bolts is a pre-tension force, needed to prevent a clearance between the several parts of the construction. To make sure that there will never be a clearance in the construction (section 1.6), the pre-tension force will be taken twice as high as the force representing the pressure fluctuations.

In the testrig the same load on the testbolts will be realised. The pressure fluctuations will be simulated by the inertial force of an oscillating mass. The force in the bolts will be measured by a strain gauge measuring unit. Also the acceleration of the inner- and outer plate of the testpiece will be measured. Given these accelerations and forces it is possible, with the aid of a good model, to calculate some material constants of the intermediate layers. There are several methods available to model our testpiece. Firstly a simulation program can be used, that, after setting up of a block diagram, creates the total mathematical model of the system and solves the resulting equations. This can be done by using the simulation program TUTSIM (Twente University of Technology SIMulation). Secondly, by a correct combination of the formulas describing the behaviour of the elements a mathematical model of the total system can be made and the differential equations describing this system can be solved.

3.2.2 TUTSIM modelling

The simulation program TUTSIM is the digital follow up of the analog computer to simulate physical problems. So TUTSIM works

with the same block structure as the old analog computer i.e. integration blocks, summation blocks etc.. For all physical problems (mechanical, electrical, thermal, etc.) the TUTSIM flow scheme is simply:

Problem ---> block model ---> mathematical model---> results.

Before the formulation of the mathematical model the equations have to be known that describe the dynamical behaviour of the elements that make up the system. These simple elements are a mass, a damper and a spring. The constitutive equations which give the relations between force and acceleration, between force and velocity and between force and place for the respective mass, damper and spring are given below [ref. 3.2]

$$\text{MASS: } F - Ma = M \frac{d^2x}{dt^2} \quad (3.2)$$

$$\text{DAMPER: } F - dv = d \frac{dx}{dt} \quad (3.3)$$

$$\text{SPRING: } F - Cx \quad (3.4)$$

F	force	[N]
M	mass	[kg]
a	acceleration	[m/s ²]
x	position	[m]
t	time	[s]
d	damper	[kg/s]
v	velocity	[m/s]
C	stiffness	[N/m]

TUTSIM is a very simple program to handle. It is sufficient to fill in the damping constants etc. in a correctly arranged block diagram.

The modelled testpiece consists of a coupling beam, a cooling plate, a few isolation plates and a heavy inner plate. The whole is bolted together with two testbolts (fig. 3.1). Only movements in the axial direction are considered. Non-axial movements of the whole and in plane bending of the inner plate are neglected. It appears that, in the model, to get a good representation of the construction, the beam should be divided in three different parts. This subdividing is indicated in figure 3.1. The resulting block model for TUTSIM is given by figure 3.2.

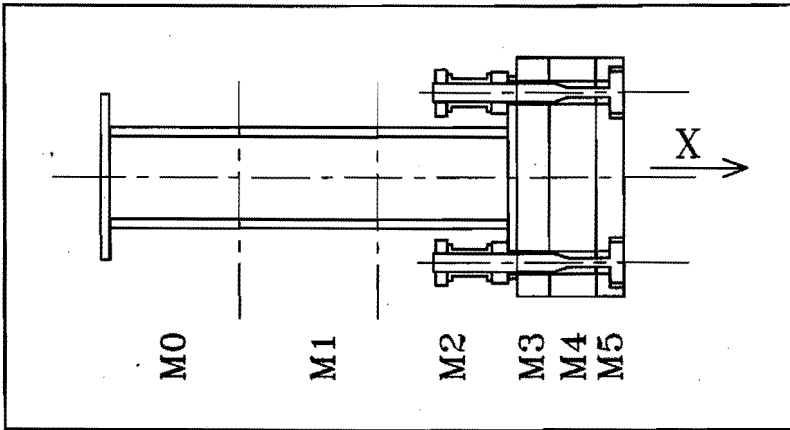


Figure 3.1 Division into several masses of the coupling-beam and the wall segment.

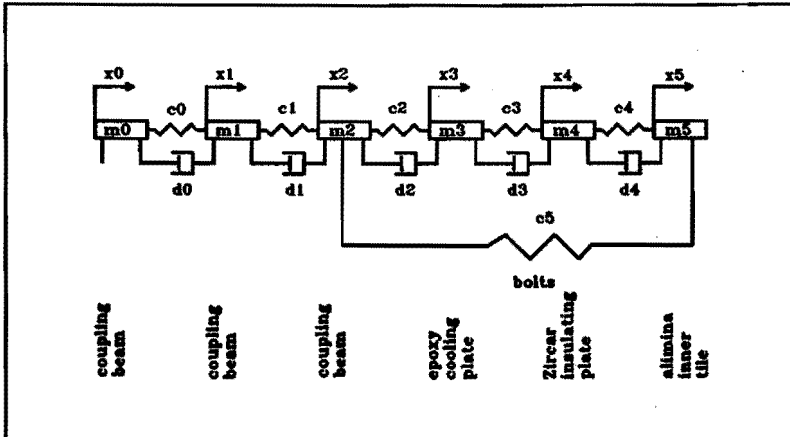


Figure 3.2 TUTSIM block model of coupling beam and wall segment. The mass of the bolt is neglected.

To run this model on a computer, with a normal sine input acceleration, all the initial conditions of the integrators have to be known. This is very difficult to realise. It is more easy to use a soft starter. A soft starter is an input signal which has zero amplitude, zero velocity, zero acceleration and zero impact at time t equals zero. The so called oblique sine is a good example of a soft starter [ref. 3.3]. The formulation of an oblique sine is given by formula 3.5.

$$\text{Oblique sine: } y(t) = \frac{A}{t_{ob}} t - \frac{A}{2\pi} \sin\left(\frac{2\pi t}{t_{ob}}\right) \quad (3.5)$$

A amplitude of cyclic function [N]
 t_{ob} time during which oblique sine is active [s]

Despite the use of this soft starter the simulations did not reach a steady state. The amplitudes increased step after step (fig. 3.3 A). In the real experiments the amplitudes of the accelerations reached a certain steady state level. The number of calculations for the model was extremely large (over $3 \cdot 10^5$). The range of the stiffnesses of the components was also large ($1 \cdot 10^4 - 1 \cdot 10^{11}$). The integration procedure, used by TUTSIM, has no accuracy control. Due to these reasons the simulations jammed.

3.2.3 Coupled differential equations

Since the TUTSIM code failed to produce a steady state solution another method had to be used to solve our dynamical problem. The second method mentioned in section 3.1 will be used. The formulation of the total mathematical model, describing the acceleration of all the masses in the system is given by formulas 3.6 - 3.11. These are a number of coupled differential

$$\ddot{x}_0 = -\frac{C_0}{m_0}x_0 + \frac{C_0}{m_0}x_1 - \frac{R_0}{m_0}\dot{x}_0 + \frac{R_0}{m_0}\dot{x}_1 + \frac{F_{in}}{m_0} \quad (3.6)$$

$$\ddot{x}_1 = \frac{C_0}{m_1}x_0 - \frac{C_0+C_1}{m_1}x_1 + \frac{C_1}{m_1}x_2 + \frac{R_0}{m_1}\dot{x}_0 - \frac{R_0+R_1}{m_1}\dot{x}_1 + \frac{R_1}{m_1}\dot{x}_2 \quad (3.7)$$

$$\ddot{x}_2 = \frac{C_1}{m_2}x_1 - \frac{C_1+C_2+C_5}{m_2}x_2 + \frac{C_2}{m_2}x_3 + \frac{C_5}{m_2}x_5 + \frac{R_1}{m_2}\dot{x}_1 - \frac{R_1+R_2}{m_2}\dot{x}_2 + \frac{R_2}{m_2}\dot{x}_3 \quad (3.8)$$

$$\ddot{x}_3 = \frac{C_2}{m_3}x_2 - \frac{C_2+C_3}{m_3}x_3 + \frac{C_3}{m_3}x_4 + \frac{R_2}{m_3}\dot{x}_2 - \frac{R_2+R_3}{m_3}\dot{x}_3 + \frac{R_3}{m_3}\dot{x}_4 \quad (3.9)$$

$$\ddot{x}_4 = \frac{C_3}{m_4}x_3 - \frac{C_3+C_4}{m_4}x_4 + \frac{C_4}{m_4}x_5 + \frac{R_3}{m_4}\dot{x}_3 - \frac{R_3+R_4}{m_4}\dot{x}_4 + \frac{R_4}{m_4}\dot{x}_5 \quad (3.10)$$

$$\ddot{x}_5 = \frac{C_5}{m_5}x_2 + \frac{C_4}{m_5}x_4 - \frac{C_4}{m_5}x_5 + \frac{R_4}{m_5}\dot{x}_4 - \frac{R_4}{m_5}\dot{x}_5 \quad (3.11)$$

equations which can be represented by the matrix notation of formula 3.12. Because of its high accuracy the one step explicit Runge-Kutta scheme of order five is chosen to solve this set of equations. Once the acceleration of the masses is

$$\left[\frac{d^2x}{dt^2} \right] - \left[A \right] \left[x \right] + \left[B \right] \left[\frac{dx}{dt} \right] + \left[F(t) \right] \quad (3.12)$$

known, as functions of the places and velocities of the masses, the coefficients of the matrixes A and B can be calculated. Now the set of equations can be solved. As a result there can be computed, as a function of time, the accelerations, velocities and positions of the masses and the forces in the springs and dampers. For the model (fig. 3.2) this is done. With the same parameters as used in the TUTSIM method, the Runge-Kutta method did not jam. The result is given in figure 3.3 B. To determine the Youngs module we will process our measured results with the Runge-Kutta method.

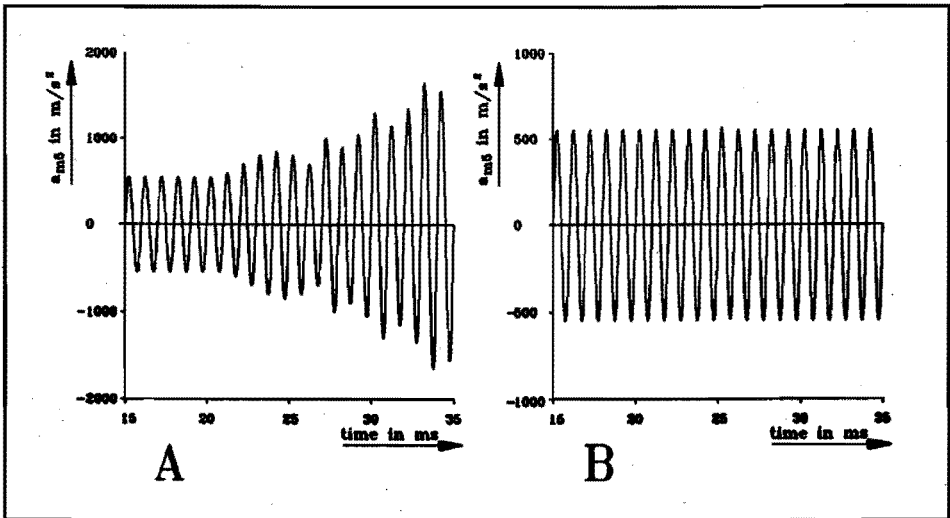


Figure 3.3 Results of the calculated acceleration of the inner tile (m5 fig. 3.2) with the TUTSIM method (A) and with the Runge-Kutta method (B).

3.3 Thermal modelling

In a real MHD generator the inner part of the generator wall is exposed to a high temperature, fast flowing gas. The outer side of the generator is enclosed in a superconducting magnet. To minimise the thermal input into the magnet the outer side of the generator should be kept at low temperature. To realise this condition the generator wall is built up of several layers (fig. 1.5). To simulate a real generator wall the test-

piece will be exposed to the same temperature gradient, which will result in a certain heat flow through the testpiece. For the calculation of the stress distribution in the testbolt the temperature distribution in the testpiece has to be known because the material constants of the bolts are temperature dependent. The material constants given by the manufacturers will also be verified.

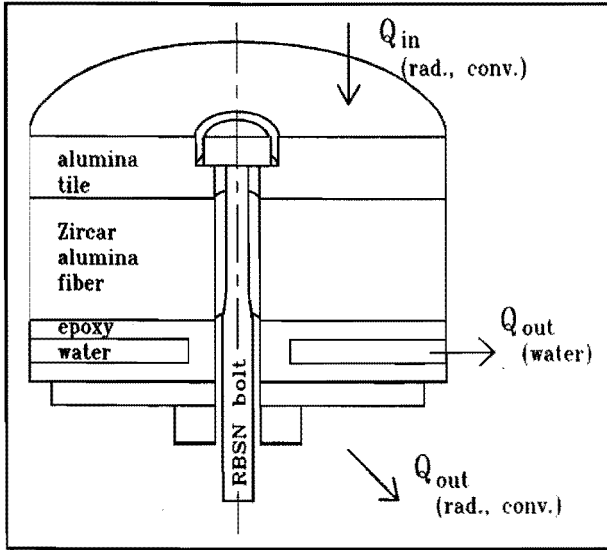


Figure 3.4 Cylinder-symmetrical model of the wall segment with the considered heat fluxes.

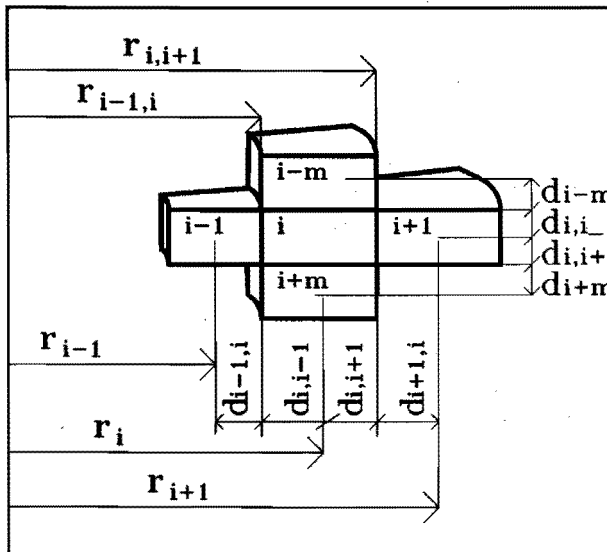


Figure 3.5 Definitions of elements and distances of the thermal model.

Before the calculation of the temperature distribution in the testpiece it first has to be modelled. There are some assump-

$$K'_{i,i} = K_{i,i-m} + K_{i,i-1} + K_{i,i+1} + K_{i,i-m}$$

$$K_{i-1,i} = \frac{\phi h}{\frac{\ln(r_{i-1,i}/r_{i-1})}{\lambda_{i-1}} + \frac{\ln(r_i/r_{i-1,i})}{\lambda_i}} \quad (3.16)$$

$$K_{i+1,i} = \frac{\phi h}{\frac{\ln(r_{i+1,i}/r_i)}{\lambda_i} + \frac{\ln(r_{i+1}/r_{i+1,i})}{\lambda_{i+1}}} \quad (3.17)$$

$$K_{i+m,i} = \frac{1}{\frac{d_{i+m,i}}{\lambda_{i+m}A_{i+m,i}} + \frac{d_{i,i+m}}{\lambda_i A_{i,i+m}}} \quad (3.18)$$

$$K_{i-m,i} = \frac{1}{\frac{d_{i-m,i}}{\lambda_{i-m}A_{i-m,i}} + \frac{d_{i,i-m}}{\lambda_i A_{i,i-m}}} \quad (3.19)$$

- ϕ = tangential width of element [-]
 h = height of element [m]
 r = radius of element [m]
 λ = heat conduction coefficient of element [W/mK]

To calculate the temperature distribution some heat inputs (outputs) and the surrounding temperatures have to be defined. These are the boundary conditions which will be incorporated in the right hand side of the matrix equation. At the hot side of the system there is a constant temperature of the heating rods which results in a radiative and convectional heat input term. The temperature of the inner side of the alumina tile is determined by the program. Free convection along a vertical wall (tile) is assumed to calculate the convectional heat input. For the radiative heat input the emissivity factors used are; $\epsilon_{Al2O3} = 0.92$, $\epsilon_{sic} = 0.86$. At the cold side we have two different boundary conditions. The first cold side is the cooling water channel. At this place there is assumed a constant water temperature. The second cold side is the steel plate of the testpiece. Due to the constant temperature outside the oven there is a radiative and a convectional negative heat input at the steel plate. There are two other boundaries of our cylindrical system. At the axis of the cylinder there is no heat transfer in radial direction. Also at the outer radius of the cylinder there will be no radial heat transfer. The equation to be solved is equation 3.20. This equation is

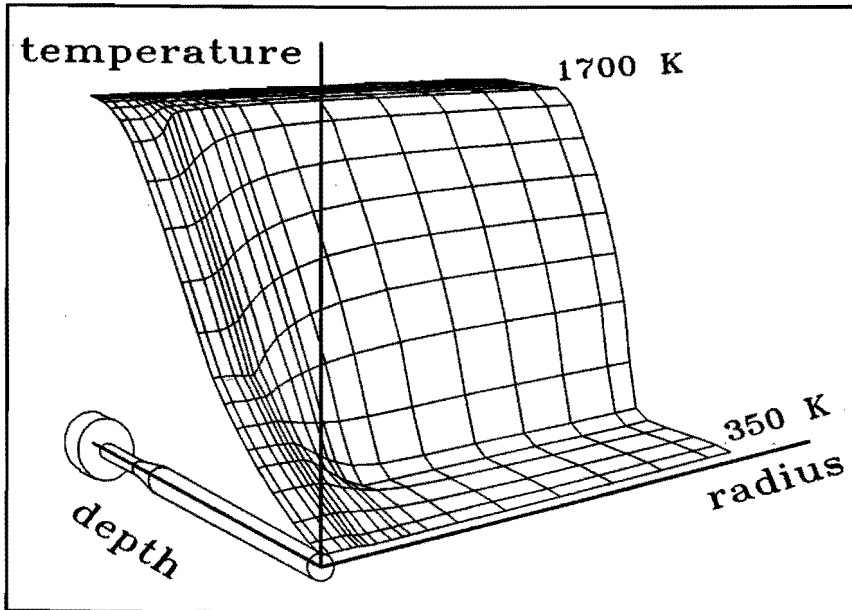


Figure 3.7 Temperature distribution in testpiece. Left-side is bolt-axis.

3.4 Crack growth modelling

3.4.1 Subcritical crack growth

Ceramics can withstand large compressive stresses. If a tensile stress is put on the ceramic the situation is quite different. The cracks in the ceramics - from the fabrication process or caused by the machining process - start to grow, even at low stresses. This is called the subcritical crack growth [ref. 3.6 - 3.16]. The first stage of it is sometimes called corrosion induced crack growth [ref. 3.17]. We will call the total phenomena subcritical crack growth, but we have to keep in mind that it is influenced by the environment. The cracks will grow in size, often at a very low speed, until catastrophic failure of the ceramic part occurs. In the next sections this crack growth phenomena will be described.

3.4.2 Crack velocity versus stress intensity

The relation between the crack velocity and the applied stress intensity factor has been determined by a number of authors for several materials [ref. 3.19 - 3.20]. An idealised diagram of this relation, in which there are a number of stages, is shown in figure 3.8.

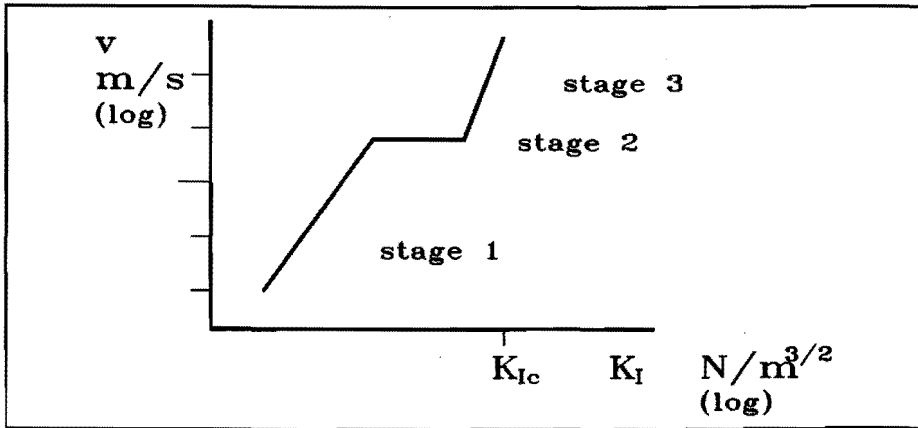


Figure 3.8 Crack velocity versus stress intensity factor.

In stage 1 the $\log v$ is proportional to $\log K_I$. In this region there is a strong interaction between the environment and the ceramic. In stage 2 the rate of diffusion of corrosive species to the crack tip is rate controlling and the v is independent of K_I . In stage 3 the $\log v$ is again proportional to $\log K_I$. Several mechanism, e.g. plastic deformation induced crack growth, thermal induced dislocation movement or grain boundary sliding control this stage. This stage is assumed to occur in all ceramics. At the end of stage 3 the stress intensity factor has reached its critical value (material dependent) and the crack will grow instantaneously with a catastrophic result. After definition of the stress intensity by formula 3.21 a general expression of the crack growth relation will be given by formula 3.22.

$$K = Y\sigma\sqrt{a} \quad (3.21)$$

- | | |
|---------------------------------|-----------------------|
| K_I = stress intensity factor | [N/m ^{3/2}] |
| Y = shapefactor of crack | [-] |
| σ = global stress | [Pa] |
| a = crack length | [m] |

$$v = \frac{da}{dt} = A \cdot e^{\left(\frac{-Q}{RT}\right)} (Y\sigma\sqrt{a})^n \quad (3.22)$$

v	= crack growth velocity	[m/s]
A^*	= constant	[-]
Q	= activation energy	[J/mol]
R	= gas constant	[J/molK]
T	= temperature	[K]

The relation for the crack growth velocity is temperature dependent. The test will be performed at one temperature. Relation 3.22 will be simplified to relation 3.23 to exclude the temperature dependency. This relation will be used throughout this thesis.

$$\text{crack velocity : } v = \frac{da}{dt} = AK_1^n \quad (3.23)$$

Reaction bonded silicon nitride is a porous material (20 %). Although a mean pore size of 20 μm is given for our material, the measured largest pore had a length of 835 μm . The pores are surrounded by a number of grains. There is no secondary SO_2 phase inside the pores nor between adjacent grains. At high temperatures, in contrary to the HPSN, the RBSN grains can not

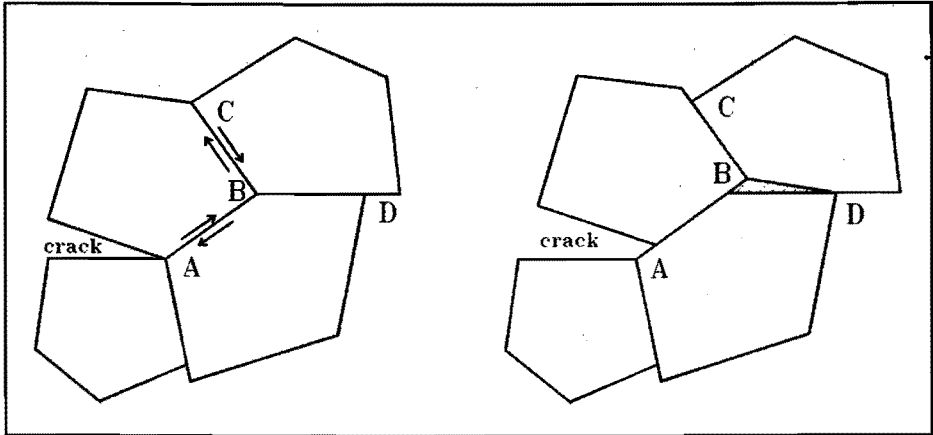


Figure 3.9 Schematic representation of crack growth by a combination of grain boundary sliding and dislocation movement. Due to the grain boundary sliding along lines AB and BC the crack will grow. Without self diffusion a secondary crack will be initialised at BD. Self diffusion, either through the bulk (Nabarro-Herring) or by the grain boundaries (Coble), will deform the grains to fill this secondary crack.

slide over a soft secondary phase. The crack growth can be stimulated by thermal activated dislocation movement. The dislocations can be formed at the grain boundaries [ref. 3.21]. Another possible crack growth mechanism, which is said to occur more often in RBSN [ref. 3.22], is the crack growth

by means of grain boundary sliding. Figure 3.9 gives an impression of several stages of this crack growth mechanism.

3.4.3 Subcritical crack growth under static load

Many constructions are subjected to a static load. Description of the crack growth (lifetime) in such a construction is of technical importance. Assume the ceramic part will be used under a certain tensile stress distribution. The part will first be proof tested shortly under a higher but equally distributed stress σ_p . If the part does not break during the proof test then nowhere in the part the stress intensity factor has reached its critical level.

$$K_{Ip} = Y\sigma_p\sqrt{a_p} \leq K_{Ic} \quad (3.24)$$

Y = shape factor [-]

σ_p = proof stress [Pa]

a_p = crack length during proof test [m]

After this proof stressing, the cracks, at the point of highest tensile stress, have a maximum length a_p . During normal use the stress σ_u on the part will be lower than the stress during the proof stressing σ_p . The start value of K_I will also be lower.

$$K_I(t=0) = Y\sigma_u\sqrt{a_p} \quad (3.25)$$

$$\sigma_u \leq \sigma_p \quad (3.26)$$

$$3.24, 3.25, 3.26 \Rightarrow K_I(t=0) \leq \frac{\sigma_u}{\sigma_p} K_{Ic} \quad (3.27)$$

During a constant load the stress intensity factor only increases due to the growth of the crack.

$$\frac{dK_I(t)}{dt} = \frac{Y\sigma_u}{2\sqrt{a(t)}} \frac{da(t)}{dt} \quad (3.28)$$

$$3.23, 3.28 \Rightarrow \frac{dK_I(t)}{dt} = \frac{AY\sigma_u}{2\sqrt{a(t)}} K_I^n(t) \quad (3.29)$$

$$K_I(t) = Y\sigma_u\sqrt{a(t)} \quad (3.30)$$

$$3.29, 3.30 \rightarrow \frac{dK_I(t)}{dt} = \frac{AY^2\sigma_u^2}{2} K_I^{n-1}(t) \quad (3.31)$$

$$\int_{K_I(0)}^{K_{Ic}} \frac{dK_I(t)}{K_I^{n-1}(t)} = \int_{t=0}^{t_f} \frac{AY^2\sigma_u^2}{2} dt \quad (3.32)$$

$$\frac{1}{(n-2)} \left(-\frac{1}{K_{Ic}^{n-2}} + \frac{1}{K_I^{n-2}(t=0)} \right) = \frac{AY^2\sigma_u^2}{2} t_f \quad (3.33)$$

$$t_f = \frac{2}{AY^2\sigma_u^2(n-2)K_{Ic}^{n-2}} \left(\left(\frac{K_{Ic}}{K_I(0)} \right)^{n-2} - 1 \right) \quad (3.34)$$

Since the part did not break during the test the size of the largest crack will be smaller than a_p .

$$t_f \geq \frac{2}{AY^2\sigma_u^2(n-2)K_{Ic}^{n-2}} \left(\left(\frac{\sigma_p}{\sigma_u} \right)^{n-2} - 1 \right) \quad (3.35)$$

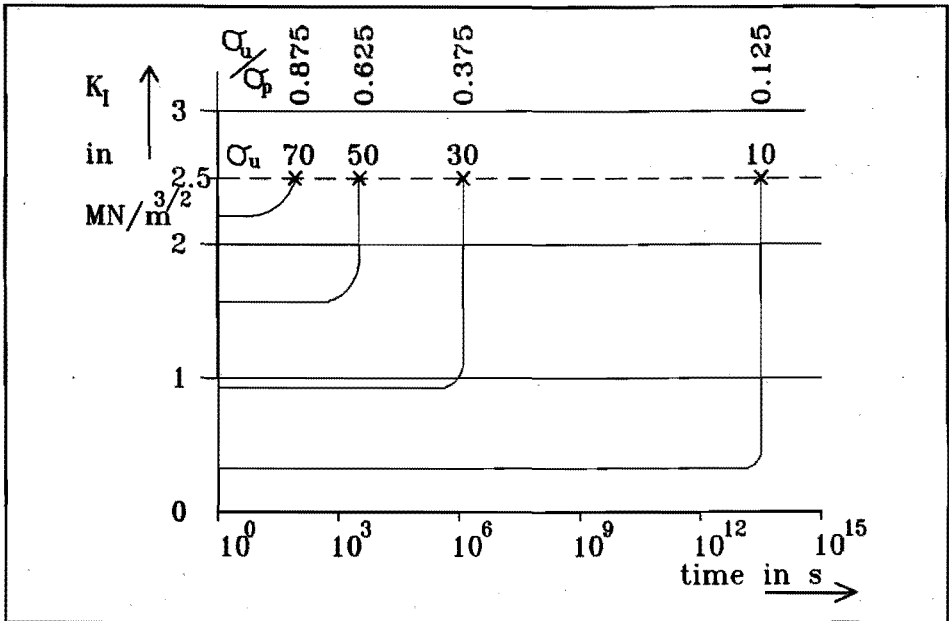


Figure 3.10 Increase of the stress intensity factor during the lifetime of a component, according to formula 3.29, with σ_u as parameter. As soon as the curve reaches the critical stress intensity factor of $2.5 \text{ MN/m}^{3/2}$ (RBSN) the component will fail. Due to the greater than sign in formula 3.35 this failure can be postponed. The assumed σ_p is equal to 80 MPa . The constants $A = 1 \cdot 10^{-99}$, $n = 18$ are according to our measurements.

If the proof stress is relatively high then a large number of specimens will fail during proof stressing. If the proof stress equals the stress during normal use then the lifetime of some of the parts will be short. There has to be found an optimum between tensile stress of the material, the proof stress and the stress during normal use to achieve a certain lifetime with a few failures during proof stressing. To make sure that the lifetime can be calculated all the parts have to be exposed to the proof stress. As will be shown in section 3.6 there is also another way to calculate the lifetime without testing all the parts.

For certain values of σ_u/σ_p the increase of K_I in time is given by figure 3.10. A small change in the value of σ_u/σ_p has a great influence on the lifetime as can be seen in this figure.

3.4.4 Subcritical crack growth under increasing load

Although not of technical importance, the subcritical crack growth under a slowly increasing load will be described in this paragraph. As will be shown the model is important to acquire material data that describe the subcritical crack growth.

As with the constant load, all parts will be shortly proof tested with a constant load, before applying the increasing load. After the test the largest crack in the part has a length a_p . During use the stress will be time dependent according to formula 3.36.

$$\sigma_u(t) = Bt \quad (3.36)$$

$$B = \text{constant} \quad [\text{Pa/s}]$$

For small values of B the stress intensity factor at time $t = 1$ s will be.

$$K_I(1) = Y\sigma_u(1)\sqrt{a(1)} = YB1\sqrt{a(1)} \leq \frac{\sigma_u(1)}{\sigma_p} K_{Ic} \quad (3.37)$$

During the lifetime, the stress intensity factor will increase due to the increase of the crack size and due to the growth of the stress.

$$\frac{dK_I(t)}{dt} = YB\sqrt{a(t)} + \frac{YBt}{2\sqrt{a(t)}} \frac{da(t)}{dt} \quad (3.38)$$

$$3.37, 3.38 \rightarrow \frac{dK_I(t)}{dt} = \frac{YBK_I(t)}{Ybt} + \frac{Y^2B^2t^2}{2K_I(t)} \frac{da(t)}{dt} \quad (3.39)$$

$$3.23, 3.39 \rightarrow \frac{dK_I(t)}{dt} = \frac{K_I(t)}{t} + \frac{AY^2B^2t^2}{2} K_I^{n-1} \quad (3.40)$$

There is no simple analytical solution for this differential equation. This first order initial value problem will be solved with a Runge-Kutta method. Figure 3.11 gives us the increase of the stress intensity factor for a certain value of B, compared with two curves of constant stress.

3.4.4.1 Determination of the crack growth parameters

The crack growth parameters n, A can be determined by measuring the time to failure and the failure stress of two parts loaded with different stress increment velocities. The crack growth parameters are used in the power law for the crack growth velocity $v = da/dt = A \cdot K_I^n$. Given the relation for a slowly increasing stress superimposed on a constant stress σ_{pl} .

$$\sigma(t) = \sigma_{pl} + \dot{\sigma}t \quad (3.41)$$

$$\frac{d\sigma(t)}{da(t)} = \frac{d\sigma(t)}{dt} \frac{dt}{da(t)} \quad (3.42)$$

$$3.23, 3.41, 3.42 \rightarrow \frac{d\sigma(t)}{da(t)} = \frac{\dot{\sigma}}{AK_I^n(t)} \quad (3.43)$$

$$3.21, 3.43 \rightarrow \frac{d\sigma(t)}{da(t)} = \frac{\dot{\sigma}}{AY^n \sigma^n(t) \sqrt{a^n(t)}} \quad (3.44)$$

$$\sigma^n(t) d\sigma(t) = \frac{\dot{\sigma} da(t)}{AY^n \sqrt{a^n(t)}} \quad (3.45)$$

$$\int_{\sigma(0)}^{\sigma_f} \sigma^n(t) d\sigma(t) = \int_{a(0)}^{a_f} \frac{\dot{\sigma} da(t)}{AY^n \sqrt{a^n(t)}} \quad (3.46)$$

$$\frac{\sigma_f^{n+1} - \sigma_{pl}^{n+1}}{n+1} = -\frac{\dot{\sigma}}{AY^n} \frac{2}{(n-2)} \left(\frac{1}{(\sqrt{a_f})^{n-2}} - \frac{1}{(\sqrt{a(0)})^{n-2}} \right) \quad (3.47)$$

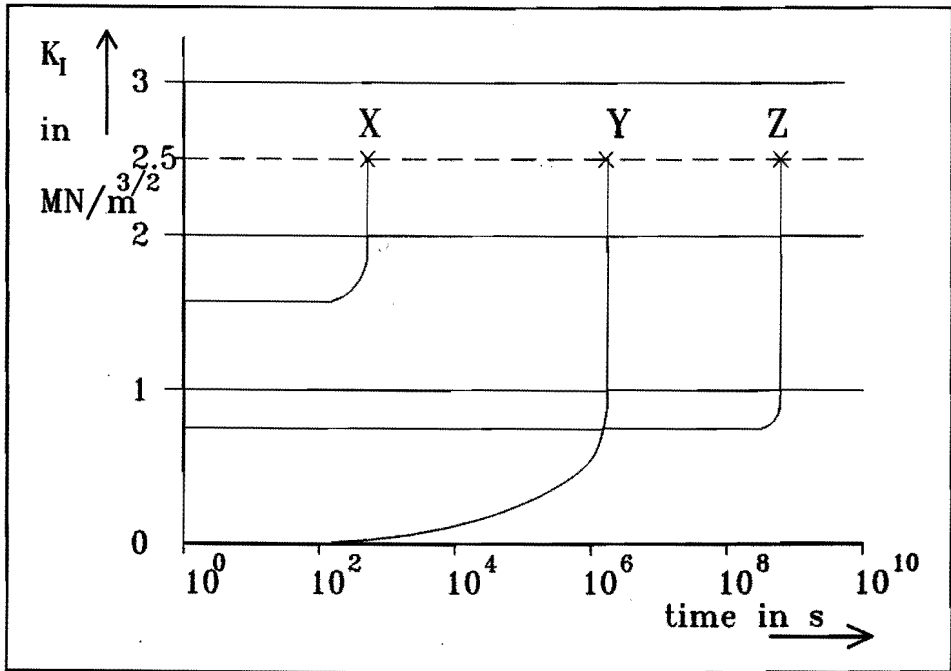


Figure 3.11 Increase of the stress intensity factor during the lifetime of a component, according to formula 3.40. Due to the greater than sign in formula 3.35 the lifetime can be longer than the time the curve reaches the critical stress intensity factor $K_{Ic} = 2.5 \text{ MN/m}^{3/2}$. The assumed $\sigma_p = 80 \text{ MPa}$. The constants $A = 1 \cdot 10^{99}$, $n = 18$ are according to our measurements. Curve X represents a constant stress of 50 MPa. Curve Y represents a slowly increasing stress with $B = 50 \text{ Pa/s}$. Curve Z represents a constant stress of 25 MPa. The lifetime of the slowly increasing stress is longer than that of the constant stress of 50 MPa.

$$\frac{\sigma_f^{n+1} - \sigma_{pl}^{n+1}}{n+1} = \frac{-2\dot{\sigma}}{AY^2(n-2)} \left(\frac{1}{Y^{n-2}(\sqrt{a_f})^{n-2}} - \frac{1}{Y^{n-2}(\sqrt{a(0)})^{n-2}} \right) \quad (3.48)$$

$$3.21, 3.24, 3.48 \Rightarrow \frac{\sigma_f^{n+1} - \sigma_{pl}^{n+1}}{n+1} = \frac{-2\dot{\sigma}}{AY^2(n-2)} \left(\frac{\sigma_f^{n-2}}{K_{Ic}^{n-2}} - \frac{\sigma(0)^{n-2}}{K_I(0)^{n-2}} \right) \quad (3.49)$$

$$\frac{\sigma_f^{n+1} - \sigma_{pl}^{n+1}}{n+1} = -\frac{2\dot{\sigma}}{AY^2(n-2)} \left(\frac{\sigma_f^{n-2}}{K_{Ic}^{n-2}} - \frac{1}{Y^{n-2}(\sqrt{a(0)})^{n-2}} \right) \quad (3.50)$$

$$\text{with } Q = \frac{AY^2(n-2)}{2(n+1)} \quad \text{and} \quad S = -\frac{1}{Y^{n-2}(\sqrt{a(0)})^{n-2}}$$

$$\dot{\sigma} = - \frac{(\sigma_{pl}^{n+1} - \sigma_f^{n+1}) Q}{\left(\frac{\sigma_f^{n-2}}{K_{Ic}^{n-2}} + S \right)} \quad (3.51)$$

With two different stress increase velocities $\dot{\sigma}_1$ and $\dot{\sigma}_2$ this results in formula 3.52.

$$\frac{\dot{\sigma}_1}{\dot{\sigma}_2} = \frac{\left(\frac{(\sigma_{pl1}^{n+1} - \sigma_{f1}^{n+1}) Q}{\frac{\sigma_{f1}^{n-2}}{K_{Ic}^{n-2}} + S} \right)}{\left(\frac{(\sigma_{pl2}^{n+1} - \sigma_{f2}^{n+1}) Q}{\frac{\sigma_{f2}^{n-2}}{K_{Ic}^{n-2}} + S} \right)} \quad (3.52)$$

For both parts (both velocities) the factors K_{Ic} , Q and S are the same. With an iterative procedure it is possible to solve equation 3.52 to get the crack growth exponent n . Known the factor K_{Ic} and the lifetime t_f , the crack growth factor A can be fitted to get a solution of the differential equation 3.40, which described the crack growth under slowly increasing load.

The parameters, describing the crack growth velocity, according to $v = AK_I^n$, are now determined by this method.

3.4.5 Subcritical crack growth under cyclic load

Many constructions are subjected to cyclic loads σ_{al} superimposed on a static load σ_{pl} . The growth of a crack in a ceramic part under such a load will be described in the first part of this section. In the second part an effective stress will be introduced which simplifies the calculation of the lifetime of a ceramic under cyclic load.

As with the other loads, all parts will be proof tested, before applying the normal load. After the test the largest crack in the part has a length smaller than a_p . During the use, the stress can be time dependent e.g. according to formula 3.53.

$$\sigma_u(t) = \sigma_{pl} + \sigma_{al} \sin(\omega t) \quad (3.53)$$

σ_{pl} = pre-load stress [Pa]

σ_{al} = alternating stress [Pa]

Immediately after applying the load the maximum stress intensity factor will be:

$$K_I(t) = Y\sigma_u(t)\sqrt{a_p} \quad (3.54)$$

$$3.53, 3.54 \rightarrow K_I(t) = Y\sigma_{pl}\sqrt{a_p} + (Y\sigma_{al}\sqrt{a_p})\sin(\omega t) \quad (3.55)$$

During the lifetime, the stress intensity factor will vary due to the increase in crack size and due to the cyclic fluctuation in the stress.

We have no detailed knowledge about processes of plasticity near the crack tip in RBSN. Grain boundary sliding can be one of the processes [ref. 3.22]. We suppose that static crack growth, e.g. by grain boundary sliding, will be the most important mechanism.

$$\begin{aligned} \frac{dK_I(t)}{dt} &= \frac{Y\sigma_{pl}}{2\sqrt{a(t)}} \frac{da(t)}{dt} + \omega Y\sigma_{al}\sqrt{a(t)} \cos(\omega t) \\ &+ \frac{Y\sigma_{al}}{2\sqrt{a(t)}} \sin(\omega t) \frac{da(t)}{dt} \end{aligned} \quad (3.56)$$

$$\begin{aligned} 3.30, 3.56 \rightarrow \frac{dK_I(t)}{dt} &= \frac{Y^2\sigma_{pl}\sigma_u(t)}{2K_I(t)} \frac{da(t)}{dt} + \frac{\omega Y\sigma_{al}K_I(t)}{Y\sigma_u(t)} \cos(\omega t) \\ &+ \frac{Y^2\sigma_{al}\sigma_u(t)}{2K_I(t)} \sin(\omega t) \frac{da(t)}{dt} \end{aligned} \quad (3.57)$$

$$\begin{aligned} 3.23, 3.57 \rightarrow \frac{dK_I(t)}{dt} &= \frac{AY^2\sigma_{pl}\sigma_u(t)}{2} K_I(t)^{n-1} + \frac{\omega\sigma_{al}K_I(t)}{\sigma_u(t)} \cos(\omega t) \\ &+ \frac{AY^2\sigma_{al}\sigma_u(t)}{2} K_I(t)^{n-1} \sin(\omega t) \end{aligned} \quad (3.58)$$

$$\begin{aligned} 3.53, 3.58 \rightarrow \frac{dK_I(t)}{dt} &= K_I(t) \left(\frac{\omega\sigma_{al}\cos(\omega t)}{\sigma_{pl} + \sigma_{al}\sin(\omega t)} \right) \\ &+ \frac{AY^2K_I(t)^{n-1}}{2} (\sigma_{pl}^2 + 2\sigma_{pl}\sigma_{al}\sin(\omega t) + \sigma_{al}^2\sin^2(\omega t)) \end{aligned} \quad (3.59)$$

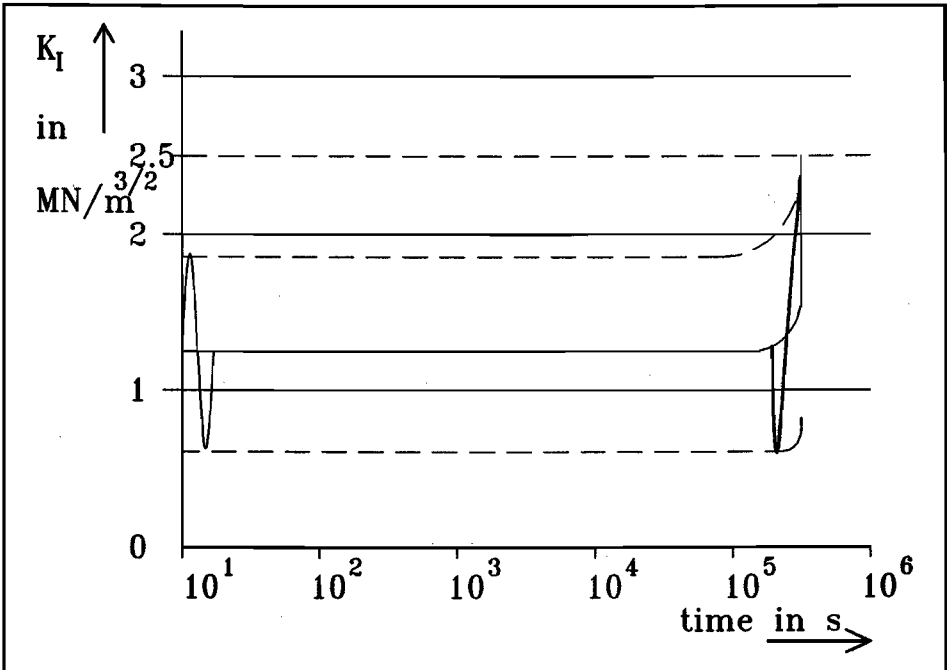


Figure 3.12 Calculated envelope of the stress intensity factor during the lifetime of a component, under cyclic load, according to formula 3.59. Due to the greater than sign in formula 3.35 the lifetime can be longer than the time before the curve reaches the critical stress intensity factor of RBSN $K_{Ic} = 2.5 \text{ MN/m}^{3/2}$. The assumed σ_p is 80 MPa, σ_{pi} is 40 MPa and σ_{ai} is 20 MPa. The constants $A = 1 \cdot 10^{-99}$, $n = 18$ are according to our measurements.

Equation 3.59 has first been solved with the Runge-Kutta method. Afterwards an analytical solution was found for this differential equation of Bernoulli (as is done in appendix D). Using the analytical solution of equation 3.53, to calculate the lifetime, is less time consuming than using the Runge-Kutta method. Figure 3.12 gives the envelope of the stress intensity factor for RBSN.

3.4.5.1 Effective stress

To calculate the lifetime of a ceramic part under a cyclic load, with the Runge-Kutta method to solve equation 3.59, is very time consuming. It is more adequate to introduce an effective stress and to use equation 3.35 to calculate the lifetime of a ceramic part. To simulate a cyclic load a constant effective stress can be introduced, if the number of cycles is

large during the lifetime of the part. If the periodic time is very small compared to the lifetime, the increase in crack size, during one cycle, can be neglected. During one period the stress intensity factor will then be dependent on the stress only.

$$K_I(t) = Y\sigma(t)\sqrt{a} = C\sigma(t) \quad (3.60)$$

C : constant [m^{1/2}]
 \bar{a} : mean value of crack size during one period [m]

The crack growth velocity will be given by formula 3.61.

$$v = \frac{da(t)}{dt} = AK_I^n(t) = AC^n\sigma_u^n(t) \quad (3.61)$$

We will define the effective stress as that constant stress, which has, during one period, the same effect on the crack growth, as the cyclic stress [ref. 3.23].

$$\bar{v} = \frac{1}{T} \int_0^T AC^n \sigma_u^n(t) dt = AC^n \sigma_{eff}^n \quad (3.62)$$

$$\sigma_{eff} = \left[\frac{1}{T} \int_0^T \sigma_u^n(t) dt \right]^{\frac{1}{n}} \quad (3.63)$$

$$\sigma_{eff} = \left[\frac{1}{T} \int_0^T (\sigma_{pl} + \sigma_{al} \sin(\omega t))^n dt \right]^{\frac{1}{n}} \quad (3.64)$$

For other periodic loads, with $\sigma > 0$ during the period, an effective stress can be defined in the same way. For certain values of σ_{al}/σ_{pl} , the effect of the crack growth exponent n on the effective stress is shown in figure 3.13. During one period, the instantaneous stress intensity factor will reach a higher level than the effective stress intensity factor. This is shown in figure 3.14. An effective critical stress intensity factor is defined, as indicated in figure 3.14, in such a way that the effective stress can be used to calculate a correct lifetime, given the value of K_{Ic} .

$$K_{Ic}^* = \frac{\sigma_{eff}}{\sigma_{pl} + \sigma_{al}} K_{Ic} = \frac{\sigma_{eff}}{\sigma_{max}} K_{Ic} \quad (3.65)$$

K_{Ic}^* : effective critical stress intensity factor [N/m^{3/2}]

When using an effective stress to calculate the lifetime also the (lower) effective stress intensity factor should be used

as upper border of the integration interval. When subjecting a part to a cyclic load according formula 3.53, then the lifetime of that part will decrease, compared with the lifetime of a part, subjected to the preload stress only.

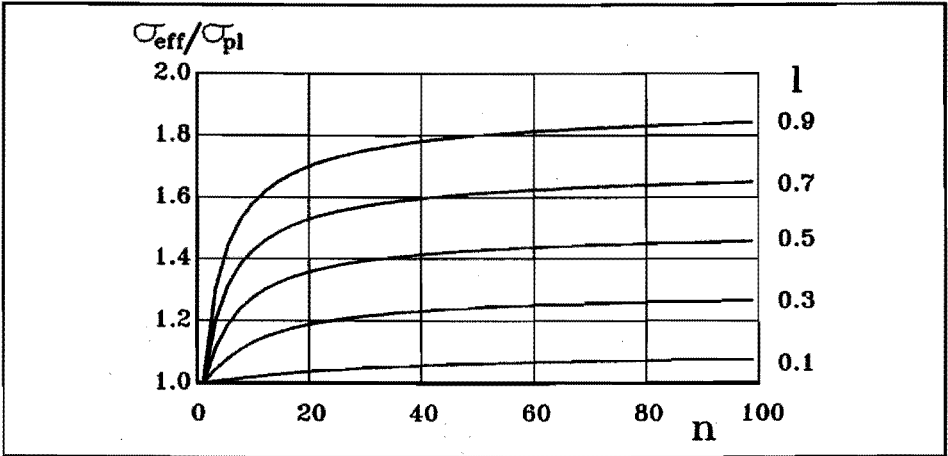


Figure 3.13 The effective stress over the preload stress as function of the the crack growth exponent n . The parameter $l = \sigma_a/\sigma_{pr}$

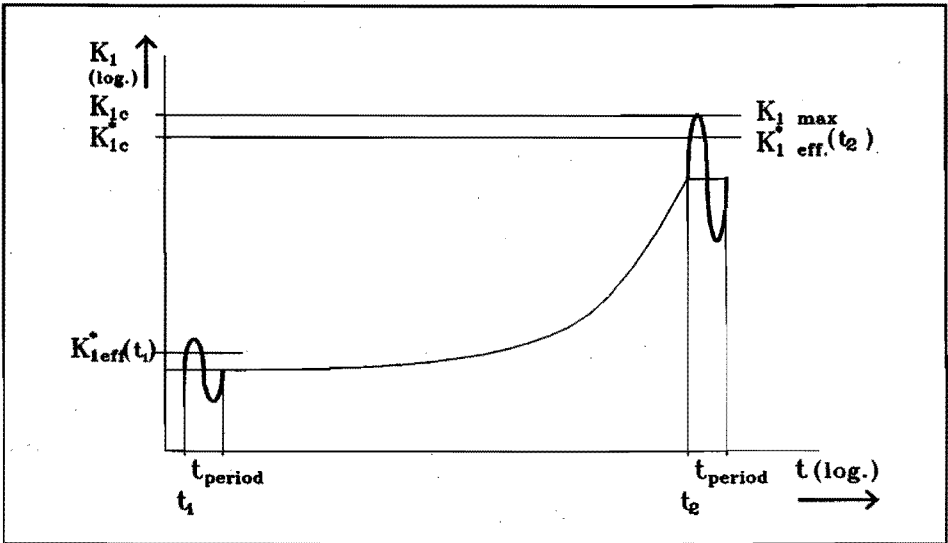


Figure 3.14 The development of the stress intensity factor. Indicated are the effective stress intensity factor $K_{I,eff}$ and the maximum stress intensity factor $K_{I,max}$

3.5 Finite element method

In the last section was shown, how the lifetime of a ceramic part, subjected to a certain stress distribution can be calculated. All the parts had to be tested first, with the same stress distribution as during normal use. There is another approach possible without testing all the parts. When using this probabilistic approach data delivered by the ceramic supplier are used to calculate the maximum allowable stress in the part accepting a certain probability of failure.

For simple geometries and loadings it is easy to calculate the maximum stress using handbooks like [ref. 3.23 - 3.27]. To determine the maximum stress in a more complex geometry or load case, finite element methods are used [ref. 3.28]. The program we use is a PC-based program called ALGOR (SUPERSAP). The ALGOR program does not have the normal disadvantages of PC-based finite element programs i.e. the size of the problem is unlimited. Although the ALGOR program is designed to compute mechanical problems it has a processor which can compute heat transfer problems. So the problem of section 3.3 could have been solved with this program. The results of the heat transfer computation can be combined with a mechanical computation. In contrast with other PC-based programs ALGOR has the feature to include temperature dependent material constants in the computation.

For the probabilistic approach the stress distribution in the whole part has to be known. The parts will not be modelled by axisymmetric elements. Despite of the longer computation time the three dimensional block elements of ALGOR are used to compute the stress. For two ceramic parts of the construction the stress distribution has been computed. These parts are the inner aluminium-oxide tile (fig. 3.15) and the silicon nitride bolt (fig. 3.16). Because of the result of the calculations the radius in the bolt hole of the tile is enlarged from 0.5 mm to 2.5 mm, to make sure that the stress intensity factor at this place is low in order to minimise the crack growth. During our tests the crack has to grow from a well defined crack at a well defined place. Since the stress in the bolt-shaft was the highest stress in the bolt, a little slit was made in the boltshaft.

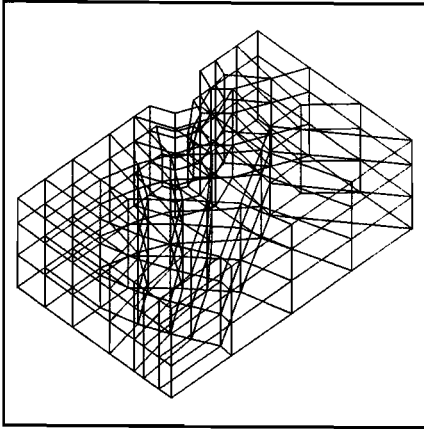


Figure 3.15 Starting mesh in one quarter of the aluminium oxide tile.

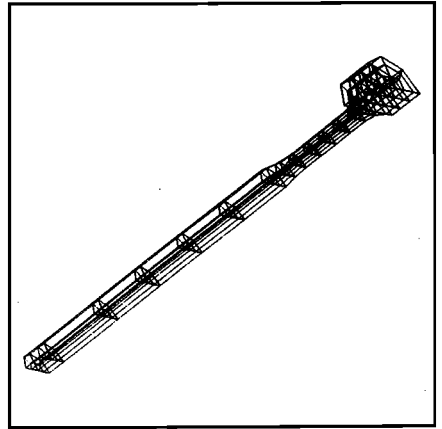


Figure 3.16 Starting mesh in one half of the silicon nitride bolt.

3.6 Probabilistic modelling

3.6.1 Stress volume integral

When measuring the tensile strength of a large number of ceramic tensile bars of certain volume, there will not be found a fixed value of the strength, above which all bars break. Instead there will be found a range of strengths at which the bars break. The strength distribution, which best fits the data of the above tests, is the Weibull distribution given in formula 3.66 [ref. 3.16, 3.17, 3.29 - 3.32].

$$P(\sigma) = 1 - e^{-\frac{V}{V_0} \left(\frac{\sigma - \sigma_u}{\sigma_0} \right)^m} \quad (3.66)$$

σ_u , σ_0 and m , the three parameters of the Weibull distribution, are defined as follows:

- 1 - σ_u is the threshold stress, below which the failure probability is zero. In practice, best estimates of σ_u are relatively small compared to the mean stress. A safe value of σ_u is zero unless there are reasons to expect an upper limit to the size of the crack.
- 2 - σ_0 is a normalising stress. It is the stress at which the probability of failure equals 0.63 if σ_u is zero.

3 - m is the Weibull modulus. It is a measure of the width of the distribution. The higher the value of m the smaller is the distribution. m is a measure of the reliability of the material.

- V = the volume of our test bar [m^3]
- V_0 = a normalising volume e.g. 1 mm^3 [m^3]
- $P(\sigma)$ = probability of failure at stress σ [-]

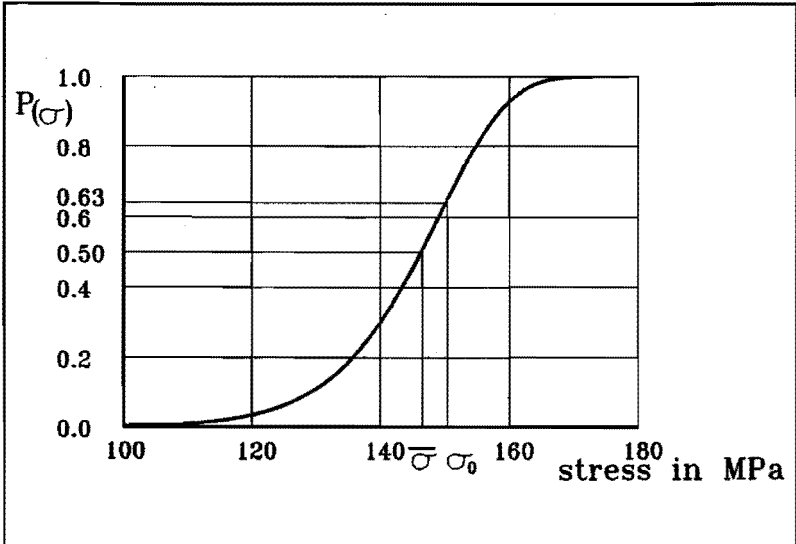


Figure 3.17 Weibull strength distribution of reaction-bonded silicon nitride ($\sigma_0 = 150 \text{ MPa}$, $m = 15$ according to A.M.E.).

- There are some assumptions made while using equation 3.60.
- 1 - The weakest link hypothesis is valid.
 - 2 - The number of flaws in the specimens is large.
 - 3 - Failure must occur for a high stress.

One remark on the value of σ_0 is concerned with manufacturers who want to present the best ceramics. Some manufacturers pretend to give the mean fracture stress $\bar{\sigma}$, but in fact they give σ_0 . As can be seen in figure 3.17, there can be a significant difference in the mean stress and the normalising stress, depending on the value of m .

In section 3.4 was explained that the critical stress intensity factor is a material constant, independent of crack size and distribution. The stress intensity factor is depending on the flaws (location and orientation), stress and flaw size. If for the experiment to determine the Weibull distribution, tensile bars of the same size and orientation from one homogeneous batch of ceramics are used, it can be stated that the

flaw distribution and orientation are the same in all the specimens. The stress intensity factor for the specimens only depends on the stress and the flaw size. A strength distribution has been determined. But since K_{Ic} is the same for all specimens it can be stated that a flaw size distribution has been determined. Figure 3.17 gives the strength distribution of RBSN. The from the strength distribution derived flaw size distribution is given in figure 3.18, supposed the critical stress intensity factor to be independent of the flaw size distribution.

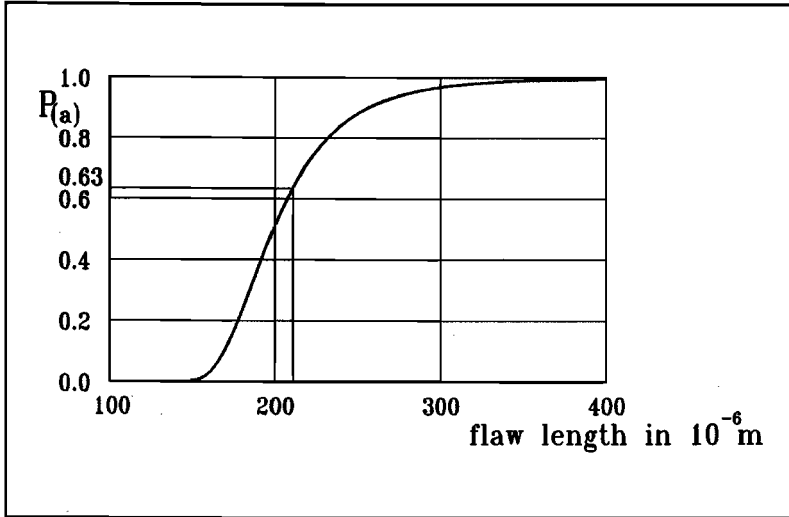


Figure 3.18 Flaw size distribution derived from the strength distribution of the A.M.E. RBSN and a K_{Ic} of $2.5 \text{ MN/m}^{3/2}$.

If the size of the tensile bars is increased, the probability of the inclusion of a large flaw increases. With the same material constant K_{Ic} this will result in a decrease in failure strength. In the tensile bars the stress is uniformly distributed. When using a three point bend test the stress distribution is linear along the bar length and along the bar height. Only at one line in the bar there is a maximum tensile stress. The probability of a large flaw to be located at the same place of the highest stress is small. The failure stress measured at a bend bar, of the same size as the tensile bar, will be higher than the one of the tensile bar. The effects of the size and the stress distribution can be combined as follows. The probability of failure of two volumes v_1 and v_2 with stresses σ_1 and σ_2 are given by formulas 3.67 and 3.68. The probability of failure of a volume of size $v_1 + v_2$ is given by formula 3.69.

$$P_{V_1} = 1 - e^{-\left(\frac{V_1}{V_0}\right)\left(\frac{\sigma_{V_1}}{\sigma_0}\right)^m} \quad (3.67)$$

$$P_{V_2} = 1 - e^{-\left(\frac{V_2}{V_0}\right)\left(\frac{\sigma_{V_2}}{\sigma_0}\right)^m} \quad (3.68)$$

$$P_{V_1+V_2} = 1 - e^{-\left(\frac{V_1}{V_0}\right)\left(\frac{\sigma_{V_1}}{\sigma_0}\right)^m - \left(\frac{V_2}{V_0}\right)\left(\frac{\sigma_{V_2}}{\sigma_0}\right)^m} \quad (3.69)$$

$$= 1 - e^{-\frac{1}{\sigma_0^m V_0} (V_1 \sigma_{V_1}^m + V_2 \sigma_{V_2}^m)}$$

Let the maximum stress in the two volumes be equal to σ_{\max} . The total volume of $v_1 + v_2$ is V .

$$P_V = 1 - e^{-\left(\frac{\sigma_{\max}}{\sigma_0}\right)^m \left(\frac{V}{V_0}\right) \frac{1}{V} \sum_{i=1}^2 v_i \left(\frac{\sigma_{v_i}}{\sigma_{\max}}\right)^m} \quad (3.70)$$

For a large number of small volumes this will become.

$$P_V = 1 - e^{-\left(\frac{\sigma_{\max}}{\sigma_0}\right)^m \left(\frac{V}{V_0}\right) \frac{1}{V} \int_V \left(\frac{\sigma_{v_i}}{\sigma_{\max}}\right)^m dV} \quad (3.71)$$

$$P_V = 1 - e^{-\left(\frac{\sigma_{\max}}{\sigma_0}\right)^m \left(\frac{V}{V_0}\right) \Sigma (v)} \quad (3.72)$$

with Stress Volume Integral S.V.I.: $\Sigma (v) = \frac{1}{V} \int_V \left(\frac{\sigma_i}{\sigma_{\max}}\right)^m dV$ (3.72)

The Stress Volume Integral is a measure of the load of a component. If this integral is small, then only a small volume of the component is subjected to a high stress. For a uniformly distributed stress, as in a tensile bar, this integral equals the value of unity.

The allowable maximum stress of components with different volumes v_1 and v_2 can be compared. If these components should have the same probability of failure the maximum allowable stress for component 1 can be derived if this stress is known for component 2.

$$P_{V_1} = 1 - e^{-\left(\frac{\sigma_{\max 1}}{\sigma_0}\right)^m \left(\frac{V_1}{V_0}\right) \frac{1}{V_1} \int_{V_1} \left(\frac{\sigma_{(v_1)1}}{\sigma_{\max 1}}\right)^m dV} \quad (3.74)$$

$$P_{V_2} = 1 - e^{-\left(\frac{\sigma_{\max 2}}{\sigma_0}\right)^m \left(\frac{V_2}{V_0}\right) \frac{1}{V_2} \int_{V_2} \left(\frac{\sigma(V_1)^2}{\sigma_{\max 2}}\right)^m dV} \quad (3.75)$$

For equal probability of failure $P_1 = P_2$.

$$\sigma_{\max 1}^m V_1 \sum (V_1) = \sigma_{\max 2}^m V_2 \sum (V_2) \quad (3.76)$$

$$\frac{\sigma_{\max 1}}{\sigma_{\max 2}} = \left(\frac{V_2 \sum (V_2)}{V_1 \sum (V_1)} \right)^{1/m} \quad (3.77)$$

How can formula 3.71 be used? It is known that the stress volume integral of a tensile bar equals unity. If the allowable stress $\sigma_{\max 2}$ of a tensile bar of volume v_2 is known then the allowable stress for a tensile bar of volume v_1 can be calculated.

$$\sigma_{\max 1} = \sigma_{\max 2} \left(\frac{V_2}{V_1} \right)^{1/m} \quad (3.72)$$

For a three point bend bar the stress volume integral equals $1/(2(m+1)^2)$. If the volume and the allowable stress for a tensile bar (component 2) is known, for equal probability of failure, the allowable stress in a three point bend bar (component 1) of the same volume will be equal to $\sigma_{\max 1}$ according to formula 3.79.

$$\sigma_{\max 1} = \sigma_{\max 2} \left(\frac{1}{2(m+1)^2} \right)^{1/m} \quad (3.79)$$

Suppose the manufacturer gives the stress distribution parameters σ_0 and m , the size of the test specimen and the kind of test used to measure these parameters. If the stress volume integral for the component used can be computed it is possible to calculate for a component, for an allowable probability of failure, the maximum allowable stress. The next section will deal with the computation of the stress volume integral.

3.6.2 Algor stress volume integral

If the allowable stress for a component is to be compared with the allowable stress given by the manufacturer, the stress volume integral of both the component and the component of the manufacturer should be known. To calculate the stress distribution in the component the volume is divided in small

elements by using the finite element program ALGOR. Since volumes are of interest the component is divided in 3-dimensional blocks, the 8-node bricks of ALGOR. As a result of the F.E.M. computation, ALGOR can produce a file with several stresses.

- 1 - The mean value of the node stresses as a constant stress at the centre of the brick
- 2 - The maximum value of the node stresses as a constant stress at the centre of the brick
- 3 - The minimum value of the node stresses as a constant value at the centre of the brick
- 4 - The stress at the centre of the brick.

The maximum stress of a node will be used as the constant stress throughout the brick. This will result in a higher value of the stress volume integral, which will result in a lower allowable stress.

From the output file of ALGOR first were calculate the volumes of all the bricks that make up the component [ref. 3.33]. Next this file was searched for the highest value of the stress σ_{max} in a wanted direction. With the highest value of the stress in the component, the volume of brick i , the maximum stress in brick i and a given value of the Weibull modul m , the contribution of brick i to the stress volume integral was calculated. The contribution of all bricks was summed to get the stress volume integral of the component.

$$S.V.I. : \sum (V) = \frac{1}{\sum_{i=1}^n V_i} \sum_{i=1}^n \left[V_i \left(\frac{\sigma_{v_i}}{\sigma_{max}} \right)^m \right] \quad (3.80)$$

The calculated stress volume integral strongly depends on the mesh size of the finite element program. If the mesh size is too large (the number of elements too small) then the stress distribution is not smooth. The resulting stress volume integral will be too high since the highest stress will be used for the total volume of the mesh. If the mesh size decreases the stress distribution will become smoother. If the stresses between two adjacent elements do not differ more than ten percent, the calculated stress volume integral will be a good approximation (error < 5%) of the real stress volume integral.

3.6.3 Algor stress surface integral

The stress volume integral can be used if it is assumed that there is a uniform distribution of flaws over the volume of

the element. This is often true. In other cases the flaws are non-uniformly distributed. The flaws at the surface of the ceramic have a larger size than the flaws inside the ceramic. Machining ceramics causes the creation of large surface flaws [ref. 3.34]. Another problem is the fact that most common loads result in the highest stress at the surface of the component. So at the surface of a component will be the largest flaw size and the highest stress. Therefore crack growth initiation at the surface can be of paramount importance. The probability of a surface flaw to grow with the highest speed will be large. As an analogon of the stress volume integral, the stress surface integral will be introduced. If we know the surface condition of both the component and the testpiece, it is possible to compare, with this integral, the allowable stress for a component to the stress given by a manufacturer for his testpieces.

$$S.S.I. = \frac{1}{A} \int_A \left(\frac{\sigma_a}{\sigma_0} \right)^m dA \quad (3.81)$$

S.S.I.	Stress Surface Integral	[-]
A	total surface of component	[m ²]
σ_a	surface stress of one element	[Pa]
σ_0	normalizing stress	[Pa]

For two components with different surfaces, the two allowable stresses, at equal probability of failure, will be according to equation 3.82.

$$\frac{\sigma_{\max 1}}{\sigma_{\max 2}} = \left(\frac{A_2 S.S. I_2}{A_1 S.S. I_1} \right)^{1/m} \quad (3.82)$$

This equation can be used in the same way as equation 3.77. There is a version of ALGOR which can produce an outputfile with all the stresses at all nodes of the used bricks. This version will be used to compute the stress surface integral. When computing the S.S.I., it must be sure that only surfaces of the bricks, that are outer surfaces of the component, are used. The first part of our S.S.I. program determines whether a surface is an outer surface. Next, all the outer surfaces of the bricks of the component are calculated. The outputfile is searched for the highest stress in a wanted direction. The fourth step is the calculation of the contribution of the separate bricks to the S.S.I. The last step is the summation which results in the total stress surface integral. As with the S.V.I. the mesh size should be small enough.

3.6.4 Lifetime calculations

The first subsection will give a flow diagram of the probabilistic method used to design a ceramic part of a construction. The calculation of the lifetime of that part is incorporated in the design. The second subsection will deal with the calculation of the lifetime of a system built up of several ceramic parts.

3.6.4.1 Lifetime calculation of one component

After the decision, which depends on the thermal and mechanical load, to design a ceramic part, some kind of ceramic will be chosen, based on the information of the manufacturers. With this information and the available space in the construction a first decision will be made on the global dimension of the ceramic part. Given the dimensions and the external load, with a finite element program, the stress distribution can be calculated. This will give the maximum stress in the component. If this stress is too large the procedure has to be followed once again. With the extension of ALGOR it is possible to calculate the Stress Volume Integral or the Stress Surface Integral of the component. With the information of the manufacturer and a finite element program the S.V.I. or the S.S.I. used by the manufacturer can be calculated. Since a certain probability of failure has to be accepted the decision has to be made what stress is acceptable in the component.

Based on the information of the manufacturer, tensile stress, critical stress intensity factor and Weibull modulus, the largest crack size in the part can be calculated with the aid of the Monte Carlo method [ref. 3.35]. With the crack growth models as described in this thesis and the crack growth data of the ceramic it is possible to calculate a minimum lifetime of the component (with a certain probability). If this lifetime is too short there has to be started all over again until an acceptable lifetime has been reached. In the end this will lead to a certain stress in the component and to the final design of the component.

3.6.4.2 Lifetime calculation of an MHD generator

A detailed example of the calculation of the lifetime of a system built up of several ceramics parts is given in this

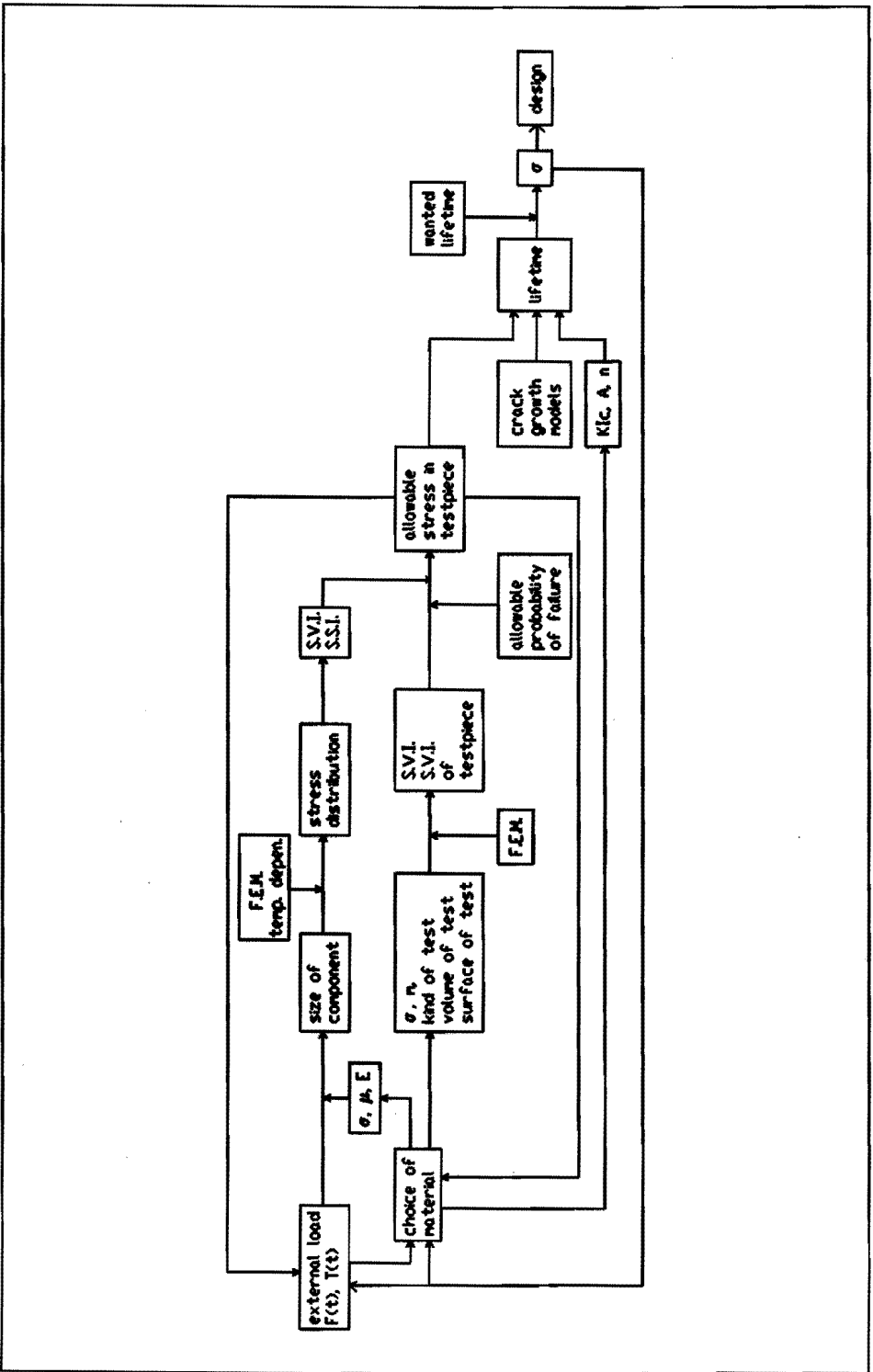


Figure 3.19 Flow chart of the design of a ceramic part.

subsection. The system we consider is a MHD generator channel. Such a channel consists of a tube with rectangular cross section. Along the channel length the cross section increases. The walls of the tube are covered with ceramic tiles. Each tile is connected, by means of a ceramic bolt, to a load carrying back plate. There is a built-in redundancy in the system, by means of the shape of the tiles, in such a way that if one bolt fails the system does not fail. Only if two adjacent bolts fail the system will fail. For the ease of the lifetime calculations the following assumptions are made:

- the walls are rectangular ($6 \times 1 \text{ m}^2$)
- the load on the tile depends only on the pressure fluctuations in the channel
- the pressure fluctuation is constant throughout the channel length
- the bolts are pre-loaded with twice the maximum pressure fluctuation
- the behaviour of the walls is independent from each other.

Assume that the material constants such as the tensile stress, the Weibull modulus and the critical stress intensity factor are known. Further should be known the crack growth exponent, the crack growth constant and the models describing the crack growth.

The lifetime calculation follows the scheme indicated below.

- 1 - From the tensile stress distribution and the critical stress intensity factor we calculate a flaw distribution
- 2 - By means of the Monte Carlo method every bolt is assigned a largest flaw out of the distribution
- 3 - The load is equally distributed over the bolts
- 4 - The lifetime of the bolt with the largest flaw is calculated
- 5 - At that time the size of the flaws in all the bolts is calculated
- 6 - Due to the failure of one bolt a redistribution of the load over the bolts is calculated
- 7 - With the new load and with the new "initial flaw" the lifetime of all the bolts is calculated
- 8 - The bolt with the shortest lifetime will fail next
- 9 - If this bolt is adjacent to a bolt which failed earlier, the system will fail
- 10 - If this bolt is not adjacent to a bolt which failed earlier we go back to point 5.

Formulas on which this scheme is based are:

- the time to failure according to formula 3.34

$$t_f = \frac{2}{AY^2\sigma^2(n-2)K_{Ic}^{n-2}} \left(\left(\frac{K_{Ic}}{K_I(0)} \right)^{n-2} - 1 \right) \quad (3.83)$$

- the flaw size at time t deduced from formula 3.31

$$a(t) = \frac{1}{\sigma^2 Y^2} \frac{1}{(K_I^{2-n}(0) - \frac{(n-2)AY^2\sigma^2 t}{2})^{\frac{2}{n-2}}} \quad (3.84)$$

- the stress distribution

$$P_{(\sigma)} = 1 - e^{-\left(\frac{\sigma}{\sigma_0}\right)^n} \quad (3.85)$$

- the definition of the stress intensity factor

$$K_{Ic} = Y\sigma\sqrt{a} \quad (3.86)$$

Combination of formula 3.85 and 3.86 will give us an expression of the flaw size a:

$$a = e^{(\ln(a_0) - \frac{2}{m} \ln \ln(\frac{1}{P(a)}))} \quad (3.87)$$

The probability of flaw length a is a number between zero and unity which can easily be generated by the random generator of a computer. Using such a random number in formula 3.87 gives a certain flaw size. For a large number of flaw sizes, calculated in this way, the flaw size distribution equals the distribution of figure 3.18.

By means of the above scheme it is possible to calculate the lifetime of a MHD generator. With material data and with chosen crack growth data this lifetime was calculated for a number of situations. The starting situation is: a tensile stress of 150 MPa, a Weibull modulus of 15, a load of 60 MPa and a stress intensity factor of 2.5 MN/m^{3/2}. The number of bolts in one wall is equal to 150.

The parameters that will be changed are:

- the load on the bolts,
- the Weibull modulus of the strength distribution,
- a proof load for all the bolts,
- a lower load on the outer bolts,
- the number of bolts on one wall,
- the arrangement of the tiles on the wall.

For the three different arrangements of the tiles on the wall (fig. 3.20) the parameters are changed one by one. The other parameters are kept at their normal (starting) value described above. For every parameter the lifetime of the system MHD channel is calculated one thousand times. The lifetime is assumed to be distributed according to a Weibull distribution. The characteristic lifetime of a generator is defined as the time at which 63 % of the generators failed. This characteristic lifetime is given in the next figures. For the first series of experimental MHD generators a characteristic lifetime of 1000 hours (3.6×10^6 s) should be established. The results of the change in load on the bolts are given in figure 3.21. The results of the change in Weibull modulus are given in figure 3.22. The results of the change in proof load are given in figure 3.23. The results of reduction of the load on the outer bolts are given in figure 3.24. The results of the change in the number of bolts are given in figure 3.25. More detailed information on the figures is given in appendix E.

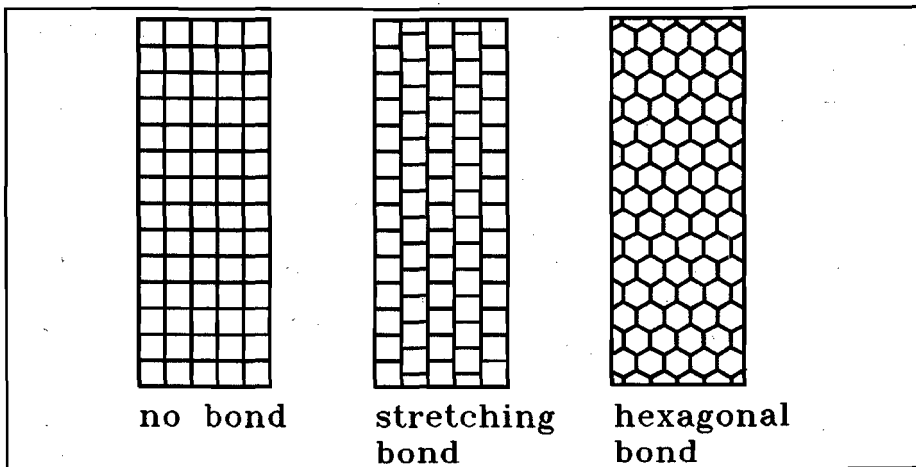


Figure 3.20 Three different arrangements of the tiles on the wall.

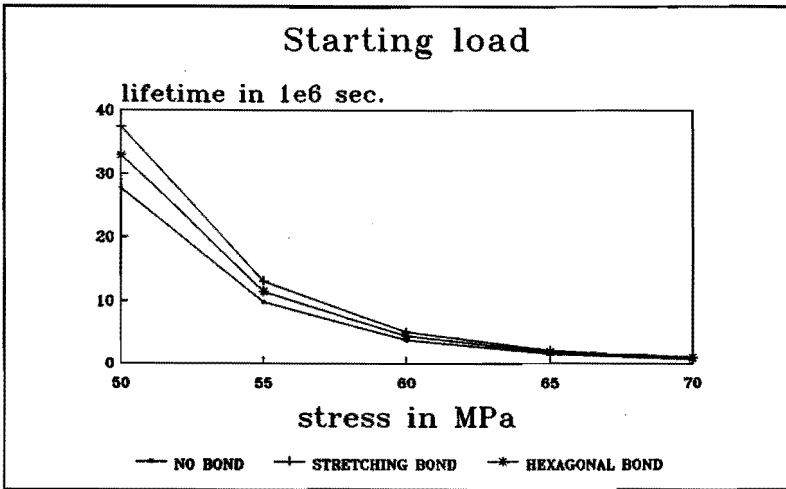


Figure 3.21 Lifetime as function of load on the bolts.

As can be seen in figure 3.21 the lifetime of generator decreases with an increase of the stress in the bolts. This is expected. The decrease in lifetime is not a linear function of the increase in stress.

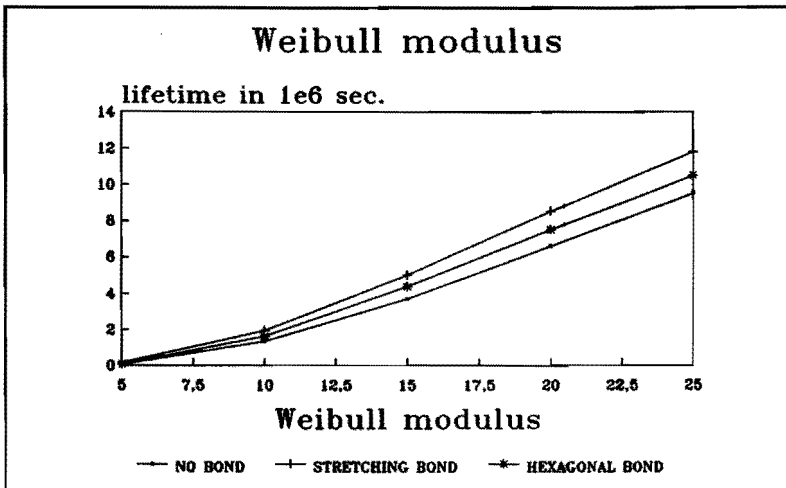


Figure 3.22 Lifetime as function of Weibull modulus of RBSN.

A high Weibull modulus indicates a sharp distribution of the cracks around the mean crack size. For RBSN with a high Weibull modulus only a few bolts will have large cracks. After failure of these bolts the stress intensity factors, in the remaining bolts, will be low due to the small crack sizes, which results in a slow crack growth and long lifetime.

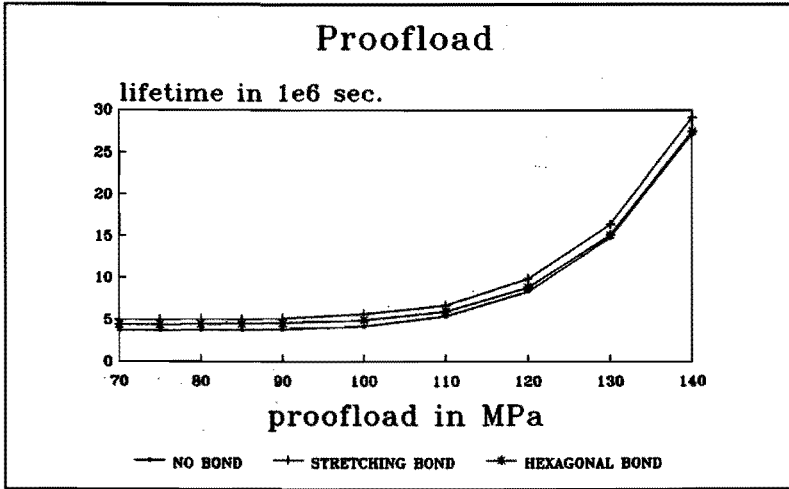


Figure 3.23 Lifetime as function of the proofload.

During applying of a high proofload, bolts with a large included cracks will fail. The remaining bolts will have small cracks. The small crack size together with the low stress, during normal use, results in a small stress intensity factor. This leads to slow crack growth and a long lifetime.

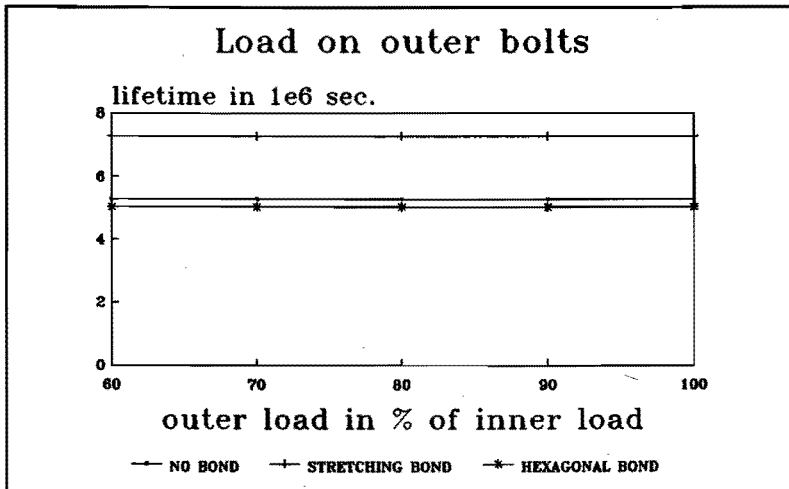


Figure 3.24 Lifetime as function of the relative load on the outer bolts.

After failure of an outer bolt, the load on this bolt will be distributed over less bolts than after failure of an inner bolt. It was expected that this would influence the lifetime. No influence on the lifetime can be seen in figure 3.24.

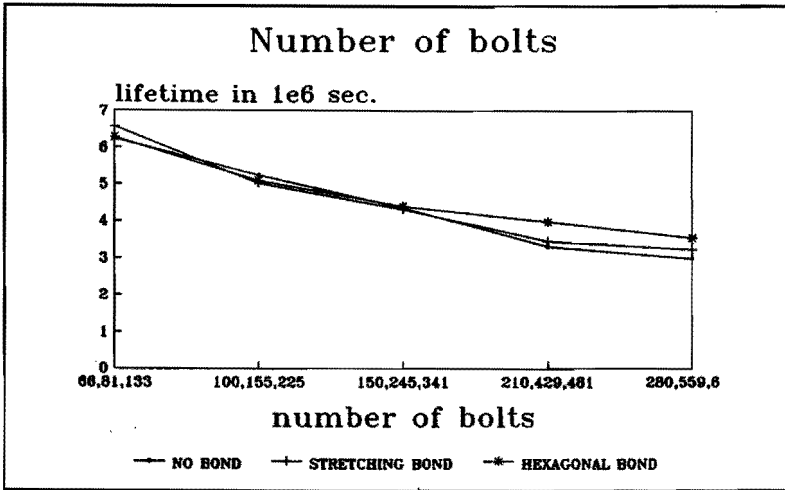


Figure 3.25 Lifetime as function of the number of bolts used.

While increasing the number of bolts the stress in the bolts is kept at a constant value of 60 MPa. More bolts results in a higher probability of a large crack. This will result in a decreasing lifetime.

Looking at the last five graphs we can state that an increase in the stress on the bolts results in a decrease of the systems lifetime compared to the normal condition. An increase in the stress in the bolts results in a smaller number of bolts. A smaller number of bolts results in a longer lifetime of the system. An optimum between load on the bolt and number of bolts should be established.

The expected lifetime of the system varies linear with the Weibull modulus. So effort to increase this modulus will be well paid.

Prooftesting of the bolts has only a significant influence on the lifetime, if the proofload approaches the tensile stress of the material. Due to such a high proof load a large number of bolts will fail during testing. Since the cost of a bolt is small compared to the cost of an overhaul of the complete system, it is worthwhile to test all the bolts with a high proofload.

Reducing the load on the outer bolts has no significant influence on the lifetime of the system.

References chapter 3

- 3.1 Balemans, W.J.M. e.a.: "Meetserie 7", internal report, Technische Hogeschool Eindhoven, 1985.
- 3.2 Shearer, Lowen J. e.a.: "Introduction to system dynamics", Reading, 1971.
- 3.3 Hoek, W. van der: "Het voorspellen van het dynamisch gedrag en positioneringsnauwkeurigheid van constructies en mechanismen", Technische Hogeschool Eindhoven, 1984.
- 3.4 Smeets, M.C.M.: "Warmtetechnische beschouwingen aan een 5 MW blow down installatie", internal report, Technische Hogeschool Eindhoven, 1980.
- 3.5 "VDI - Wärmeatlas", VDI - Verlag GmbH, Düsseldorf, 1977.
- 3.6 Evans, A.G., "Fracture mechanics of ceramics", New York, Plenum Press, 1976.
- 3.7 Morrel, R., "Handbook of properties of technical and engineering ceramics", Londen, 1985.
- 3.8 Chalmers, B. e.a., "Progress in material science", vol. 21, no 3/4, Pergamon Press, Oxford, 1976.
- 3.9 Riley, F.L., "Nitrogen ceramics", pag. 451-487, Elsevier Publishers, Leiden, 1977.
- 3.10 Buresch, F.E. e.a., "Festigkeitskennwert für die sicherheitstechnische Auslegung keramischer Komponenten von Energierzeugungsanlagen", KFA-2102, Jülich, 1986.
- 3.11 Bethge, D., "Hochtemperaturkriechen und langsame Rissausbreitung in keramischen Werkstoffen mit Glasphase am Beispiel des HPSN", dissertation, KFK-4096, Karlsruhe, 1986.
- 3.12 Porz, F., "Reaktionsgesintertes Siliziumnitride: Charakterisierung, Oxidation und mechanische Eigenschaften", dissertation, KFK-3375, Karlsruhe, 1982.
- 3.13 Steinmann, D., "Untersuchung de langsamen Risswachstums von heissgepresstem Siliziumnitrid bei hohen Temperaturen", dissertation, Karlsruhe, KFK-3414, 1982.

- 3.14 Paris, P. e.a., "A critical analysis of crack propagation laws", Transaction of the ASME, pag. 528-534, 1963.
- 3.15 Wiederhorn, S.M. e.a., "An error analysis of failure prediction techniques derived from fracture mechanics", Journal of The American Ceramic Society, vol 59, no. 9-10, 1976.
- 3.16 Jakus, K. e.a., "Analysis of fatigue data for life-time predictions for ceramic materials", Journal of Materials Science, vol 13, 1978.
- 3.17 Gulden, M.E. e.a., "Stress corrosion of silicon nitride", Journal of The American Ceramic Society, vol. 59, no 9-10, 1976.
- 3.18 Bradt, R.C. e.a., "Concepts, flaws and fractography", proceedings symposium, Plenum Press, 1974.
- 3.19 Fett, T., "Lebensdauervorhersage an keramischen Werkstoffen met den Methoden der Bruchmechanik bei elastischem und viscoelastischem Materialverhalten", dissertation, Karlsruhe, 1983.
- 3.20 Evans, A.G. e.a., "Structural Ceramics", Progress in Material Science, Pergamon Press Ltd., Oxford, 1976.
- 3.21 Jayatilaka, A. de S., "Fracture of engineering brittle materials", Applied Science Publishers LTD., London, 1979.
- 3.22 Salah, U.D. e.a., "Creep deformation of reaction sintered silicon nitrides", Journal of The American Ceramic Society, vol. 58, no 11-12, 1975.
- 3.23 Sass, F. e.a., "Dubbels Taschenbuch für den Maschinenbau", Springer-Verlag, Berlin, 1961.
- 3.24 Tada, H. e.a., "The stress analysis of cracks handbook", Paris Productions Inc., St. Louis, 1985.
- 3.25 Roark, R.J. e.a., "Formulas for stress and strain", McGraw-Hill Inc., Tokyo, 1975.
- 3.26 Peterson, R.E., "Stress concentration factors", John Wiley & Sons Inc., New York, 1974.

- 3.27 Fenner, R.T., "Engineering elasticity", Ellis Horwood Ltd., Chichester, 1986.
- 3.28 Schmitt, W., "Numerical methods in fracture mechanics", Fracture of non-metallic materials, p. 47-74., Reidel Publishing company, Dordrecht, 1987.
- 3.29 Davies, D.G.S., "The statistical approach to engineering design in ceramics", Proceedings of the British Ceramic Society, no. 22, London 1973.
- 3.30 Lewis, D. e.a., "An experimental test of the Weibull scaling theory", Journal of The American Ceramic Society ", vol. 59, no. 11-12, 1976.
- 3.31 Hastings, N.A.J.H., "Statistical distributions", the Butterworth Group, London, 1974.
- 3.32 Weibull, W., "Statistical distribution function of wide applicability", Journal of Applied Mechanics, vol. 18, 1951.
- 3.33 Franken, G.J.A., "Spannings-volume-integralen m.b.v. finite element analysis: impementaties in 'c'", Internal report, Eindhoven University of Technology, 1990.
- 3.34 Saurwalt, J.J., "Construeren in keramiek, bepaling van de buigsterkte", symposium Mikrocentrum West, Delft, 1988.
- 3.35 Endrenyi, J., "Reliability modelling in electric Power Systems", John Wiley & Sons, Toronto, 1978.

4 Measurements

4.1 Introduction

One of the main issues of this thesis is the lifetime of a ceramic bolt. The measurements concerned with this item will be dealt with in the section 4.2. In chapter 3 there was presented a model of the dynamical behaviour of the wall segment. Measurements on one of the earlier versions of the segment, in the cold situation, will be given in section 4.3. The results of the thermal measurements will be compared with the results obtained from the model, as described in chapter 3. This comparison will be given in section 4.4.

Additional measurements involved in this project will also be given in this chapter. These measurements were carried out to:

- prepare the testbolt,
- determine the thermal and chemical attack on the bolt,
- improve the loading system of the testbolt.

The received testbolts had a certain machined surface. To make sure that there was a set of equal testbolts they were ground in the workshop. This is discussed in section 4.5. According to the strength distribution theory of section 3.6, weak bolts, with large included cracks, should first fail during tensile tests. The results are discussed in section 4.6. Starting cracks of a given length can be made by various ways. The first idea of using Vickers indentations and the saw slit that was used are discussed in section 4.7.

A number of bolts failed long before the expected lifetime. The bolts did not fail at the notch introduced, but near the bolt head. Chemical attack from the environment by gas or by a liquid surface layer could have caused a decrease in strength. Poor distribution of sintering aids can locally decrease the strength of the material. Phase transformation, at the testing temperature will decrease the strength. These possibilities are described in section 4.8. Due to the construction of the wall segment, a bending moment can be introduced to the bolt. Since ceramics do not deform plastically this leads to high stresses near the bolt head. The loading of the testbolt will be described in section 4.9. Measurements on an improved loading construction of the testpiece are given in section 4.10.

4.2 Results of lifetime measurements

The aim of the lifetime experiments was to determine the crack growth parameters A and n by means of a number of quasi static experiments. This will be done in the first quasi static experiments in which the stress increase velocity will be significantly changed from one series of runs to the other series of runs. With the crack growth parameters the lifetime of a dynamic experiment will be calculated, according to the model of section 3.4. This lifetime will be verified by a second series of quasi static experiments with a dynamical load superimposed on the static load.

All these experiments were performed with the ceramic bolt (as part of the designed MHD generator wall segment) positioned in the oven. The experiments performed will briefly be presented in chronological sequence. At several points in this section an overview of a series of experiments will be given. A comprehensive description of the measurements will be given in appendix F.

The oven has the capability to heat up from room temperature to 1773 K in 2 hours. To minimize the thermal load on the alumina tile the oven is programmed to heat up in 4 hours and to cool down in 8 hours. Independent of the starting temperature or of the final temperature this heating schedule was followed. During the heating up cycle the bolt was loaded with a small force. This was necessary to position the inner tile of the testpiece during inserting in the oven. While heating up the wall segment, the load on the bolt changed slightly due to the difference in thermal expansion of the several parts. The starting preload was approximately 10 MPa. During the heating up cycle this decreased till 5 MPa. At the desired steady state temperature the preload was adjusted to approximately 10 MPa. The first experiments were carried out in an air atmosphere. All bolts have a small slit (radius 0.14 or 0.03 mm).

The first runs were used to get familiar with the test-rig. During these runs two bolts broke prematurely due to a power failure. The cooling of the wall segment and the control system of the oven were improved. It was also noticed that the bolts did not break at the saw slit but near the bolt head. This bolt head was often covered with a reaction layer. Some experiments were performed to investigate this layer. During the first runs the load was kept at a constant value of 9.7 MPa. The excitator was used for half an hour in run six. The most important data of the first seven runs are given in table 4.1. Remarks on these runs are compiled in table 4.2. The

character behind the run number is A for the upper bolt and B for the lower bolt.

Table 4.1 Data of the first seven runs. The bolts of run 2 broke during run 5.

run	envi- ron- ment	initial stress MPa	oven temp. K	initial notch depth 10^{-3} m	failure stress MPa	life- time 10^3 sec
1A	air	10	673	0.3	10	?
2A,B	air	10	1679	0.3	-	
3A,B	air	10	1208	0.3	-	
4A,B	air	10	1773	0.3	-	
5B	air	10	1773	0.3	4	70.0
6A,B	air	10	1773	0.3	10	5
7A,B	air	10	1773	0.3	10	4

Table 4.2 Remarks on the first seven runs.

run	location of fatal fracture	moment of fatal fracture	remarks
1A	saw slit	during heating	premature failing
2A,B	-	-	epoxy burning
3A,B	-	-	burn optical system
4A,B	-	-	one hour at 1773 K
5B	near bolt head	during cooling	one hour dynamic load
6A,B	near bolt head	at high temp.	
7A,B	near bolt head	during cooling	power failure

After these runs some experiments were performed to investigate the reactivity between RBSN and some other materials which will be dealt with in section 4.8. This is also given in appendix F.

After these experiments the lifetime measurements were continued. In the following runs the stress was slowly increased stepwise. The data of the next four runs are given in table 4.3 and the remarks on these runs are given in table 4.4. More information on these runs is given in appendix F.

Table 4.3 Data of runs eight to eleven.

run	environment	initial stress MPa	oven temp. K	initial notch depth 10^{-3} m	failure stress MPa	life-time 10^3 sec
8B	argon	10	1773	0.3	70	1.037
9A	argon	10	1773	0.3	90	691
10A	air	10	1573	0.6	-	
11B	air	10	1573	0.6	max. 88	

Table 4.4 Remarks on runs eight to eleven.

run	location of fatal fracture	moment of fatal fracture	remarks
8B	bolt head	-	-
9A	bolt head	-	-
10A	bolt head	during cooling	loos screw thread
11A	bolt head	during cooling	computer failure

It can be stated that run 8 and run 9 are in agreement with expectations derived from the theory presented in section 3.4. A small stress increase velocity should result in a long life-time and a small failure stress. A larger stress increase velocity results in a shorter lifetime and a higher failure stress. Although the measurements are in agreement with the theory some features were noticed which indicated that the theory did not describe all the processes in the bolt. In spite of the argon flush, the surface of the bolt was still covered with a brown layer. The fatal crack did not originate from the saw slit. These features will be dealt with in sections 4.8 and 4.9. As result of the investigations (described in sections 4.8 and 4.9) as to these features it was decided to take the following actions:

- decrease the testing temperature from 1773 K to 1573 K to stop the transformation from α -RBSN to β -RBSN which has a lower strength
- stop the flushing with argon because it has no effect on the oxidation mechanism
- increase the notch from a depth of 0.3 mm to a depth of 0.6 mm to increase the local stress intensity factor

- use, at the cold side, a spring leaf suspension system to decrease the bending moment in the bolt
- use at the hot side the ball-and-cup system to decrease the bending moment in the bolt.

With the spring leave system and the ball-and-cup system, a large number of experiments were performed, at room temperature, to determine their influence on the bending moment in the bolt. The results of these experiments are presented in section 4.10. As expected both systems reduced the bending moment significantly. Both systems were incorporated in the high temperature wall segment.

To increase the influence of the saw cut on the stress distribution in the bolt, the depth was enlarged from 0.3 mm to 0.6 mm. The load was stepwise adjusted by tightening the nut on the bolt in run twelve. To prevent breaking of the bolt during the increase of the stress, from run thirteen on, the stress was remotely increased by adjusting the pressure in an air cylinder beneath the bolt nut. To make sure that the fatal crack originated from the saw slit, this slit was again enlarged to 0.9 mm from run fourteen on. The main data of runs 14 till 18 will be given in table 4.5. Remarks on these runs will be given in table 4.6. More information on these runs is given in appendix F.

Table 4.5 Data of runs 12 to 18.

run	environment	initial stress MPa	oven temp. K	initial notch depth 10^{-3} m	failure stress MPa	life-time 10^3 sec
12A	air	6	1573	0.6	111	1,105
13B	air	6	1573	0.6	202	1,175
14A	air	9	1573	0.9	211	434
15A	air	9	1573	0.9	227	661
16A	air	9	1573	0.9	224	3.36
17A	air	9	1573	0.9	279	4.56
18A	air	9	1573	0.9	229	5.04

Table 4.6 Remarks on runs 12 to 18.

run	location of fatal fracture	moment of fatal fracture	remarks
12A	bolt head	during loading	transverse force
13B	bolt head	-	-
14A	saw slit	-	-
15A	saw slit	-	-
16A	in colder part	-	failure spring leaf system
17A	near saw slit	-	flaw in material
18	in colder part	-	flaw in material

Some bolts still broke at a natural flaw. To increase the effect of the saw slit its radius was decreased from 0.14 mm to 0.03 mm as is explained in section 4.7. With this smaller radius in the bottom of the saw slit the other experiments were performed. During runs 22 to 24 besides the pre-load also the dynamic load was slowly increased. It was intended to let the dynamic load be 50 % of the pre-load but only a dynamic load of 10 % was achieved. This was due to a weak air cylinder in the load chain. The data of these experiments are given in table 4.7, the remarks in table 4.8 and the descriptions in appendix F.

Table 4.7 Data of runs 19 to 24.

run	environment	initial stress MPa	oven temp. K	initial notch depth 10^{-3} m /radius	failure stress MPa	life-time 10^3 sec
19	air	9	1573	0.9/0.03	118	2.40
20	air	10	1573	0.9/0.03	139	2.82
21	air	10	1573	0.9/0.03	93	242
22	air	10	1573	0.9/0.03	110	2.28
23	air	10	1573	0.9/0.03	69-103	102-158
24	air	10	1573	0.9/0.03	125	159
25	air	10	1573	0.9/0.03	94	152

Table 4.8 Remarks on runs 19 to 24.

run	location of fatal fracture	moment of fatal fracture	remarks
19	saw slit	during reloading	ball-and-cup fracture
20	saw slit	-	-
21	saw slit	-	-
22	saw slit	-	dynamic loading 0.1 x load
23	saw slit	unknown	failure of data-acquisition system
24	saw slit	-	-
25	saw slit	-	-

From these runs only runs with bolts with a saw slit depth of 0.9 mm will be used to determine the crack growth constants n and A . Run 14 and run 15 will both be used. Run 16 will not be used because the bolt broke due to a failure of the leaf spring system. Although the bolt of run 17 broke just beside the saw slit, the data will be used because the temperature at that place was almost equal to the temperature in the saw slit. The width:depth ratio of the flaw in the bolt was smaller than the width:depth radius of the saw slit. The data of run 18 will not be used because the fatal crack was too far away from the saw slit. Due to a failure of the ball-and-cup system the bolt of run 19 could not rotate in the alumina tile. During re-adjusting of the load the bolt broke. The data of this run will not be used. Data of runs 20, 21, 22, 23, 24 and 25 will be used.

The runs used are plotted in figure 4.1. The lines through the failure points of matching runs should be parallel if a similar crack growth exponent n for all the runs exists. If the bolt of run 17 had broken at the saw slit, it would have been at a higher stress. Due to a difference in crack geometry sharper saw slits will result in a shorter lifetime. The results of runs 22-25 are not contradicting the influence of the dynamic loading.

By a combination of several experiments the following crack growth constants can be deduced (table 4.9).

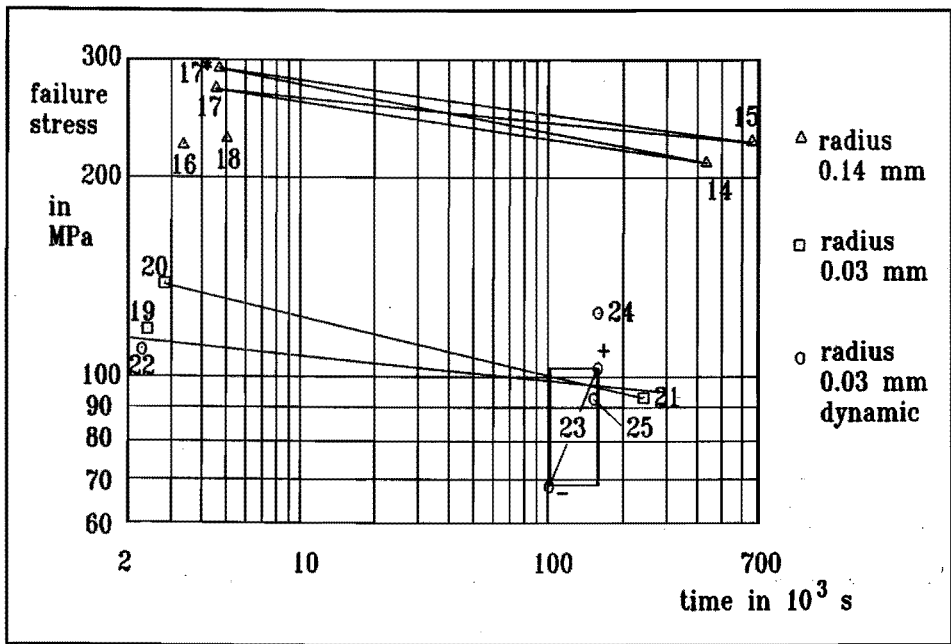


Figure 4.1 Results of the lifetime-measurements.

Table 4.9. Crack growth constants of RBSN

experiments	crack growth exponent n	crack growth constant A
14 and 17	n = 18	A = 1*10 ⁻⁹⁹
14 and 17*	n = 13	A = 1*10 ⁻⁸⁹
15 and 17	n = 27	A = 1*10 ⁻¹²¹
15 and 17*	n = 19	A = 1*10 ⁻¹⁰²
20 and 21	n = 11	A = 1*10 ⁻⁸⁰
14 - 21	n = 18 ± 6	A = 1*10 ^{-99±14}

As an overall result it can be concluded that RBSN shows a time dependent failure behaviour. If this time dependent behaviour is described by the subcritical crack growth models of section 3.4, then the crack growth constants n and A can be deduced from the above experiments. For the RBSN of AME this results in equation 4.1 describing the slow crack growth at an oven temperature of 1573 K in air.

$$v = 1.0 \cdot 10^{-99} K_I^{18} \tag{4.1}$$

For the mean n from table 4.9 a line is drawn through the points of runs 22 till 25 in figure 4.1. As can be seen there is a wide spread between the mean line through these points and the points themselves. This can be due to the influence of small natural flaws in the bottom of the saw slit. The spread of the points around the line gives no verification of the correctness of the subcritical crack growth model under dynamic load. It is possible that the crack growth behaviour can be described by that model. More tests should be performed to prove this statement.

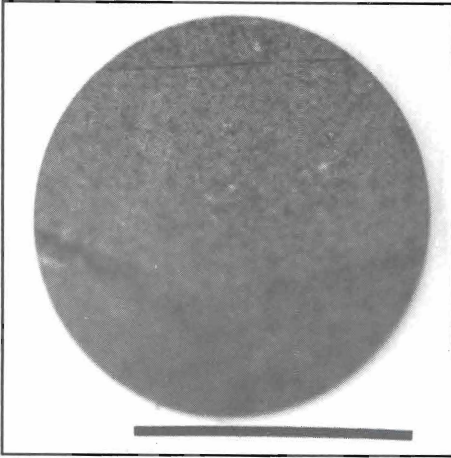


Figure 4.2 Crack surface of run 14 originating from saw slit. Flat region near saw slit, rough region and shear lips. Bar = 5 mm.

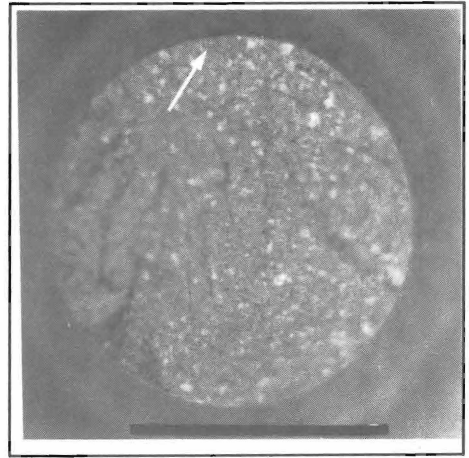


Figure 4.3 Crack surface of run 17. Crack originated from natural flaw (arrow). Bar = 5 mm.

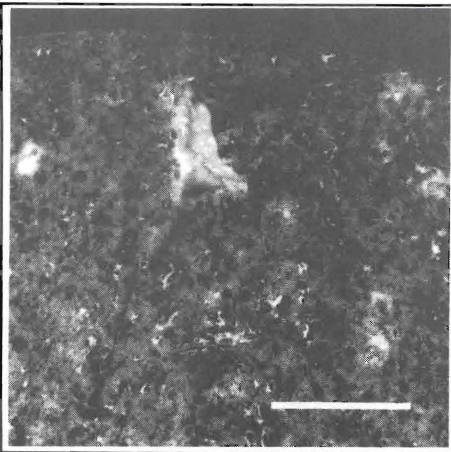


Figure 4.4 Natural flaw from which the crack originated during run 17. Bar = 0.5 mm.

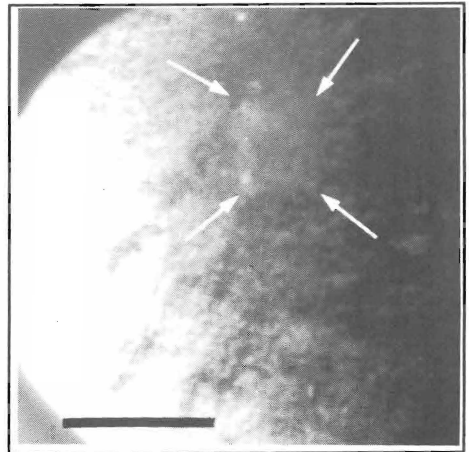


Figure 4.5 Large inclusion on the crack surface of run 18. Bar = 2 mm.

The measurements of figure 4.1 can be translated to a K_I - v diagram more commonly in use (fig. 4.6). Some typical crack surfaces are given in figures 4.2 to 4.5.

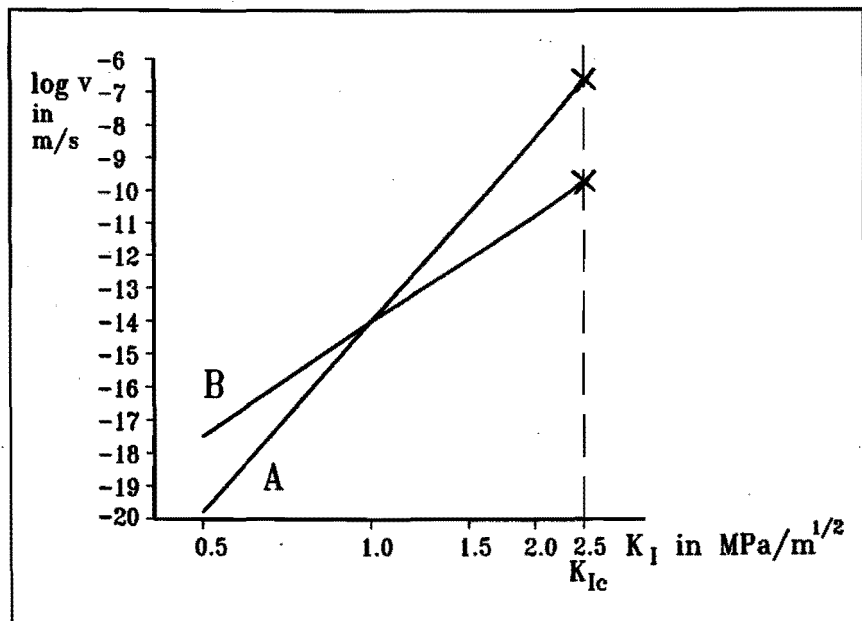


Figure 4.6 K_I - v diagram for the RBSN used. Curve A slit radius 0.14 mm. Curve B slit radius 0.03 mm.

4.3 Dynamical behaviour of the wall segment

The dynamical behaviour of the wall segment has been calculated using the models presented in section 3.2. These calculations were performed with material data for room temperature. The results of these calculations are given in table 4.9. The acceleration of the inner tile and of the steel back are measured. The acceleration of the inner tile is measured by means of the laser-interferometer. An accelerometer is used to measure the acceleration of the steel back plate. The Youngs modulus of the Zircar had to be adjusted to bring the calculated accelerations in line with the measurements. The manufacturer Youngs modulus and the Youngs modulus used are given in table 4.10.

The dynamical behaviour of the wall segment was only measured and calculated at room temperature. Due to the mechanical improvements (e.g. spring leaf system) in the design the dynamical behaviour will change. These improvements are not

accounted for in the models. Also the influence of the temperature dependency of the Youngs moduli is not accounted for.

Table 4.10 Comparison of measured and calculated values of the accelerations and forces.

	acceleration of inner plate	Youngs modulus Zircar 1) given by ICI 2) own measurement	force in bolt
calculation	555 m/s ²	1) 117 MPa	1250 N
measurement	538 m/s ²	2) 78 MPa	1210 N

By placing the accelerometer along the mirror on the inner tile, the laser interferometer can be checked. The results of these measurements are given in figure 4.7. It can be concluded that the acceleration of the inner tile can be measured by means of the laser-interferometer at room temperature.

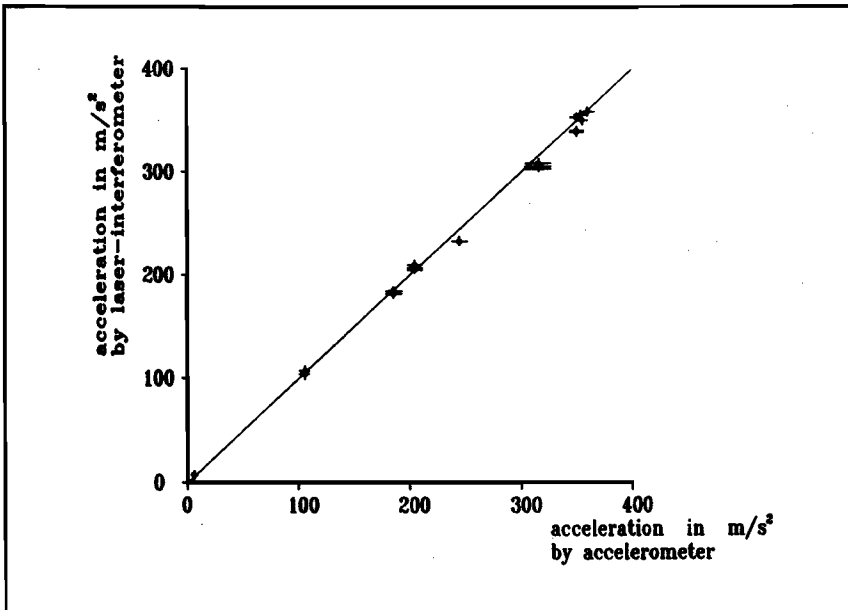


Figure 4.7 Comparison of the measurement of the acceleration of the inner tile by means of an accelerometer (x-axis) and by means of the laser-interferometer (y-axis).

The laser-interferometer has been used at high oven temperature to measure the acceleration of the inner tile. Due to oxidation and evaporation of the platinum mirror, the laser-interferometer could only be used for a short time.

4.4 Thermal measurements

In section 3.3 a thermal model of the testpiece was presented. As one of the boundary conditions for this model a oven temperature of 1773 K was assumed. During the runs this oven temperature has been reduced to 1573 K. For this new boundary condition the same model has been used to calculate the temperature profile. The results from these calculations were compared with the temperature measurements in the wall segment. The thermocouples in the wall segment were placed in seven distinct places. These places are indicated from TCA to TCG in figure 4.8.

The calculations (fig. 4.8) did not agree with the measurements. So the model has to be adapted. This adaptation is performed in two steps. In the first step the temperature dependent heat conduction coefficients of the alumina, the Zircar and the epoxy are adjusted in such a way that the calculated temperatures are in good agreement with the measured values (TCA - TCE).

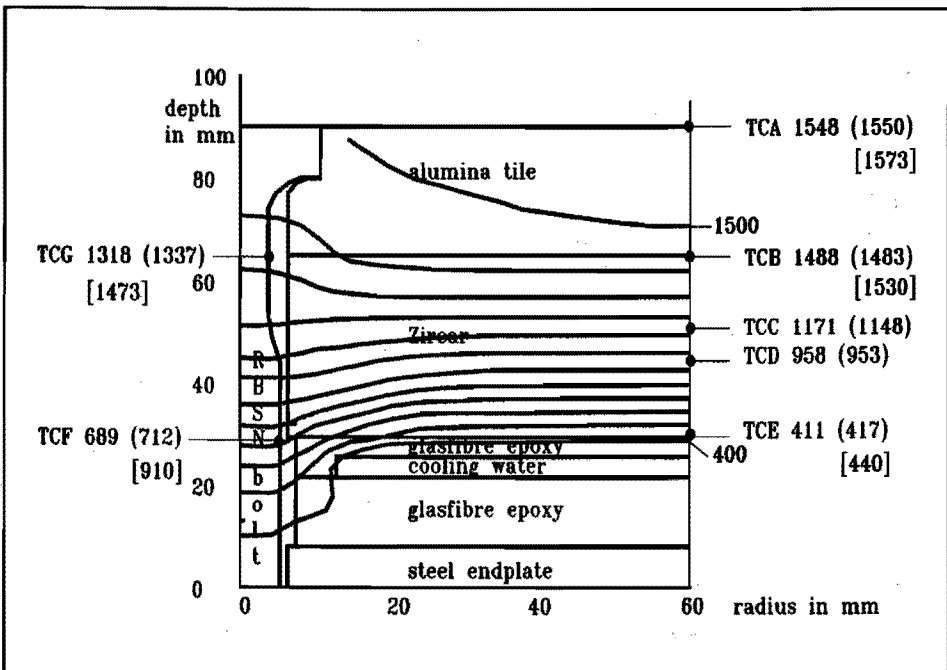


Figure 4.8 Result from the thermal calculations for the testpiece in an oven at 1573 K. Indicated are the thermocouples and the measured temperatures. The calculated temperatures for material data of the manufacturer are placed between brackets and for adjusted material data between parentheses.

In the second step the heat conduction coefficient of the RBSN and the heat transfer coefficient in the slit between the bolt and the tile and Zircar is adjusted to bring into line the calculated values with the measured values (TCF, TCG). The results from the calculations and from the measurements are presented in figure 4.8.

The heat conduction coefficient of the alumina had to be decreased in comparison with the data of the manufacturer. A broken alumina tile showed a not completely sintered interior. The heat conduction coefficient of the Zircar had to be increased. Due to the pressure on this material it is compressed. The contact between the fibers is enhanced and the insulating air is diminished. This result in a better heat conduction. The heat conduction of the RBSN had to be increased in comparison with the manufacturers data. The heat transfer between the bolt and the surrounding had to be enlarged as well. The model is not adjusted for the heat transfer inside and outside the oven which could also influence the differences between measured and calculated temperatures. The result from the measurements and calculations are used in the calculation of the stress distribution in the bolt. Figure 4.9 gives an indication of the difference between the used material data and the given material data.

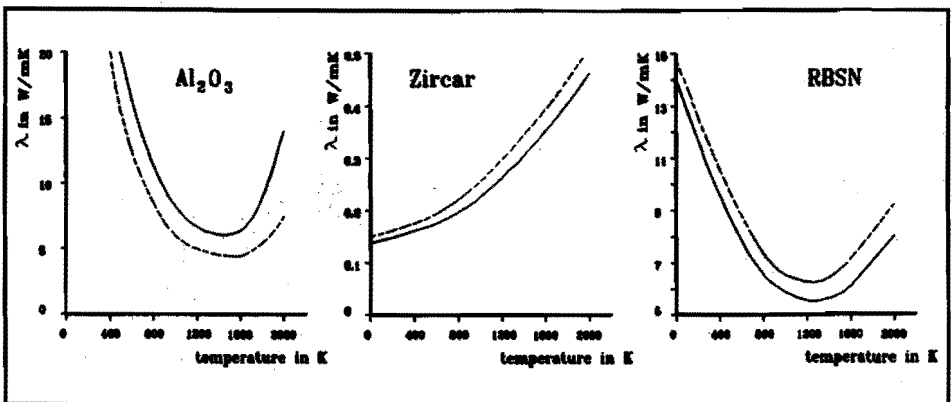


Figure 4.9 Differences between the heat conduction coefficients given by the manufacturer (continuous lines) and the used heat conduction coefficients (dashed lines).

4.5 Grinding

In the green stage after presintering the RBSN bolts are machined to net shape. As can be seen from the received bolts this machining is done on a lathe. The machining grooves are perpendicular to the axis of the bolt. These grooves act as

notches. In the reduced diameter part of the bolt there should not be any other crack, perpendicular to the load, except from the saw slit introduced on purpose. To remove the machining grooves the bolts have been ground. Grinding removed $100\ \mu\text{m}$ from the surface of the bolt. The machining grooves introduced by the grinding are parallel to the axis. Since the cracks, eventual resulting from this grinding, are parallel to the load they have no influence on crack initiation.

Together with the reduced part of the bolt the contact surface of the bolt head has been ground in one clamp. In this way the contact surface of the head is perpendicular to the axis of the bolt. Grinding parameters are:

- grinding speed 6.28 m/s
- feeding speed $0.7 \cdot 10^{-3}$ m/s
- size of diamond grains $50 \cdot 10^{-3}$ m.

As a result of this machining no microscopically visible cracks, except from the natural pores, could be detected. The machining grooves are visible, see figure 4.10. The roughness has been measured by an instrument developed by the faculty of mechanical engineering of the Technical University Eindhoven. With this instrument it is possible to measure the roughness of curved surfaces. The roughness turned out to be $10.4\ \mu\text{m}$. Figure 4.11 gives a three dimensional representation of the measured roughness.

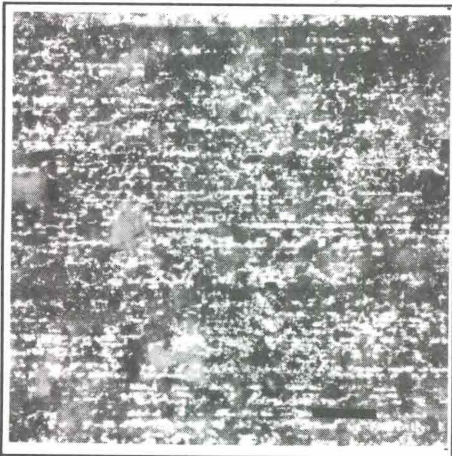


Figure 4.10 Machining grooves as a result of grinding the RBSN bolt. Bar = 0.1 mm.

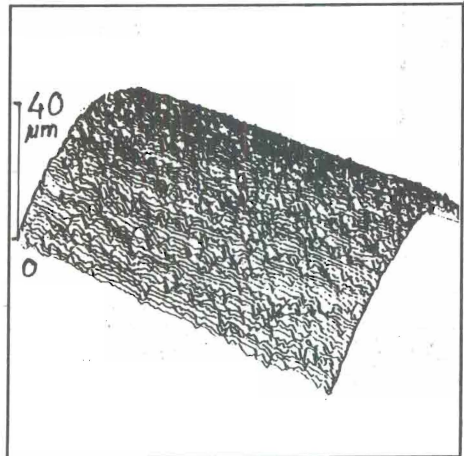


Figure 4.11 Three dimensional representation of the measured roughness. The figure covers an area of $1200 \times 600\ \mu\text{m}$.

4.6 Proof tensile tests

The first series of bolts (10 pieces) have been subjected to tensile tests. These tests had two objectives. The first objective was to set a maximum limit to the crack size in the bolt. The second objective was to measure the Young's modulus of our RBSN. As is stated in chapter 1 the tensile strength of RBSN is not a fixed value. This strength has a certain Weibull distribution. As is explained in section 3.6 this distribution in strength is due to a distribution in initial crack size. Bolts with a large crack in the reduced diameter will, at increasing the force, sooner reach the critical stress intensity factor. These bolts will then break. The remaining bolts will have cracks in the reduced diameter with a size smaller than $K_{Ic}^2/Y^2 \cdot \sigma_{max}^2$. The cracks are assumed to surface cracks. The value of σ_{max} was equal to 80 MPa. For the given material this will result in a maximum value of the crack of 780 μm . Due to a bending moment, which can be deduced from the signals of the two opposite strain measuring systems, some bolts broke just at the clamps. At a mean tensile stress of 80 MPa a bending stress of 30 MPa was measured at the centre of the bolt. To reduce this bending moment the standard clamps of the Lingstrom 400S tensile testing machine were replaced by a flexible clamping system which resulted in a decrease of the bending stress to 5 MPa (fig. 4.12, 4.13). The extension meter

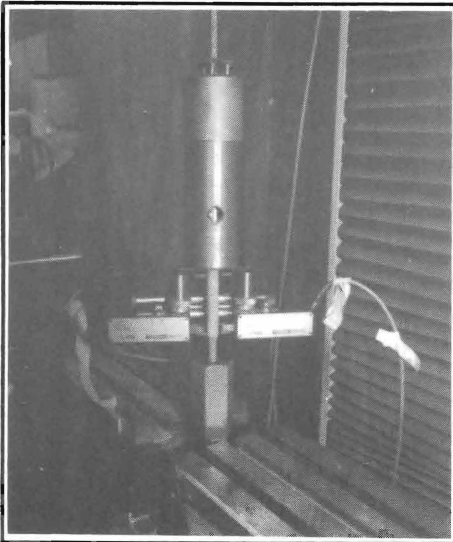


Figure 4.12 Experimental proof tensile set-up.

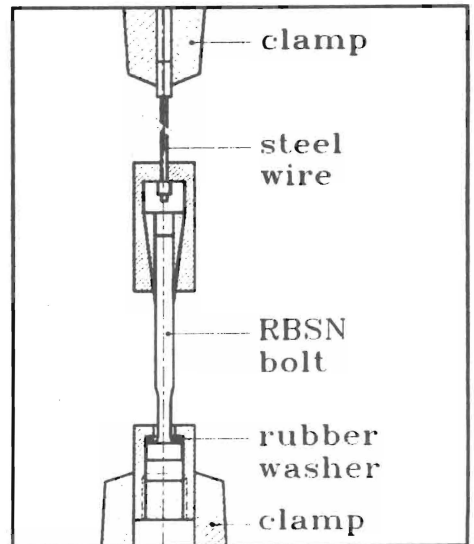


Figure 4.13 Schematic overview of bending free clamping system.

used was of mark Schenck Trebel type RDA2. Although the Youngs modulus of the RBSN has been given by the manufacturer this value has been verified According to A.M.E. the Youngs modulus should be 170 GPa. During the tensile tests both the elongation and the applied force were measured. Given the cross section area of the bolt, the stress and the Youngs modulus can be calculated. Figure 4.14 gives the force and strain signals from the tensile tests. The calculated mean Youngs modulus for ten bolts is equal to $E = 167 \text{ GPa} \pm 5 \text{ GPa}$. This is in good agreement with a value of 170 GPa given by the manufacturer and with a value of 172 GPa for RBSN with 20% porosity according to Phani and Niyogo [ref.4.1].

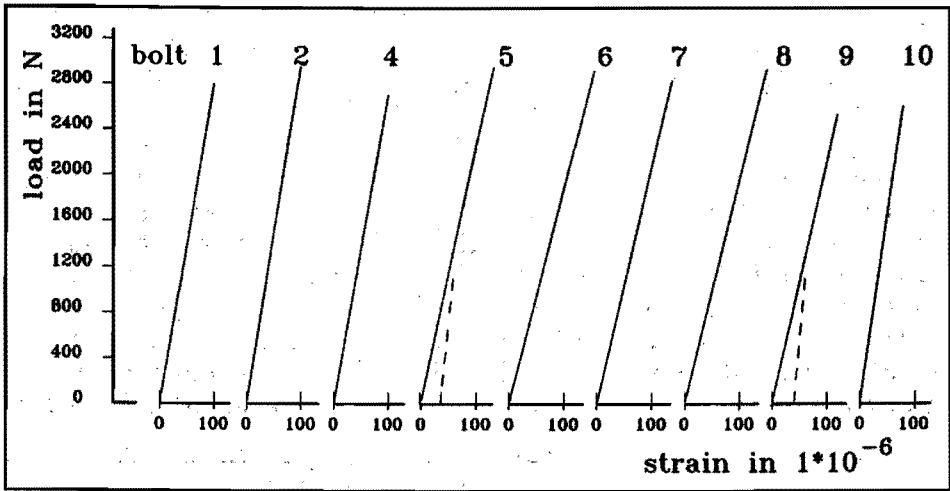


Figure 4.14 Force versus strain signals of nine RBSN bolts during the tensile tests (bolt 3 was already broken). The strain was measured with two opposite systems. From the signals of the separate systems the bending moment can be deduced.

4.7 Vickers indentation and saw slit

4.7.1 Vickers indentation

The mean purpose of the tensile tests was to set a maximum value for the crack size in the surviving bolts. The maximum possible size of the remaining cracks is thus known. But these cracks still have a certain distribution. To decrease the spread in lifetimes, to be measured during the tests, it is desirable to have, in all the bolts, cracks of one size. For

this reason in all the bolts cracks of one size, larger than the largest size of the cracks remaining after the tensile tests should be introduced. According to Steinmann and Bethge [ref. 4.2, 4.3] it is possible to introduce cracks of a given size by means of Vickers indentations. By the Vickers indentation a penny shaped crack should be created. For a value of $a/b = 0.45$ [ref. 4.3] the depth b of the crack can be determined by measuring the length $2a$ of the crack. For 23 HV50 indentations the lengths of the cracks, originating from the indentations, are measured. Figure 4.15 gives a Vickers indentation in RBSN. Figure 4.16 gives a crack originating from an indentation. The mean crack size (a) around these 23 indentations is equal to $154 \mu\text{m}$. The standard deviation equals $177 \mu\text{m}$. The shortest crack has a length of $0 \mu\text{m}$ and the largest crack has a length of $500 \mu\text{m}$. From these figures it can be concluded that the cracks, introduced by the Vickers indentation in the RBSN, have a length, which can not be reproduced within 10 %.

A deviation in crack length of 10 % can give rise to a change in lifetime by a factor ten (fig. 3.10). Although this method will produce sharp cracks, it is not used because the crack size is not reproducible. With a mean indentation width of $430 \mu\text{m}$, a crack length of $2 \times 154 \mu\text{m}$ and a depth width ratio of 0.45 this should result in a crack depth of $332 \mu\text{m}$. This is not larger than the largest crack remaining after the tensile tests.

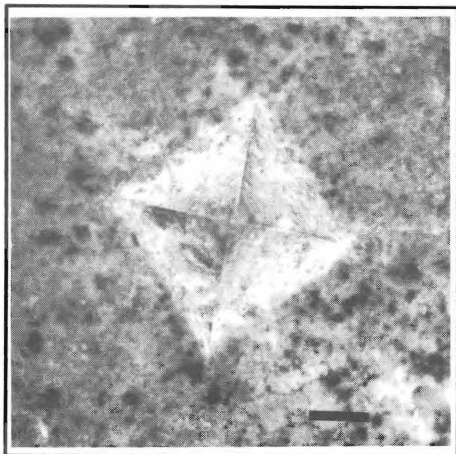


Figure 4.15 Vickers HV50 indentation in RBSN. From both horizontal edges cracks originate. Bar equals $100 \mu\text{m}$.

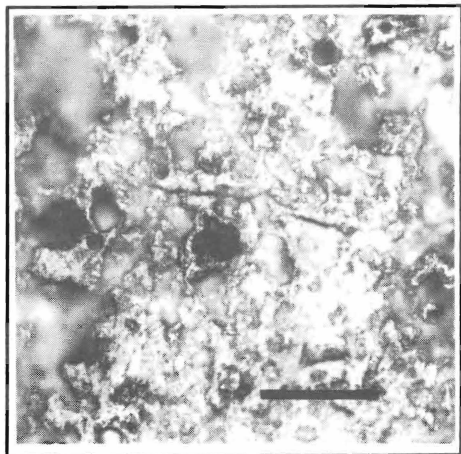


Figure 4.16 Crack clearly visible at the RBSN surface. Bar equals $50 \mu\text{m}$.

4.7.2 Saw slit

In our opinion it is necessary to make, in the bolt, a well defined crack at a well defined position. With such a crack the shape factor in the stress intensity factor can be calculated according to Paris [ref. 4.4]. For this calculation the circular cross section is translated to bar with a rectangular cross section. The rectangular cross section has a height equal to the diameter of the bolt. The width is adjusted to in such a way that the bending resistance moment of both bar and bolt are equal. Now it is possible to use Parish handbook. By means of the tensile proof test it is possible to exclude cracks larger than a given size. But neither the size nor the position or orientation of the remaining cracks are known. By means of the Vickers indentation method it is possible to make a crack at a well defined position. This crack size is not a reproducing function of the indentation force. Therefore it is not possible to create cracks with a fixed depth in this way. It is possible to make a notch at a well defined position with a well defined depth by means of a diamond saw. If the slit is small enough it has been assumed by Pabst to be a sharp crack [ref. 4.5]. In our case the slit was made with a diamond saw with a width of 0.2 mm. This resulted in a slit width of 0.28 mm (fig. 4.17). In figure 4.18 the critical stress intensity factor as a function of the saw slit radius according to Pabst is given.

The notch made by the saw has a width of 0.28 mm. As can be seen from figure 4.19 the saw slit intersects with a number of natural pores. These pores form sharp cracks. It is assumed that the effective width of the saw slit is equal to the width of those natural pores. In this way the saw slit has a sharp extension. The mean size of these pores is 20 μm . The depth of the slit ranges from 300 to 900 μm . In the calculation for the shape factor Y the length of a natural pore will be added to the notch depth. Despite the enlarging of the depth the bolts sometimes broke at large natural flaws (fig. 4.5). This could be an indication that the saw slit did not always intersect a sharp natural flaw.

According to Inglis [ref. 4.6] the stress concentration near a crack tip is inversely proportional to the root of the crack radius if the radius is small. To increase the effect of the saw slit its depth could be enlarged or its width could be decreased. It was decided to decrease the width of the saw slit. By means of a steel wire ($d = 40 \mu\text{m}$), covered with diamond paste ($d \leq 10 \mu\text{m}$), a small groove was made in the bottom

of the saw slit (fig. 4.20).

After this improvement of the saw slit configuration all bolts broke at the saw slitt. Our measurements are not in agreement with the saw width - K_{Ic} relation according to Pabst. The critical stress intensity factor is strongly dependent on the saw width.

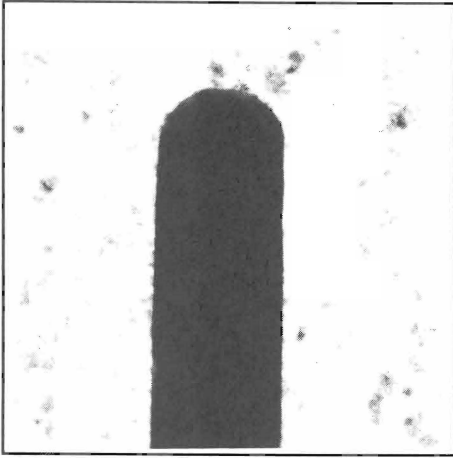


Figure 4.17 Cross section of the saw slit. Slit width is 0.28 mm.

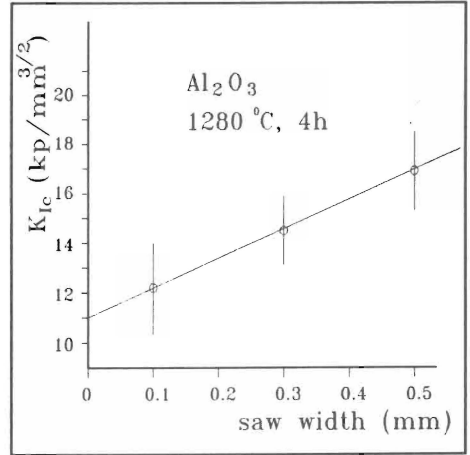


Figure 4.18 Relation between slit width and critical stress intensity factor according to Pabst.

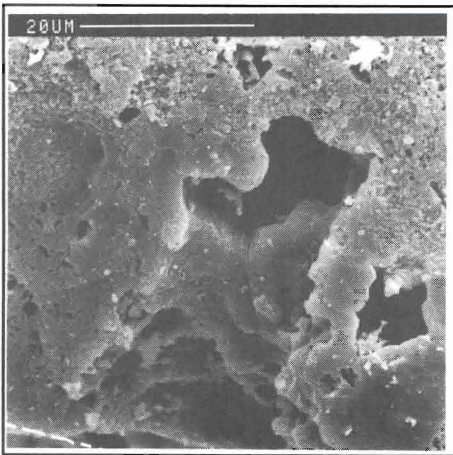


Figure 4.19 Crack surface originating from a natural flaw ($l = 300 \mu\text{m}$).

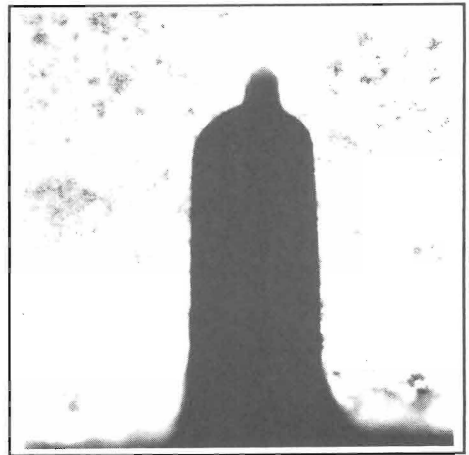


Figure 4.20 Cross section of saw slit (0,28 mm) with small groove made with steel wire.

4.8 Thermal and chemical attack of RBSN

4.8.1 Description of problem

The use of the RBSN at high temperatures during a long time, can result in a number of problems which have to be solved e.g.:

- the oxidation of RBSN in air
- the compatibility of RBSN with other ceramics
- the inhomogeneous distribution of sintering aids
- the phase transformations in the RBSN.

These problems will shortly be highlighted in the following subsections.

4.8.1.1 Oxidation of RBSN

After the first tests it turned out that the silicon nitride bolt head was covered with a layer of reaction products. The tests were performed in air at a temperature of 1773 K. The tests lasted approximately 10 hours. The layer at the front (hot) side of the bolt head had a thickness of 0.5 mm and was coloured brown. This is an indication that the layer contained iron-oxide next to silicon-oxide. In the layer large (0.5 mm) bubbles were enclosed. The bottom of the head, which was close to the alumina tile, had a white coloured layer. In these layers cracks were visible. Some of the cracks extended

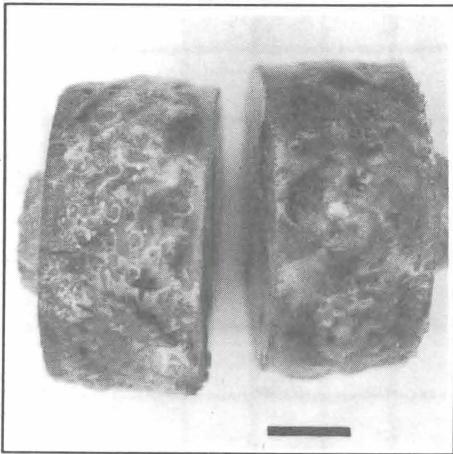


Figure 4.21 Impression of the reaction layer around the bolt head. Bar = 5 mm.

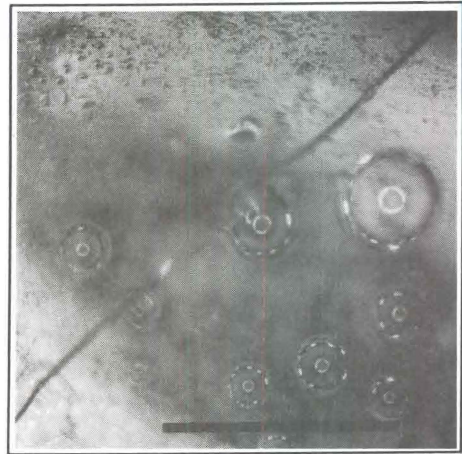


Figure 4.22 Agglomeration of bubbles in the reaction layer. Bar = 0.1 mm.

into the silicon nitride bulk material. These cracks might have been formed during cooling of the bolt. Figure 4.21 gives an overview of the layers around the bolt head. Figure 4.22 shows an agglomeration of cracks in the reaction layer.

To decrease the thickness of the reaction layer, the bolt was flushed with argon. The argon flush was set at a flow of 0.070 m³/h. This resulted in a decrease of layer thickness around the head from 0.5 to 0.2 mm. The thickness of the front layer remained the same. Although the thickness of the layer decreased, it was decided to stop flushing the bolts.

4.8.1.2 Compatibility tests

Four three point bend tests were performed to examine the compatibility of ceramic materials in air at a temperature of 1673 K during approximately 100 hours. The maximum stress in the RBSN bend bar was 2 MPa. The following combinations of ceramics were used:

- a - BN (low oxygen of Duramic) - RBSN (AME)
 - b - Al₂O₃ (Al23 of Friedrichsfeld) - RBSN (AME)
 - c - RBSN (Ceranox NR of Annawerk) - RBSN (AME)
 - d - Al₂O₃ (Al23 of Friedrichsfeld) - RBSN (Ekasin R of Elektro Schmelzwerke Kempten ESK).
- a - The test was performed with a RBSN bar on a BN support. After the test it turned out that the BN support evaporated (thickness loss = 0.5 mm). The RBSN bar was covered with a white glassy layer (fig. 4.23). Bubbles were visible in this layer. Cracks originating from this layer penetrated into the RBSN, causing the bar to break. The RBSN bar sintered to the BN support.
- b - After the test the RBSN bar was completely covered with a brown glassy layer (fig. 4.24). No cracks were visible in this layer nor on the bar itself. The transition area from RBSN to Al₂O₃ was covered with a transparent glassy layer. Also this bar sintered to its support.
- c - After this test it turned out that both the RBSN bar and RBSN support were covered with a brown glassy layer. No cracks were visible in the layers nor on the beam or support (fig. 4.25). Also in this set-up the bar sintered to its support.
- d - After the test the RBSN bar was covered with only a very thin transparent glassy layer (fig. 4.26). No cracks were visible in this layer. The RBSN did sinter to the Al₂O₃.

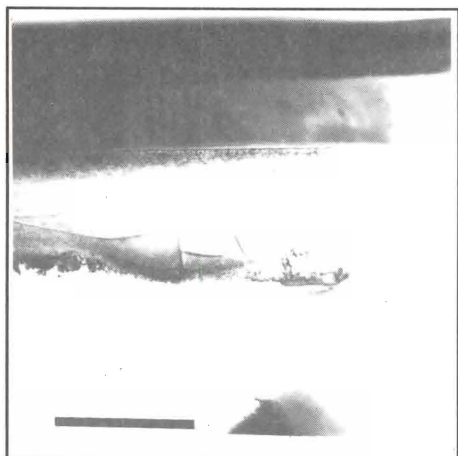


Figure 4.23 Layer on RBSN beam with cracks and bubbles. Bar = 5 mm.

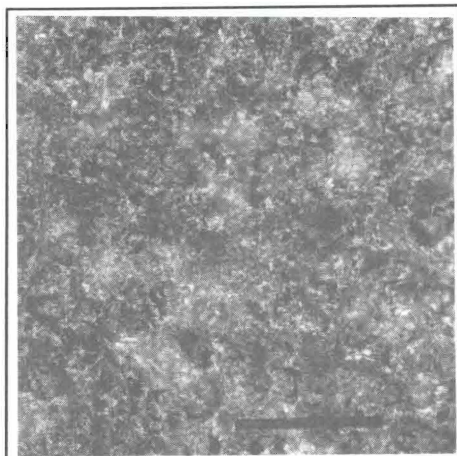


Figure 4.24 Layer on RBSN beam without any cracks. Bar = 0,5 mm.

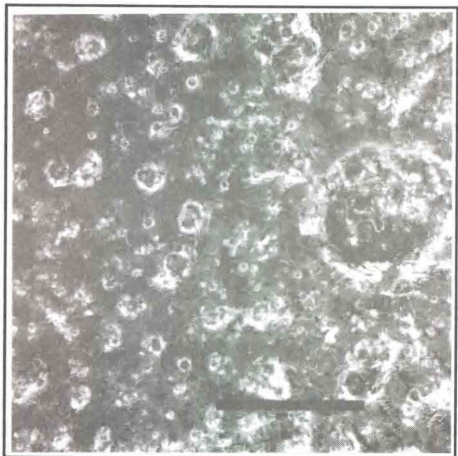


Figure 4.25 Layer on RBSN beam without any cracks. Bar = 0,5 mm.

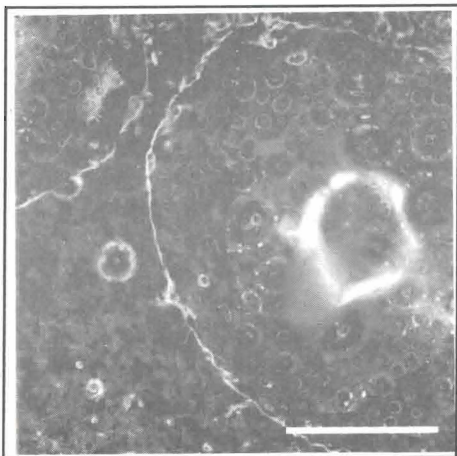


Figure 4.26 Transparent layer on E.S.K. RBSN beam. Bar = 0,5 mm.

From these experiments it was concluded that the different makes of RBSN will sinter together to Al_2O_3 . Both the RBSN of AME and Annawerk showed the typical covering with the brown (Fe_2O_3) layer. This layer was not visible on the RBSN of ESK.

4.8.1.3 Iron 'vulcano'

The sintering reaction of RBSN is increased by adding a small amount of metallic iron (< 1%) to the silicon before nitriding. In order to have an influence on the sintering speed the small iron particles should be equally dispersed in the green

silicon preshape. According to the observations the iron is not equally distributed over the RBSN. A normal cross section of an RBSN product is coloured grey (fig. 4.27). The cross section of the AME RBSN is coloured light grey. In this cross section dark grey areas are clearly visible (fig. 4.28).

By means of a semi quantitative Electron Micro Probe Analysis (EMPA) the composition of the ceramics is determined. This method only gives a relation between the elements selected to analyse. Elements with a molecular weight less than 16 can not be detected by the method used. To perform a correct quantitative measurement the surface to be analysed should be:

- electrically conductant
- perpendicular to the incident electron beam
- polished.

The RBSN surfaces analysed do not meet any of these requirements. As mentioned above the only information is a relative composition between selected elements (Si, Fe, Al, Ca and Mg). At four places over a radial section of the bolt head the composition has been determined. These places are:

- 1 - the centre of the bolt head
- 2 - a dark grey area
- 3 - a white coloured region near the surface
- 4 - the reaction layer on the surface.

In the centre of the bolt head there is a 1.2 % contribution of iron in the composition. In the dark grey area the contribution of iron is 10 %. The iron contribution in the white region below the surface is 0.55 %. In the reaction layer on the surface the iron content is 13 %.

From these measurements it is concluded that the iron is not equally dispersed in the RBSN. The amount of iron in the dark grey area is a factor ten higher than in the matrix. The iron content near the surface is low in contrary to the iron content in the reaction layer. It was concluded that the iron diffused to the surface. At the surface it reacted with oxygen to form a brown iron-oxide layer.

Some RBSN parts, which had no visible defect at the surface, before the test, showed some very explicit holes in the surface, after being exposed for approximately 100 h at 1773 K in air atmosphere. On the surface around these holes there is a thick brown reaction layer. In a cross section (fig. 4.29), through one of these holes, it looks as if a "vulcano" has erupted. A deep crater is visible at the surface. The "vulcano" cone, out of iron oxide, is formed on the surface of the RBSN ceramic (fig 4.30).

We assume that just below the RBSN surface there was a dark grey area with a high iron content. During the exposure at high temperature in air the iron oxidized. Iron-oxide has a larger volume than pure iron. Due to the increase in volume a pressure will develop in the dark grey area. If this pressure is high enough the RBSN bridge between surface and iron droplet will desintegrate. At 1773 K the iron-oxide is liquid. It will flow, through the created hole, to the surface of the RBSN. In this way a crack will be formed.

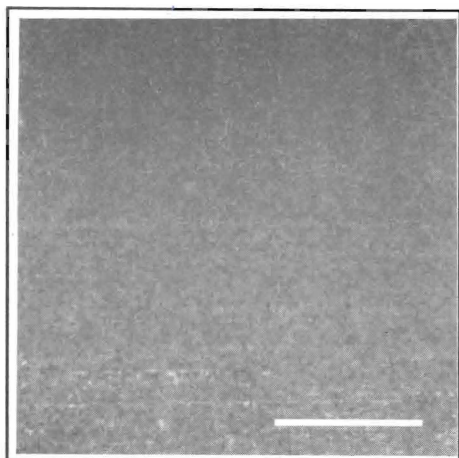


Figure 4.27 Cross section of RBSN from Annawerk. The cross section is equally coloured. Bar = 0,5 mm.

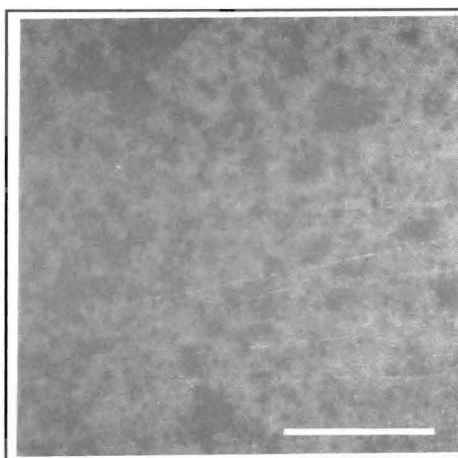


Figure 4.28 Cross section of RBSN from AME. Clearly visible are dark spots on this cross section. Bar = 0,5 mm.

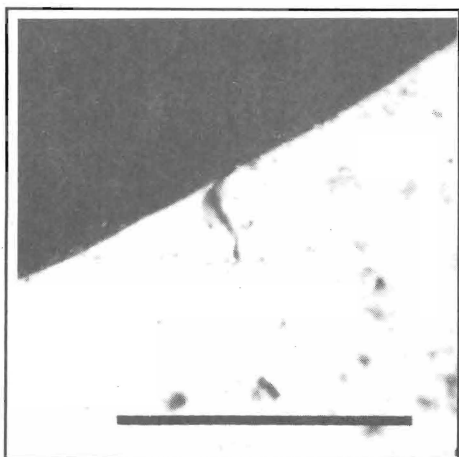


Figure 4.29 Cross section of iron vulcano with deep crater into the RBSN and with iron oxide 'vulcano' cone on the RBSN surface. Bar = 0.5 mm.

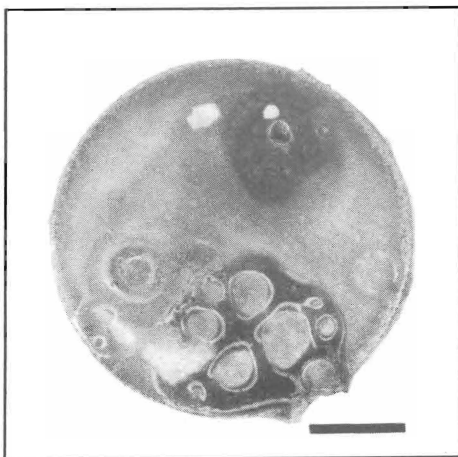


Figure 4.30 Top view on large iron vulcano. Bar = 5 mm.

From the measurements and from the observations it was concluded that RBSN used was of a poor quality. Because of the economics the manufacturer could not produce a homogeneous RBSN with a lower iron content.

4.8.1.4 Phase transformations

During the production of RBSN, the silicon preform reacts with nitrogen to form silicon nitride. In the first stage of this process, at a temperature of 1623 K, α - Si_3N_4 is formed. During the second stage of the process, at a temperature of 1723 K, the α - Si_3N_4 is transformed into β - Si_3N_4 . This second stage takes approximately 100 hours. During this stage 40 % of the Si_3N_4 is transformed. The strength of β - Si_3N_4 is some 25 % lower than the strength of α - Si_3N_4 [ref. 4.7]. During the first experiments the RBSN bolt head was kept at a temperature of 1773 K. The experiment lasted 100 hours. The experiment (in air with 80 % N_2) had the same influence on the transformation of Si_3N_4 as the last stage of the sintering process. As a result the Si_3N_4 was completely transformed from the α -phase to the β -phase. This will result in a lower allowable stress or a shorter lifetime at a certain stress.

The effect of the phase transformation on the composition of RBSN was measured by means of the X-ray diffraction method [ref. 4.8]. From one bolt the composition of the cold end and of the hot end (bolt head) was determined by this method. The results are given in figures 4.31 and 4.32. The inner two peaks of the quadruple peak around 35 degrees in fig. 4.31, indicate the appearance of α - Si_3N_4 . The two outer peaks correspond with β - Si_3N_4 . In figure 4.32 (hot bolt head) the two inner

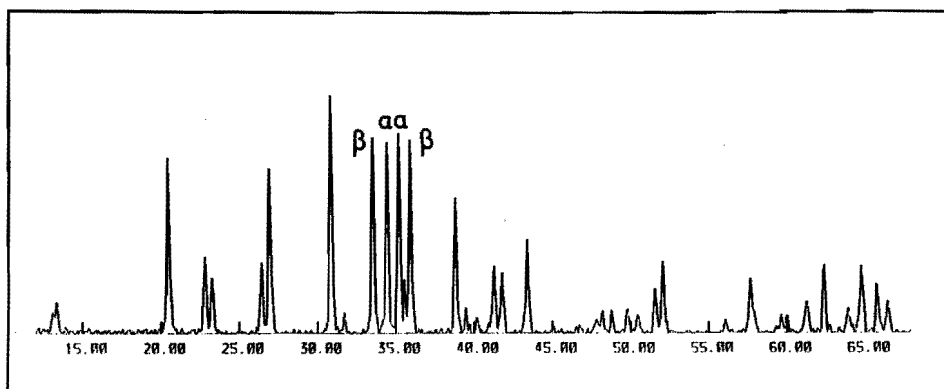


Figure 4.31 X-ray diffraction results from the cold part of the bolt. Horizontal axis is detection angle. The four peaks around 35° indicate both α - and β - phase.

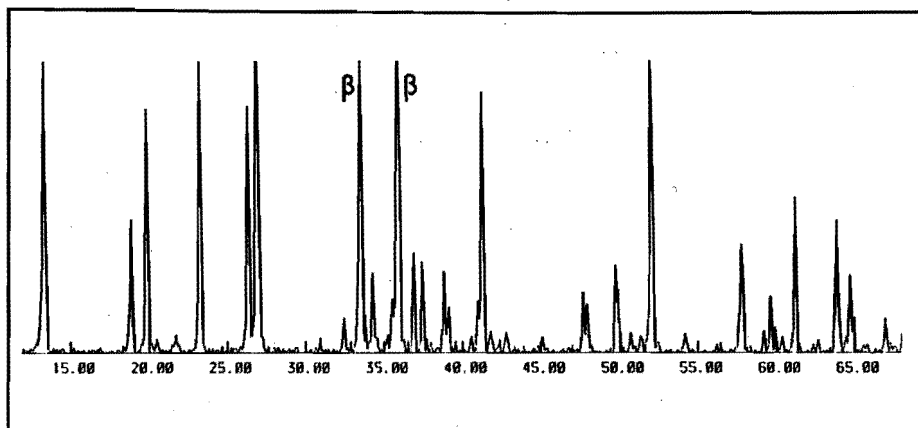


Figure 4.32 X-ray diffraction results from the hot bolt head. Horizontal axis is detection angle. The two peaks around 35° indicate only $\beta\text{-Si}_3\text{N}_4$.

peaks are not clearly visible. This indicates that the silicon nitride of the bolt head is transformed from $\alpha\text{-Si}_3\text{N}_4$ to $\beta\text{-Si}_3\text{N}_4$. The strength of the RBSN is decreased [ref. 4.7].

To prevent this transformation and to prevent corrosion, crack and sintering problems, the next series of experiments were performed at a lower temperature. The transformation process starts at a temperature above 1623 K [ref. 4.7]. To make sure that the RBSN will not transform, the temperature of the experiments was reduced to 1573 K.

4.9 Forces on the bolt

It is our intention to load the bolt with a known axial force. This will result in a certain stress distribution. The stress together with the saw slit will result in a stress intensity factor. Due to the crack growth the stress intensity factor will increase until it reaches the critical value. At that moment the bolt will break. In order to obtain only one centric tensile force a soft washer was placed beneath the bolt head to distribute the force over the circumference of the bolt head. The resulting force should then be in line with the centreline of the bolt. At the cold side a universal joint was placed between the bolt end and the steel back plate of the coupling beam. By means of the washer and the universal joint, only forces that coincide with the centreline of the bolt should be transmitted. Despite these systems also transverse forces could be transmitted by the bolt. They are introduced

by the following phenomena:

- a - contact between bolt and back plate at other places besides the bolt head and the universal joint
- b - non-equally distributed contact stress under the bolt head.

4.9.1 Thermal expansion

Before the heating up cycle of the experiment, the inner alumina plate and the outer steel back plate are in a aligned position (fig. 4.33 a). The bolts are loaded with only a small force (± 100 N). During the heating up cycle, the distance between the holes in the alumina tile will increase. The distance between the holes in the cold steel back plate does not increase (fig. 4.33 b). The bolt is still directed from the hole in the tile to the hole in the back plate. This direction is no longer perpendicular to the back plate. In the tile the bolt should rotate over the platinum washer. At the back plate the universal joint gives way to every wanted direction of the bolt. So during the heating up cycle no transverse force is introduced at the cold end of the bolt. A normal experiment

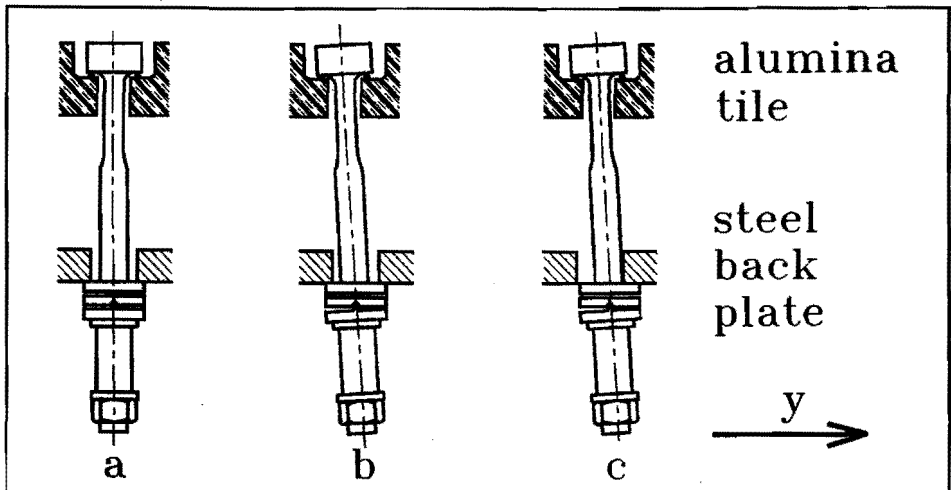


Figure 4.33 Position of bolt, alumina tile and steel back plate in the cold situation (a), during heat-up (b) and during cool down (c).

stops with the failure of the notched bolt, before the start of the cooling down cycle. Due to some failures in the power grid and in the control system of the oven, the oven cooled down twice before failure of the bolt. At that time the expe-

riments lasted over 50 hours. During cooling the distance between the holes in the tile decreased. A solidifying reaction layer between bolt head, platinum washer and alumina tile prevents the bolts from rotating there. To follow the still shrinking tile, the bolts have to move in y-direction (fig. 4.33 c) until they touch the hole edges. From that moment on an increasing transverse force acts on the cold end of the bolt. This results in a bending moment in the bolt which has a maximum at the bolt head. The bending stress can be significantly larger than the tensile stress. Since it is not transmitted by it, the transverse force can not be measured by strain measuring cylinder.

4.9.2 Bending moment tests

A small set-up (fig. 4.34) was built to verify the theory of the bending moment. In this set-up the bolt can be loaded with a certain force. This force is measured by the standard measuring cylinder. The eccentricity of force, at the bolt head, can be adjusted. Just below the bolt head two strain gauges are cemented to the bolt. They measure the bending stress in the bolt. A mirror is cemented on top of the bolt head. This mirror follows the rotation of the bolt head due to the eccentricity of the force. This rotation can be calculated from the measured displacement of the reflected laser beam on the mirror.

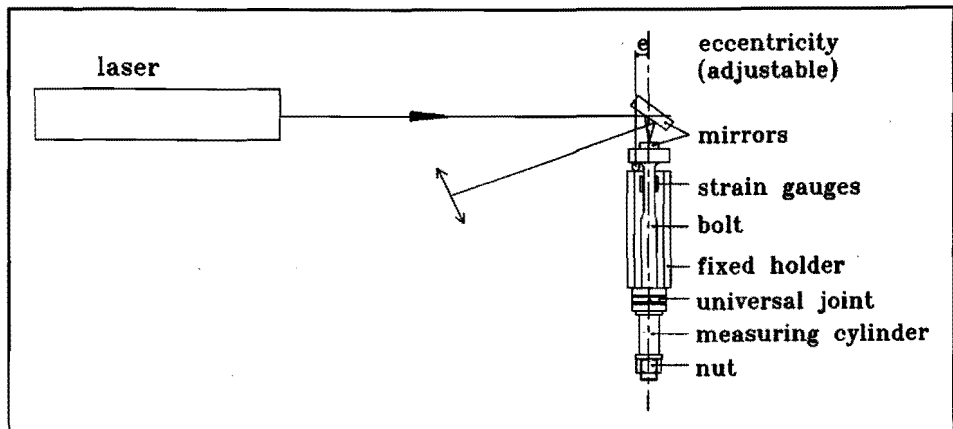


Figure 4.34 Experimental set-up to measure the bending moment and the transverse force without ball-and-cup and leaf spring systems.

A transverse force at the bolt end, due to an excentricity at the bolt head, will introduce a bending moment. Both the axial and transverse force are measured by the measuring cylinder. The bending moment results in a bending stress in the bolt shaft which is also measured. By means of the F.E.M. programm this stress is calculated. Also the rotation of the bolt head (c.q. mirror) is calculated.

Figure 4.35 gives the results of the first measurements with this set-up. On the vertical axis is the axial stress σ_a in the bolt shaft. The measured bending stress σ_b is on the horizontal axis. For a number of excentricities the measured relations between σ_a and σ_b are given by the continuous lines. The calculated relations are given by the dashed lines. The measured values lay on a straight line. This line does not intersect the origin. So there still is a small bending moment acting on the bolt at excentricity zero. This bending moment can be due to the fact that we load our bolt by means of a nut. This will be discussed in section 4.9.

From the above measurements we can derive the conclusion:

- If the axial force does not coincidence with the centre-line of the bolt than there is an excentricity in the loading. This excentricity will lead to a bending stress in the bolt shaft which is proportional to the axial force and to the excentricity.

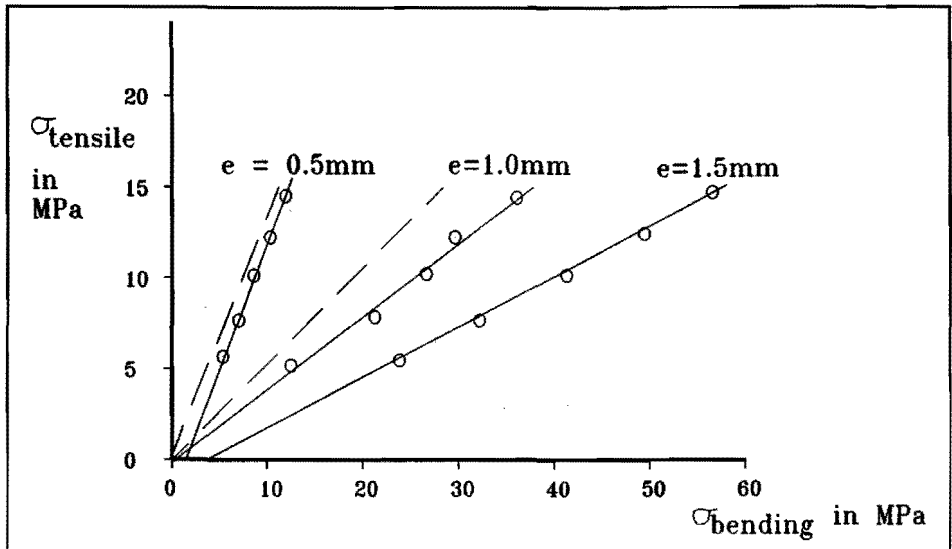


Figure 4.35 Relations between axial stress and bending stress for certain excentricities without ball-and-cup and leaf spring systems. Measured = continuous lines, calculated = dashed lines.

4.9.3 Screw-thread

The axial load on the bolt is applied by rotation of the nut over the screw thread of the bolt. Let us have a look in detail to the bolt-nut combination. Both parts are provided with screw thread. The thread of the bolt has a smaller diameter than the thread of the nut (fig. 4.36). In this way it is possible to move the nut over the bolt.

If the force is transmitted axially from the nut to the bolt (fig. 4.36 a) it is assumed that the load is transmitted by only one thread. Two equal forces act on the bolt at the same excentricity but at some axial difference. This results in a bending moment on the bolt.

If the effective force is transmitted off center, which can be the result of some particle below the nut or axial stroke of the nut, the nut will tilt over the bolt (fig. 4.36 b). It is assumed that the load is now transmitted by the two outer threads of the nut. The forces in this case are of different magnitude although they act at the same radial distance. Due to the larger axial distance between the two forces, the resulting bending moment on the bolt, is larger than in the former case.

If the component beneath the nut can move radially and if it

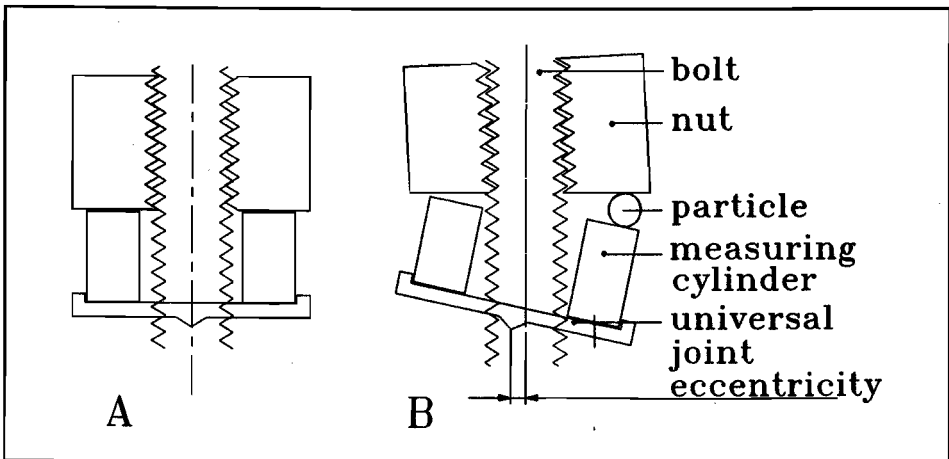


Figure 4.36 Nut over the screw-thread of a bolt. a: load centric transmitted. b: load transmitted off centre.

can rotate, it will do so in the latter case. This will result in an off axis transmission of the force from this component to the next component.

Rotating of the nut over the bolt can be diminished in two

ways. First we can reduce the tolerance between the screw-thread of the nut and screw-thread of the bolt. A second way is to increase the height of the nut. We used selected bolts and nuts with a very close tolerance on the threads.

4.9.4 Constructions to decrease the transverse force

Not only during premature cooling, but also during normal experiments the bolts broke just below the head. We suppose that this is also the result of a bending moment acting on the bolt shaft. If the platinum washer does not deform enough, then the force will not be equally distributed over the circumference of the bolt head. This results in a force at the bolt head at some distance (eccentricity) of the centreline (fig. 4.37).

At the cold side, the force will go through the centre of the universal joint. This centre coincides with the centreline of the bolt. The universal joint can transmit both axial and transverse forces. If in addition to the axial force there is also a transverse force transmitted by the joint then the signals of two opposite strain gauges will differ. The measured signals were always different. They sometimes differ more than 100 %. From this difference in strain gauge signals we deduced that the force at the bolt head had an excentricity up to 7.35 mm.

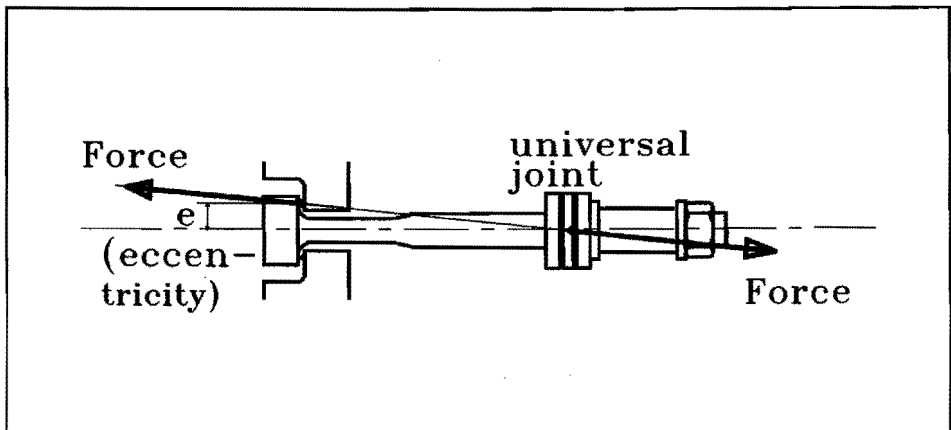


Figure 4.37 Excentricity of the force at the bolt head.

To reduce the transverse force, and with that the bending stress below the bolt head, there are some alternatives:

- a - use one bolt per tile
- b - use a kinematic suspension in the oven
- c - use a system with low transverse stiffness.

a - To prevent rotation of the tile two bolts are used in the test-rig.

b - If it is possible to make sure that the force, at the hot side, is acting through the centre line of the bolt, then there will be no transverse force in the bolt. In a beam-quadruple (fig. 4.38 a) the force from body 1 to body 3 will be transmitted through the momentary pole P_{13} of body 1 and body 3. This pole lies on the intersection point of the lines through body 2 and body 4. If this pole P_{13} lies on the centreline of the bolt then the resulting force will coincide with this centreline.

For one position of the bolt and tile this can be realised by a beam-quadruple. If the bolt translates or rotates with respect to the tile then the pole P_{13} will no longer coincide with the centreline of the bolt. If in one plane the beam-quadruple is replaced by two balls rolling over curves in the bolt head and the tile (fig. 4.38 b), a degree of freedom is introduced, which can be used to make sure that pole P_{13} will coincide with the centreline of the bolt.

In a starting position the lines through the contact points of the balls intersect in pole P_{13} on the centre

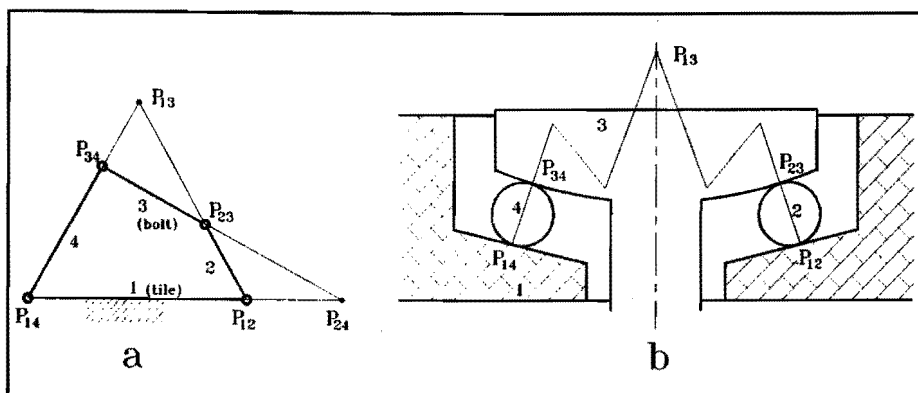


Figure 4.38 Basic principle of beam-quadruple (a) and possible realisation by means of balls (b).

line of the bolt. The bolt is rotated over a small angle. This results in rolling of the balls over a small distance. Given the condition of the pole to lie on the centreline of the bolt, will result in trajectories on both the bolt and the tile. For both movements (translation and rotation) of the bolt, with respect to the tile, the trajectories have been calculated to fulfil the condition of pole P_{13} to coincide with the centreline of the bolt.

For both movements it is not possible, in this way, to fulfil the condition of coincidence of pole and centreline. This possible solution was not used.

(In many tensile testing machines a ball bearing is used to decrease the bending moment in the testpiece. This bearing can give way to a rotation but not to a translation. If the clamps are not aligned, which normally is so, then a bending moment will still be introduced.)

- c - By means of low friction layers the friction coefficient can be reduced from 0.3 to 0.05, which, at a given axial force of 1000 N will result in a reduction of the transverse force from 300 to 50 N. By means of some ball-bearing gliding system, the transverse force can be reduced even further. Another way of reducing the transverse force is by means of a leaf spring system (fig. 4.39 b). In axial direction these systems have a high stiffness. In transverse direction the stiffness is significantly lower. To compensate for both horizontal and vertical movements, leaf springs in both directions are needed. The leaf springs can be replaced by wire springs. In that case only three wires are needed, which results in a more simple system (fig. 4.39 a). Both systems still have a transverse stiffness. If the springs are replaced by threads this stiffness would

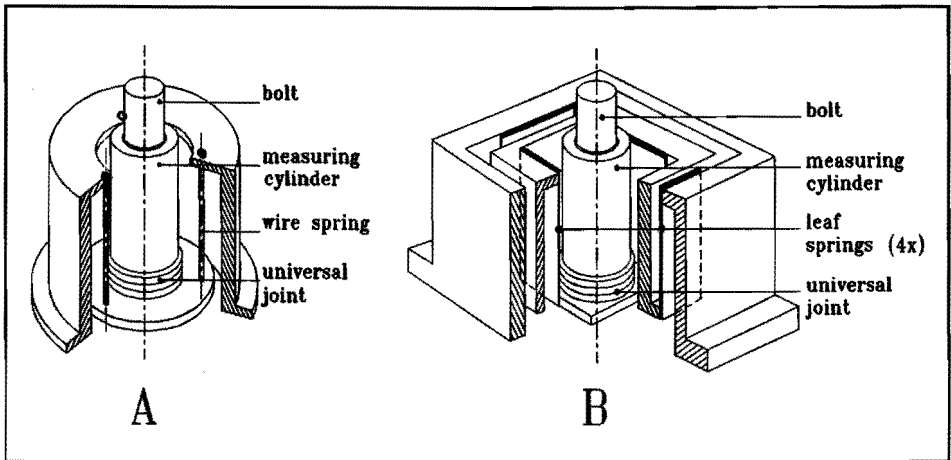


Figure 4.39 Two spring suspension systems with low transverse stiffness. System A by means of three wire springs. System B by means of four leaf springs.

become zero. For the designed system with the leaf-springs the transverse stiffness is equal to 2.5 N/mm. For the system with the wire springs the stiffness is equal to 13.8 N/mm due to the larger outer fibre distance.

The expected movement of the bolts is 0.5 mm. This would result in a transverse force of 1.25 N respective 6.9 N. From F.E.M. calculations it was deduced that the maximum tensile stress in the bolt would increase from 65 MPa (at zero transverse force) to 68 MPa or 88 MPa at transverse forces of 1.25 N respective 6.9 N. The tensile force is supposed to be equal to 1000 N. The increase in stress should be lower than 5 % so it was decided to build the more complicated system with the leaf springs.

The platinum washer reacts with the alumina tile. To prevent this reaction the washer was replaced with a ball-and-cup system. This system can follow the desired rotation of the bolt during heating up at low axial load. Once in position the load is always distributed equally over the circumference of the bolt. The load does not have to be equally distributed in respect of the tile. In a cold situation the friction coefficient between ball and cup was measured to be equal to 0.22.

The effect of the leaf spring system and the ball-and-cup system can be expressed in a decrease in bending stress at the saw slit in the bolt compared with this stress without any of these systems. This comparison is given in table 4.11. A transverse movement of the bolt end, due to thermal expansion, of 0.5 mm is assumed. In the case of the ball-and-cup system a tensile force of 1000 N is assumed. As the result of the comparison we can state that introducing some additional construction elements will significantly reduce the bending stresses.

Table 4.11 Comparison of the influence of several systems on the bending stress in the bolt.

system	tensile stress	bending stress	total stress
no system	65 MPa	309 MPa	374 MPa
ball-and-cup	65 MPa	38 MPa	103 MPa
leaf spring	65 MPa	3 MPa	68 MPa

References chapter 4

- 4.1 Phani, K.L., e.a., "Elastic modulus-porosity relationship in brittle solids", World congress on high tech ceramics, Milan, Italy 1986,
- 4.2 Steinmann, D., "Untersuchung des langsamen risswachstum von heisgepresstem siliziumnitrid bei hohen temperaturen", dissertation, Universität Karlsruhe, 1982.
- 4.3 Bethge, D., "Hochtemperaturkriechverformung und langsame rissausbreitung in keramische stoffen mit glasphase am beispiel HPSN", dissertation, Universität Karlsruhe, 1986.
- 4.4 Paris, e.a., "The stress analysis of cracks handbook", Paris Productions Inc., St. Louis, 1985.
- 4.5 Pabst, R.F., "Determination of K_{Ic} - factors with diamond-saw-cuts in ceramic materials", Fracture mechanics of ceramics, vol. 2, p. 555-565, Plenum Press, London, 1974.
- 4.6 Tetelman, A.S., e.a., "Fracture of structural materials", John Wiley & Sons, New York, U.S.A., 1977.
- 4.7 Davidge, R.W., "Mechanical properties of reaction bonded silicon nitride", ed. Riley, Nitrogen Ceramics, p. 541-559, Noordhoff, Leiden, 1977.
- 4.8 Walls, J.M., "Methods of surface analysis", Cambridge, Cambridge University Press, 1989.

5 CONCLUSIONS

From the present study the following conclusions concerning the design of a MHD generator wall segment, the diagnostics to measure the load on this segment, the models describing the dynamical and thermal behaviour of the wall segment, the models describing the slow crack growth in ceramics, the model to calculate the lifetime of the generator and the test-rig can be drawn.

Design of wall segment

For a closed cycle MHD generator a wall segment has been designed. A number of these segments have to be used to build a MHD generator wall. Because of the maximum size of the available ceramics, the wall of a large generator has to be segmented. Considering the electrical processes in the generator, ceramics should be used as inner materials. Considering the heat flux through the wall a thermal insulating material should be applied. In the design all these considerations are combined. During the present study it turned out that the bolt in the designed wall segment was loaded with both bending and tensile stresses (section 4.9). The designed wall segment (fig. 1.11), is a representation of our development. The systems (section 4.9), to exert a kinematical correct tensile stress without bending stress, were initially not incorporated in the design, but just added to it. The ball-and-cup system (section 4.9) can be incorporated in the design of the bolt and the tile. Because of the large number of bolts, attention has to be paid to the simplification and/or combination of the leaf spring system and the universal joint (section 4.9).

From a mechanical and electrical point of view the designed wall segment (section 1.8) is a good construction for a modular MHD generator channel. Ceramics do not show subcritical crack growth under pressure stresses. So it is better to avoid as much as possible tensile stresses in ceramic construction parts. If the cross section of the generator does not have to be rectangular then a shape closed construction with vaulted walls, where the tiles are loaded with a pressure stress, is a good construction. Further research should be performed to this topic.

For all the ceramic parts of a construction, especially those under tensile stress (bolts), stress concentrations should be

avoided.

For tensile testing systems the leaf spring system in combination with universal joints can be used to minimize the bending moment in the part subjected to the tensile stress.

Diagnostics

Two kinds of diagnostics, to measure the load on the bolt, were presented in chapter 2. These diagnostics are a laser-interferometer in combination with a dynamical model of the construction and a strain gauge measuring system.

At room temperature and with a constant load on the wall segment the laser-interferometer met its purpose. The accelerations measured, by the laser-interferometer and the forces in the bolts calculated with the model of these accelerations, are in good agreement with the values measured by other systems. At high temperature the duration of the laser-interferometer measurements was limited due to the oxidation and evaporation of the platinum laser mirror. At high temperature and with a thick platinum mirror, the duration of the laser-interferometer measurements was limited due to the shifting of the moving mirror while increasing the load.

The strain gauge system on the measuring cylinder performed well during all runs. In combination with the amplifier chosen even the strain signals with a frequency of 1000 Hz could be measured.

Models

In chapter 3 several models were presented which described certain aspects of the wall segment. These models have been concerned with the following items:

- dynamical modelling of the wall segment
- thermal modelling of the wall segment
- modelling of the crack growth
- probabilistic lifetime-calculation.

For a wall segment without leaf spring system and without air cylinder for load adjustment the presented dynamic model could well describe its dynamical behaviour. However the stiffness of some components had to be determined empirically.

The thermal model can be used to get a good idea (error <5%) of the temperature distribution in the wall segment. By an

empirical method the material data supplied by the manufacturer should be verified and adjusted before it can be used in the model.

The width of the saw slit has a strong influence on the failure stress of the bolts. All bolts with a radius of 0.03 mm broke at a lower stress than the bolts with a radius of 0.14 mm. The fatal crack was located at the saw slit.

The crack growth model presented can be applied to describe the crack growth in Reaction Bonded Silicon Nitride at 1573 K in air under slowly increasing stress. The constants in the relation for the crack growth velocity versus the stress intensity factor $v = AK_I^n$ using the data from the measurements under slowly increasing stress are for the material studied:

$$n = 18 \pm 6 \quad [-]$$
$$A = 1 \cdot 10^{-99 \pm 14} \quad [\text{si units}]$$

These are some of the few data on the subcritical crack growth in RBSN. The number of measurements, used to verify the model of subcritical crack growth under slowly increasing stress, is small. From these measurements we can only get an indication of the correctness of the crack growth model. Further investigations should be performed to decrease the spread.

The number of dynamic measurements, to verify the application of the subcritical crack growth model under dynamical loading, is too small to proof the correctness of this model. Because of the fact that the dynamical load was only 10% of the static load, the existence of an effective stress, to represent the dynamical load, could not be proved.

No experiments have been performed to prove the correctness of the probabilistic lifetime calculation (section 3.6) of MHD generators.

Test-rig

The experimental test-rig built to perform the lifetime tests was, in the end, a reliable device to load the wall segment with both a thermal and a mechanical load. After some modifications the slowly increasing stress system was a reproducible, transverse force free, system. Due to coupling of some weak devices in the load string of the bolt, the excitator was no longer strong enough to exert a dynamical load on the bolt that was 50% of the static load. Only a 10% share of the static load could be achieved. So there is no significant difference between the static and the dynamic loading.

Appendix A

Relevant properties of the used ceramics.

		Reaction Bonded Silicon Nitride A.M.E.	Aluminum Oxide E.S.K.	ZAL 45 I.C.I.
density	g/cc	2.5	3.8	0.72
porosity	%	20	0	70
composition		50% α -Si ₃ N ₄ 50% β -Si ₃ N ₄	99.7% Al ₂ O ₃ 0.2% MgO	96% Al ₂ O ₃ 3% SiO ₂
(bending) strength	300 K 1000 K MPa	150 150 150	340	-
compressive strength	300 K MPa	800	2500	4.5
Weibull modulus	m	10	25	-
Youngs modulus	300 K 1000 K GPa	170 163 156	310 300 270	10.5 8.0 7.0
Poissons ratio	-	0.23	0.27	-
hardness (Vickers)	MPa	3000	2100	-
thermal expansion	300 K 1000 K $\cdot 10^{-6} / K$	3.0 3.0 3.0	5.4 9.0 10.2	6.4 7.8 9.0
thermal conductivity	300 K 1000 K W/mK	12 7 6	28 9 6	0.12 0.24 0.35
specific heat	J/kgK	680	1025	1047
maximum temperature (melting, sublimation, decompose)	K	1670 2170	2120 2140	1920 2140
electrical resistance	300 K 1000 K Ω cm	10 ¹¹ 10 ⁸ 10 ⁵	10 ¹⁴ 10 ⁹ 10 ⁵	
magnetic permeability	μ_r	0.05	0.11	

Appendix B.

In this appendix a description is given of mathematical background of a Michelson-interferometer and of the expected signals on the detector of that meter. Also some information is given on the coherence of a laser beam.

The electric field E of a light beam at place z along its axis and at time t , can be described by formula b.1

$$E(z, t) = E_0 e^{i(-kz + \omega t + \phi)} \quad (\text{b.1})$$

$$E_0 = \text{electrical field at location } z = 0 \quad [\text{V/m}]$$

$$k = 2\pi/\lambda \quad \text{wave number} \quad [1/\text{m}]$$

$$\lambda = \text{wavelength} \quad [\text{m}]$$

$$\omega = \text{circular velocity} \quad [1/\text{s}]$$

$$t = \text{time} \quad [\text{s}]$$

$$z = \text{location along beam} \quad [\text{m}]$$

$$\phi = \text{phase angle} \quad [\text{rad.}]$$

For monochromatic and coherent light the phase angle ϕ is constant over the lightbeam. The detector measures the intensity of the light of the two reflected beams 1 and 2 according to formula b.2.

$$I_d = [E_1 e^{i(-kz + \omega t + \phi_1)} + E_2 e^{i(-kz + \omega t + \phi_2)}]^2 \quad (\text{b.2})$$

With the detector at a fixed place the real part of the intensity at a certain moment will be given by formula b.3.

$$I_d = E_1^2 + E_2^2 + 2E_1 E_2 \cos(\phi_1 - \phi_2) \quad (\text{b.3})$$

The phase difference $\delta = \phi_1 - \phi_2$ between the two lightbeams depends only on the difference in beam length $2s$. Where s is the displacement of the moving mirror. With good mirrors the energy of the two light beams will be almost equal ($E_1 = E_2$). The C is the background light intensity whereas the $B \cdot \cos(\delta)$

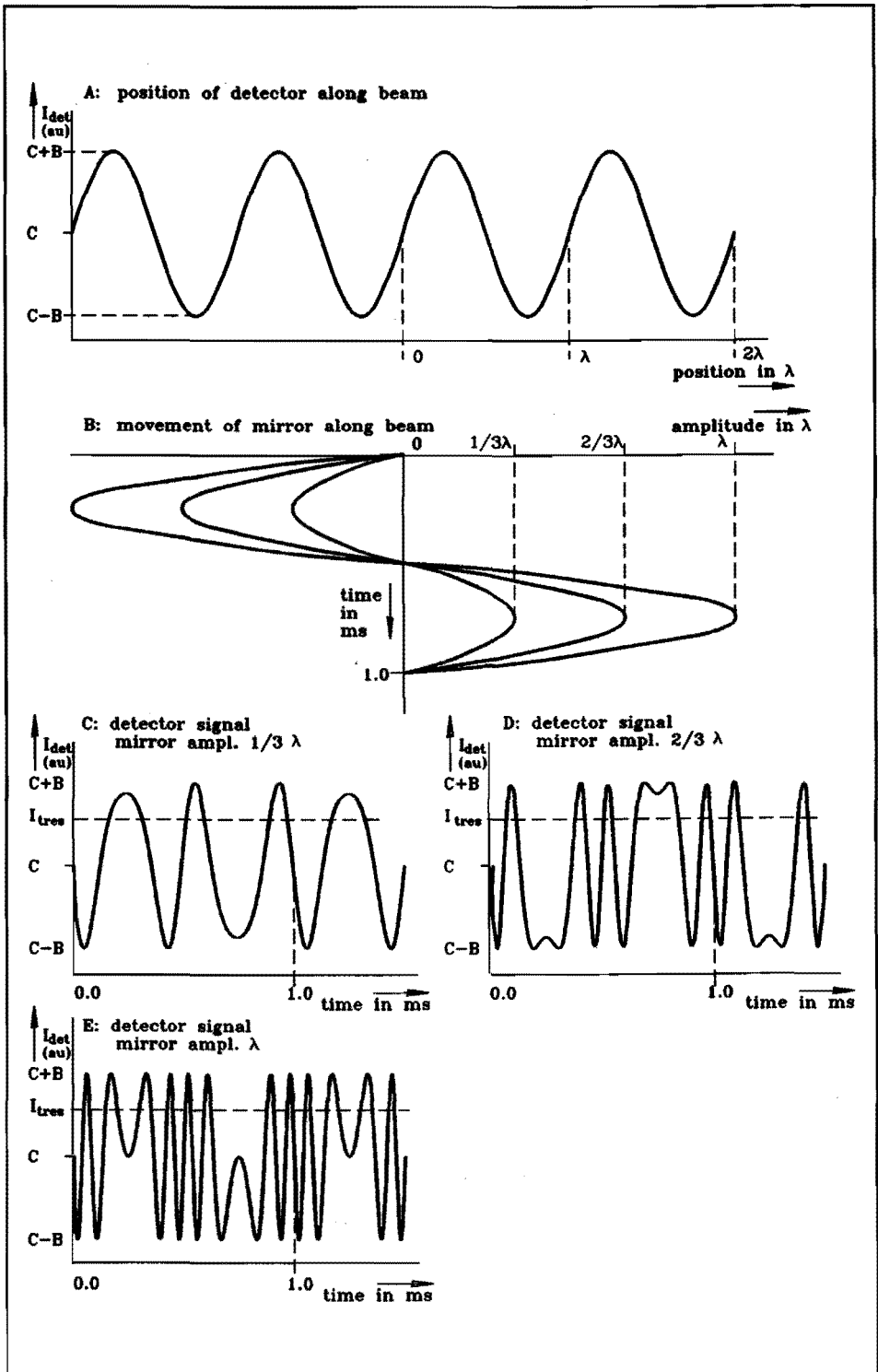


Figure b.1 Detector signals as function of amplitude of the displacements.

$$I_d = 2E_1^2(1 + \cos\delta) = C + B\cos\left(\frac{4\pi}{\lambda}s\right) \quad (\text{b.4})$$

is the, time or place dependent, fluctuating term often referred to as fringe. The detector will measure the fringes, with an intensity above a certain threshold value.

To see what we can expect to measure [ref b.1] let us look at figure b.1. In this figure we see at A the phase of the incident lightbeam on the moving mirror. At B we see the displacement of the moving mirror. Notice that at B a displacement of λ results in a displacement in A of 2λ , due to the double optical path. The signal on the detector, for the three different amplitudes of the movement, is given by C, D, and E respectively.

A maximum acceleration of 700 m/s^2 at a frequency of 1000 Hz results in a maximum amplitude of the displacement of $20 \cdot 10^{-6} \text{ m}$. For a HeNe-laser with a wavelength of $0.6328 \cdot 10^{-6} \text{ m}$ this displacement equals an optical displacement of 32 wavelengths, which results in 64 signals from the detector. Each period, the mirror moves over four times the amplitude of the sine. The 256 signals from the detector are not equally spaced in time. To measure this signal the sampling frequency of the counter should be at least 768 kHz.

The minimum detectable amplitude of the movement is $1/2 \lambda = 0.3164 \cdot 10^{-6} \text{ m}$. The minimum detectable acceleration at 1 kHz equals 12.5 m/s^2 .

Formula b.2 is based on the fact that the light is monochromatic and coherent. With a HeNe-laser the light is monochromatic. The light in the laser beam is only coherent over a certain length ΔL . Each laser has its own gain profile (Doppler profile) as is indicated in figure b.2. Due to some losses only frequencies within a short interval are amplified. This short interval is called the fluorescent linewidth Δf_1 . For the HeNe-laser with a wavelength of $0.6328 \cdot 10^{-6} \text{ m}$ ($f_0 = 4.74 \cdot 10^{14} \text{ Hz}$) the fluorescent linewidth is typical $1700 \cdot 10^6 \text{ Hz}$. Within this linewidth one or more wavelengths can be amplified. Each wave with a length of $\lambda = 2 \cdot l/n$ will be amplified in a laser tube with cavity length l . We call this a mode of a laser. In a laser, with a cavity length of 0.25 m, the mode spacing Δf_{ms} between two adjacent modes is given by formula b.5.

$$\Delta f_{ms} = \frac{c}{2l} = \frac{3 \cdot 10^8}{2 \cdot 0.25} = 600 \cdot 10^6 \text{ Hz} \quad (\text{b.5})$$

c - speed of light in vacuum

[m]

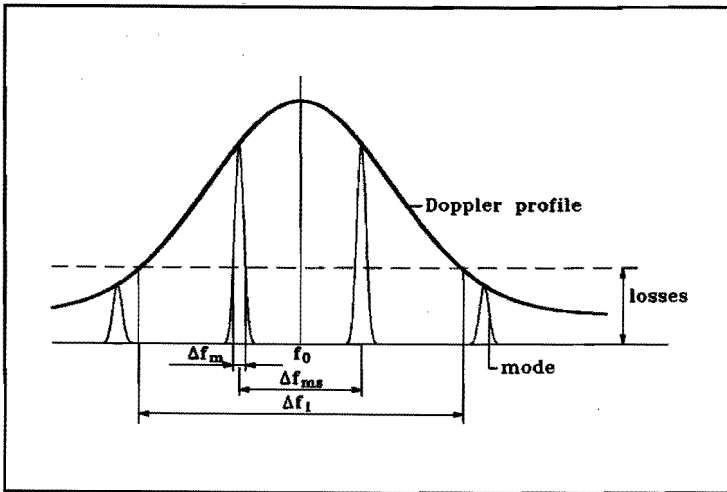


Figure b.2 Doppler profile and modes of a laser.

In a small laser the mode spacing is large. So there are only two modes in the fluorescent linewidth. These two modes are polarised perpendicular. Normally the linewidth of a laser beam equals the fluorescent linewidth of this laser. If there are only two modes beneath the fluorescent linewidth then the linewidth equals the mode spacing plus two times the mode width. If we filter one of the two modes then the linewidth equals the mode width. With the aim of a temperature and cavity length regulation you can achieve a linewidth $\Delta\nu$ of less than $10 \cdot 10^6$ Hz [b.1]. The coherence length of a laserbeam is given by formula b.6.

$$\Delta L = c \cdot \Delta t \quad (b.6)$$

$$\text{coherence time } \Delta t = \frac{1}{\Delta\nu} \quad (b.7)$$

$$b.7, b.8 \Rightarrow \Delta L = \frac{c}{\Delta\nu} \quad (b.8)$$

For the laser used the coherence length will become 30 m. If we did not filter one of the two modes the coherence length would be 0.17 m. In the experiment the optical path is approximately 1.5 m.

Appendix C.

For the strain gauge system, as described in paragraph 2.5, the force - voltage relation will be deduced in this appendix. We relate to the measuring shell of figure 2.6. Each shell has a cross-section of 26.5 mm². If we load the shell with 1000 N then the stress $\sigma = 37.7 \text{ N/mm}^2$. With this stress and a Youngs modulus E of $200 \cdot 10^3 \text{ N/mm}^2$ the strain ϵ in the shell will be 188.5 μ strain. The change in resistance of the strain gauge will be given by formula c.1.

$$\frac{\Delta R}{R} = K \frac{\Delta L}{L} = K\epsilon = K \frac{\sigma}{E} \quad (\text{c.1})$$

R - resistance [Ω]

K - gauge factor [-]

L - length [m]

With a strain gauge of 350 Ω and a gauge factor of 2 this will give a change of 0.132 Ω . We use the strain gauges in a half bridge figure c.1.

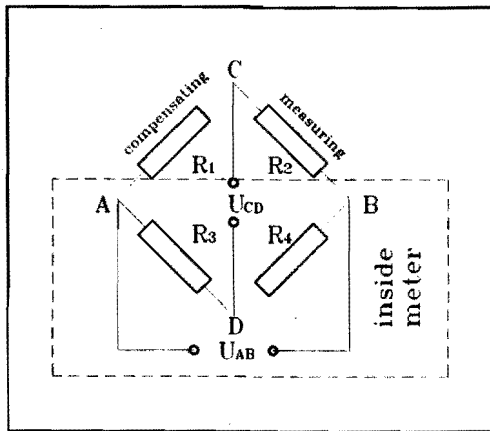


Figure c.1. Strain gauge circuit according to Wheatstone.

With the bridge in balance $R_{1 \cdot R4} = R_2 \cdot R_3$. Only the measuring strain gauge R_2 will change during loading.

$$U_{cd} = U \frac{\Delta R_2}{4R + 2\Delta R_2} \quad (c.2)$$

For a small change ΔR_2 this can be approximated by

$$U_{cd} = U \frac{\Delta R_2}{4R} = 0.25K\varepsilon \quad (c.3)$$

At an excitation voltage of 5 V and a gain of 1500 this should result in a measured bridge voltage of 0.707 V. The measured bridge voltage at a load of 1000 N was 0.710 V. This is good enough.

Appendix D.

In this appendix a general analytical solution will be given for the differential equations in paragraph 3.5 and 3.6. These equations describe the behaviour of the stress intensity factor, as function of the crack growth, under slowly increasing stress and under cyclic load. The stress intensity factor at the tip of a crack with length $2a$ is given by formula d.1. The general expression for the crack growth velocity is given by formula d.2.

$$K_I = Y\sigma(t)\sqrt{a(t)} \quad (d.1)$$

$$\frac{da}{dt} = v = AK_I^n \quad (d.2)$$

K_I stress intensity factor mode 1 [N/m^{3/2}]

Y shapefactor [-]

$\sigma(t)$ stress without crack at time t [Pa]

$a(t)$ crack length at time t [m]

v crack growth velocity [m/s]

A crack growth constant [-]

n crack growth exponent [-]

Differentiating d.1 with respect to t gives formula d.3.

$$\frac{dK_I}{dt} = Y \left(\sigma'(t)\sqrt{a(t)} + \sigma(t) \frac{1}{2\sqrt{a(t)}} \frac{da(t)}{dt} \right) \quad (d.3)$$

Substituting a from formula d.2 in d.3 will lead to formula d.4.

$$\frac{dK_I}{dt} = Y \left(\sigma'(t) \frac{K_I}{Y\sigma(t)} + \sigma(t) \frac{1}{2} \frac{Y\sigma(t)}{K_I} AK_I^n \right) \quad (d.4)$$

$$\begin{aligned}
 &= Y \left(\frac{\sigma'(t) K_I}{Y\sigma(t)} + \frac{Y}{2} \sigma^2(t) A K_I^{n-1} \right) \\
 &= \frac{K_I \sigma'(t)}{\sigma(t)} + \frac{AY^2}{2} \sigma^2(t) K_I^{n-1}
 \end{aligned}$$

$$\frac{dK_I}{dt} - \frac{\sigma'(t)}{\sigma(t)} K_I = \frac{AY^2}{2} \sigma^2(t) K_I^{n-1} \quad (d.5)$$

The general differential equation of Bernoulli is given by formula d.6.

$$y' + P(x)y = Q(x)y^p \quad (d.6)$$

We state that K is a function of z and α according to formula d.7.

$$K_I = z^\alpha \quad (d.7)$$

$$\frac{dK_I}{dt} = \alpha z^{\alpha-1} \frac{dz}{dt} \quad (d.8)$$

$$K_I^{n-1} = (z^\alpha)^{n-1} = z^{\alpha n - \alpha} \quad (d.9)$$

Formula d.5 combined with d.7 - d.9 gives formula d.10.

$$\alpha z^{\alpha-1} \frac{dz}{dt} - \frac{\sigma'(t)}{\sigma(t)} z^\alpha = \frac{AY^2}{2} \sigma^2(t) z^{\alpha n - \alpha} \quad (d.10)$$

$$\frac{dz}{dt} - \frac{\sigma'(t)}{\sigma(t)} \frac{z^\alpha}{\alpha z^{\alpha-1}} = \frac{AY^2}{2} \sigma^2(t) \frac{z^{\alpha n - \alpha}}{\alpha z^{\alpha-1}} \quad (d.11)$$

$$\frac{dz}{dt} - \frac{\sigma'(t)}{\sigma(t)} \frac{z}{\alpha} = \frac{AY^2}{2} \sigma^2(t) \frac{z^{\alpha n - 2\alpha + 1}}{\alpha} \quad (d.12)$$

This equation is linear if:

$$z^{\alpha n - 2\alpha + 1} = z^0 = 1 \quad (d.13)$$

$$\alpha n - 2\alpha + 1 = 0$$

$$\alpha = \frac{-1}{n-2} = \frac{1}{2-n} \quad (d.14)$$

Equation d.12 combined with d.14 leads to equation d.15.

$$\frac{dz}{dt} - \frac{\sigma'(t)}{\sigma(t)} (2-n) z = \frac{AY^2}{2} \sigma^2(t) (2-n) \quad (d.15)$$

Let us assume z to be a function of u and v; $z = uv$.

$$\frac{dz}{dt} = \frac{du}{dt} v + u \frac{dv}{dt} \quad (d.16)$$

Using these relations equation d.15 can be rewritten as equation d.17.

$$\frac{u dv}{dt} + \frac{v du}{dt} - \frac{\sigma'(t)}{\sigma(t)} (2-n) uv = \frac{AY^2}{2} \sigma^2(t) (2-n) \quad (d.17)$$

$$\left(\frac{dv}{dt} - \frac{\sigma'(t)}{\sigma(t)} (2-n) v \right) u + v \frac{du}{dt} = \frac{AY^2}{2} \sigma^2(t) (2-n) \quad (d.18)$$

Suppose the first coefficient of u in d.18 equals zero.

$$\frac{dv}{dt} - \frac{\sigma'(t)}{\sigma(t)} (2-n) v \quad (d.18)$$

$$\frac{dv}{v} - \frac{\sigma'(t)}{\sigma(t)} (2-n) dt = (2-n) \frac{\sigma'(t)}{\sigma(t)} = (2-n) \frac{d\sigma(t)}{\sigma(t)} \quad (d.20)$$

$$\int_{t=0}^t \frac{dv}{v} = (2-n) \int_{t=0}^t \frac{d\sigma(t)}{\sigma(t)} \quad (d.21)$$

$$\ln|v(t)| - \ln|v(0)| = (2-n)(\ln|\sigma(t)| - \ln|\sigma(0)|) \quad (d.22)$$

$$\ln \left| \frac{v(t)}{v(0)} \right| = (2-n) \ln \left| \frac{\sigma(t)}{\sigma(0)} \right| \quad (d.23)$$

$$\frac{v(t)}{v(0)} = \left(\frac{\sigma(t)}{\sigma(0)} \right)^{(2-n)} \quad (d.24)$$

$$(v > 0, \sigma > 0)$$

We assume no crack closure during the lifetime of the component. We are only considering tensile stresses. So the conditions of equations d.24 are fulfilled.

We stated that the first coefficient of u in equation d.18 equals zero. We will rewrite these equations using equation d.24.

$$v \frac{du}{dt} = \frac{AY^2}{2} \sigma^2(t) (2-n) \quad (\text{d.25})$$

$$v(t) \left(\frac{\sigma(t)}{\sigma(0)} \right)^{(2-n)} \frac{du}{dt} = \frac{AY^2}{2} \sigma^2(t) (2-n) \quad (\text{d.26})$$

$$\frac{du}{dt} = \frac{1}{v(t)} \frac{AY^2}{2} (2-n) \sigma^2(t) \left(\frac{\sigma(0)}{\sigma(t)} \right)^{(2-n)} \quad (\text{d.27})$$

$$\frac{du}{dt} = \frac{1}{v(t)} \frac{AY^2}{2} (2-n) \sigma^{(2-n)}(0) \sigma^n(t) \quad (\text{d.28})$$

$$\int_{t=0}^t du = \frac{1}{v(t)} \frac{AY^2}{2} (2-n) \sigma^{(2-n)}(0) \int_{t=0}^t \sigma^n(t) dt \quad (\text{d.29})$$

$$u(t) - u(0) = \frac{1}{v(t)} \frac{AY^2}{2} (2-n) \sigma^2(0) \int_{t=0}^t \sigma^n(t) dt \quad (\text{d.30})$$

$$u(t) = \frac{1}{v(t)} \frac{AY^2}{2} (2-n) \sigma^{(2-n)}(0) \int_{t=0}^t \sigma^n(t) dt + u(0) \quad (\text{d.31})$$

$$z = uv = \left(\frac{1}{v(t)} \frac{AY^2}{2} (2-n) \sigma^{(2-n)}(0) \int_{t=0}^t \sigma^n(t) dt + u(0) \right) \cdot \left(v(t) \left[\frac{\sigma(t)}{\sigma(0)} \right]^{(2-n)} \right) \quad (\text{d.32})$$

$$z = \frac{AY^2}{2} (2-n) \sigma^{(2-n)}(t) \int_{t=0}^t \sigma^n(t) dt + u(0) v(t) \left(\frac{\sigma(t)}{\sigma(0)} \right)^{(2-n)} \quad (\text{d.33})$$

$$K_I = z^{\frac{1}{2-n}} = K_I(t) = \left(\frac{AY^2}{2} (2-n) \sigma^{(2-n)}(t) \int_{t=0}^t \sigma^n(t) dt + u(0) v(t) \left[\frac{\sigma(t)}{\sigma(0)} \right]^{(2-n)} \right)^{\frac{1}{2-n}} \quad (\text{d.34})$$

$$K_I(t) = \left(\sigma^{(2-n)}(t) \left[\frac{AY^2}{2} (2-n) \int_{t=0}^t \sigma^n(t) dt + \frac{u(0) v(0)}{\sigma^{(2-n)}(0)} \right] \right)^{\frac{1}{2-n}} \quad (\text{d.35})$$

$$K_I(0) = \left(\sigma^{(2-n)}(0) \left[0 + \frac{u(0)v(0)}{\sigma^{(2-n)}(0)} \right] \right)^{\frac{1}{2-n}} \quad (d.36)$$

$$K_I(0) = (u(0)v(0))^{\frac{1}{2-n}} \quad (d.37)$$

$$u(0)v(0) = K_I^{(2-n)}(0) \quad (d.38)$$

$$\frac{u(0)v(0)}{\sigma^{(2-n)}} = \frac{K_I^{(2-n)}}{\sigma^{(2-n)}(0)} = \left(\frac{K_I(0)}{\sigma(0)} \right)^{(2-n)} = (Y\sqrt{a(0)})^{(2-n)} \quad (d.39)$$

The general expression of the stress intensity factor as function of time will be given by equation d.40.

$$K_I(t) = \left(\sigma^{(2-n)}(t) \left[\frac{AY^2}{2} (2-n) \int_{t=0}^t \sigma^n(t) dt + (Y\sqrt{a(0)})^{(2-n)} \right] \right)^{\frac{1}{2-n}} \quad (d.40)$$

From this equation a general expression of the crack length as function of time can be deduced.

$$K_I(t) = Y\sigma(t)\sqrt{a(t)} \Rightarrow a(t) = \frac{K_I^2(t)}{Y^2\sigma^2(t)} \quad (d.41)$$

$$a(t) = \frac{\left(\sigma^{(2-n)}(t) \left[\frac{AY^2}{2} (2-n) \int_{t=0}^t \sigma^n(t) dt + (Y\sqrt{a(0)})^{(2-n)} \right] \right)^{\frac{1}{2-n}}}{Y^2\sigma^2(t)} \quad (d.42)$$

$$a(t) = \frac{\left(\sigma^{(2-n)}(t) \left[\frac{AY^2}{2} (2-n) \int_{t=0}^t \sigma^n(t) dt + (Y\sqrt{a(0)})^{(2-n)} \right] \right)^{\frac{2}{2-n}}}{(Y^{(2-n)}\sigma^{(2-n)}(t))^{\frac{2}{2-n}}} \quad (d.43)$$

This general expression of the crack length as function of time is given by equation d.44.

$$a(t) = \left(\frac{AY^n}{2} \int_{t=0}^t \sigma^n(t) dt + a^{\left(\frac{2-n}{2}\right)}(0) \right)^{\frac{2}{2-n}} \quad (d.44)$$

For the two special cases of a slowly increasing stress and of a cyclic stress, the expressions of the stress intensity factor and of the crack length, as function of time, will be given.

Slowly increasing stress.

$$\sigma(t) = \dot{\sigma} t \quad (\dot{\sigma} \text{ is constant}) \quad (d.45)$$

$$\sigma^{(2-n)}(t) = (\dot{\sigma} t)^{(2-n)} = \dot{\sigma}^{(2-n)} t^{(2-n)} \quad (d.46)$$

$$\int_{t=0}^t \sigma^n(t) dt = \int_{t=0}^t \dot{\sigma}^n t^n dt = \dot{\sigma}^n \int_{t=0}^t t^n dt = \dot{\sigma}^n \left[\frac{t^{(n+1)}}{n+1} \right]_{t=0}^t \quad (d.47)$$

$$= \dot{\sigma}^n \left(\frac{t^{(n+1)}}{n+1} - 0 \right) = \frac{\dot{\sigma}^n}{n+1} t^{(n+1)} \quad (d.48)$$

$$\frac{\dot{\sigma}^n t^n t}{n+1} = \frac{(\dot{\sigma} t)^n t}{n+1} = \frac{\sigma^n(t) t}{n+1} \quad (d.49)$$

The stress intensity factor as function of time will be.

$$K_I(t) = \left(\dot{\sigma}^{(2-n)} t^{(2-n)} \left[\frac{AY^2}{2} (2-n) \frac{\sigma^n(t) t}{n+1} + (Y\sqrt{a(0)})^{(2-n)} \right] \right)^{\frac{1}{2-n}} \quad (d.50)$$

$$K_I(t) = \left(\sigma^{(2-n)}(t) \left[\frac{AY^2}{2} (2-n) \frac{\sigma^n(t) t}{n+1} + (Y\sqrt{a(0)})^{(2-n)} \right] \right)^{\frac{1}{2-n}} \quad (d.51)$$

And $a(t)$ will be equal to;

$$a(t) = \left(\frac{AY^n}{2} (2-n) \frac{\sigma^n(t) t}{n+1} + a(0) \right)^{\frac{2-n}{2-n}} \quad (d.52)$$

Cyclic stress with prestress.

$$\sigma(t) = \sigma_0 + \sigma_{amp} \sin(\omega t) \quad (d.53)$$

$$K_I(t) = \left(\left| Q \left[\frac{AY^2}{2} (2-n) R + S \right] \right| \right)^{\frac{1}{2-n}} \quad (d.54)$$

with

$$Q = (\sigma_0 + \sigma_{amp} \sin(\omega t))^{(2-n)}$$

$$R = \sigma_0^n \sum_{k=0}^n \binom{n}{k} \left(\frac{\sigma_{amp}}{\sigma_0} \right)^k \int_{t=0}^t \sin^k(\omega t) dt$$

$$S = (Y\sqrt{a(0)})^{(2-n)}$$

$$\sigma_0^n \sum_{k=0}^n \binom{n}{k} \left(\frac{\sigma_{amp}}{\sigma_0} \right)^k \int_{t_0}^t \sin^k(\omega t) dt - \int_{t_0}^t (\sigma_0 + \sigma_{amp} \sin(\omega t))^n dt \quad (d.55)$$

and a(t) will be equal to;

$$a(t) = \left(\frac{AY^n}{2} (2-n) \sigma_0^n \sum_{k=0}^n \binom{n}{k} \left(\frac{\sigma_{amp}}{\sigma_0} \right)^k \int_{t_0}^t \sin^k(\omega t) dt \right) + a(0) \left(\frac{(2-n)}{2} \right)^{\frac{2}{2-n}} \quad (d.56)$$

Appendix E.

The lifetime of a M.H.D. generator is calculated in paragraph 3.6.4. The influence of the variation of some initial conditions on the lifetime of the generator is presented in figures 3.21 - 3.25. The variation of the initial conditions are:

- the initial load on the bolts.
- the Weibull modulus of the RBSN.
- the proofload.
- the load on the outer bolts.
- the number of bolts on one wall.

The results of these calculations are presented in this appendix in tabular form. The first two numbers in the next tables are the characteristic failure time of the first bolt and the Weibull modulus of that distribution. The next two numbers are the characteristic lifetime of the whole wall and the Weibull modulus of that distribution.

Table E.1 Variation of the initial load on the bolts.

	50 MPa	55 MPa	60 MPa	65 MPa	70MPa
no bond	16.8e6	5.89e6	2.25e6	0.93e6	0.41e6
	m= 1.5	m= 1.5	m= 1.5	m= 1.5	m= 1.5
	27.7e6	9.68e6	3.71e6	1.53e6	0.66e6
	m= 2.7	m= 2.7	m= 2.7	m= 2.7	m= 2.6
stret- ching bond	25.6e6	8.96e6	3.43e6	1.42e6	0.62e6
	m= 1.6	m= 1.6	m= 1.6	m= 1.6	m= 1.5
	37.5e6	13.1e6	5.02e6	2.06e6	0.91e6
	m= 2.5	m= 2.5	m= 2.5	m= 2.5	m= 2.4
hexago- nal bond	16.0e6	5.60e6	2.14e6	0.88e6	0.39e6
	m= 1.5	m= 1.5	m= 1.5	m= 1.5	m=1.5
	33.0e6	11.5e6	4.39e6	1.82e6	0.80e6
	m= 3.2	m= 3.1	m= 3.1	m=3.1	m= 3.1

Table E.2 Variation of the Weibull modulus.

	m = 5	m = 10	m = 15	m = 20	m = 25
no bond	0.01e6	0.45e6	2.26e6	4.96e6	7.85e6
	m= 0.7	m= 1.0	m= 1.5	m= 2.1	m= 2.6
	0.07e6	1.35e6	3.71e6	6.60e6	9.54e6
	m= 0.9	m= 2.0	m= 2.7	m= 3.4	m= 3.9
stret- ching bond	0.00e6	0.90e6	3.44e6	6.71e6	10.0e6
	m= 0.5	m= 1.0	m= 1.6	m= 2.14	m= 2.7
	0.15e6	1.94e6	5.02e6	8.53e6	11.8e6
	m= 0.8	m= 1.8	m= 2.5	m= 3.1	m= 3.7
hexago- nal bond	0.00e6	0.44e6	2.14e6	4.73e6	7.53e6
	m= 0.7	m= 1.0	m= 1.5	m= 2.1	m= 2.6
	0.08e6	1.63e6	4.39e6	7.50e6	10.5e6
	m= 0.9	m= 2.2	m= 3.1	m= 3.9	m= 4.5

Table E.3 Variation of the proofload.

	70 MPa	90 MPa	110 MPa	120 MPa	140 MPa
no bond	2.25e6	2.45e6	4.14e6	7.23e6	26.7e6
	m= 1.5	m= 1.8	m= 3.5	m= 5.7	m= 40.2
	3.71e6	3.86e6	5.41e6	8.35e6	27.2e6
	m= 2.7	m= 3.1	m= 6.2	m= 8.6	m= 51.9
stret- ching bond	3.43e6	3.49e6	4.97e6	7.84e6	26.9e6
	m= 1.6	m= 1.8	m= 2.9	m= 4.4	m= 19.7
	5.02e6	5.15e6	5.97e6	8.84e6	27.4e6
	m= 2.5	m= 2.7	m= 5.7	m= 10.2	m= 48
hexago- nal bond	2.14e6	2.31e6	3.47e6	7.18e6	26.7e6
	m= 1.5	m= 1.8	m= 3.8	m= 7.3	m= 39.0
	4.39e6	4.57e6	5.13e6	7.95e6	26.5e6
	m= 3.1	m= 3.6	m= 6.0	m= 8.3	m= 48

Table E.4 Variation of the load on the outer bolts.

	0,6	0,7	0,8	0,9	1,0
no bond	3.36e6	3.36e6	3.36e6	3.36e6	3.36e6
	m= 1.5	m= 1.5	m= 1.5	m= 1.5	m= 1.5
	5.29e6	5.29e6	5.29e6	5.29e6	5.29e6
	m= 2.8	m= 2.8	m= 2.8	m= 2.8	m= 2.8
stret- ching bond	4.83e6	4.83e6	4.83e6	4.83e6	4.83e6
	m= 1.5	m= 1.5	m= 1.5	m= 1.5	m= 1.5
	7.27e6	7.27e6	7.27e6	7.27e6	7.27e6
	m= 2.5	m= 2.5	m= 2.5	m= 2.5	m= 2.5
hexago- nal bond	2.57e6	2.57e6	2.57e6	2.57e6	2.57e6
	m= 1.5	m= 1.5	m= 1.5	m= 1.5	m= 1.5
	5.04e6	5.04e6	5.04e6	5.04e6	5.04e6
	m= 3.0	m= 3.0	m= 3.0	m= 3.0	m= 3.0

Table E.5 Variation of the number of bolts (tiles).

	20 x 3 27 x 3 19 x 7	25 x 4 31 x 5 25 x 9	30 x 5 35 x 7 31 x 11	35 x 6 39 x 11 37 x 13	40 x 7 43 x 13 43 x 15
no bond	3.99e6	2.96e6	3.99e6	1.89e6	1.57e6
	m = 1.5	m = 1.5	m = 1.5	m = 1.5	m = 1.5
	5.24e6	4.34e6	5.24e6	3.31e6	2.97e6
	m = 2.4	m = 2.6	m = 2.4	m = 2.9	m = 2.9
stret- ching bond	5.23e6	3.44e6	2.65e6	1.92e6	1.59e6
	m = 1.6	m = 1.6	m = 1.5	m = 1.5	m = 1.5
	6.56e6	5.02e6	4.31e6	3.44e6	3.22e6
	m = 2.2	m = 2.5	m = 2.4	m = 2.8	m = 2.9
hexago- nal bond	3.78e6	2.74e6	2.14e6	1.76e6	1.45e6
	m = 1.5	m = 1.5	m = 1.5	m = 1.5	m = 1.5
	6.27e6	5.09e6	4.39e6	3.96e6	3.53e6
	m = 2.7	m = 3.1	m = 3.1	m = 3.2	m = 3.4

Appendix F

In this appendix a comprehensive description of the several lifetime measurements (runs) and covering experiments will be given.

The first run was scheduled to get familiar with the set-up. The oven should be brought to 1773 K and the excitator should be tested together with a real testpiece. During heating up one bolt broke at a temperature of 673 K and at a stress of 9.7 MPa. The fatal crack originated from the saw cut. The oven was cooled down and the bolts were replaced.

The second run had the same aim as the first run. The preload was 9.7 MPa. During the heating a smell of burned epoxy was noticed and the experiment was stopped. The temperature inside the oven reached 1679 K. According to the schedule the oven was cooled down.

The third run had still the same aim as the first run. The set-up was improved with an air cooling system for the circumference of the glassfibre reinforced epoxy cooling plate. During heating of the oven it was noticed that most of the introduced cooling air passed along the testpiece to the inner chamber of the oven. It left the oven at high temperature by the diagnostic holes. This air heated the optical part the set-up. Again the experiment was stopped, at a temperature of 1208 K.

The fourth run had the same aim as the first run. The temperature of 1773 K was reached without any problem. The system was held at this temperature for one hour. Without having used the excitator the run was stopped by cooling down the system at the end of the week.

In the fifth run the aim of the first run was reached. The oven was heated till 1773 K. This temperature was held constant for one hour. After that time the excitator was switched on. At a frequency of 1000 Hz the amplitude of the excitator was set in such a way that the dynamic force on the bolt was half the static force. The dynamic stress was set to 5 MPa. This testpiece was loaded in this way during half an hour. Since all parts of the set-up worked well at this time the oven was cooled down. During cooling of the oven both bolts broke. One bolt broke at a temperature of 743 K at a stress of

4 MPa after 60,000 s. The fatal crack in this bolt was located near the bolt head. The second bolt broke at room temperature at a stress of 4 MPa after 75,000 s. This bolt broke also near the bolt head.

After dismounting of the bolts it turned out that the bolt heads were covered with a brown layer. This layer showed some remarkable pits. The bolt shaft was covered with a white layer containing a large number of bubbles.

To investigate the brown and white layer some experiments were performed. During the first of these experiments a small RBSN bar was placed in the oven in contact with three alumina bars. After 4 hours at 1673 K the RBSN bar was also covered with a brown layer. Near the alumina bars the layer was white and contained bubbles. Although no load was exercised on the RBSN bar a small crack could be seen in the bar. This crack was located in the part of the bar which was covered with the white layer. More cracks were visible in this white layer. But no more cracks penetrated into the RBSN bar.

From this test it was concluded that the white layer on the RBSN was formed by a reaction with the alumina. The thermal expansion of this surface layer is smaller than that of the RBSN. Due to this fact the surface layer cracked during cooling. At a certain point the thickness of the layer was large enough to let the crack penetrate into the body material.

A second experiment was performed for further investigation. In this experiment two RBSN bars were placed inside the oven. One bar was encapsulated in an alumina fibre blanket. The other one was placed on an other RBSN bar. This second one was not in contact with any alumina. These bars were heated at 1673 K during 4 hours. After this time the encapsulated bar was covered with small white droplets. These were molten alumina fibres. The second bar was covered with a brown layer. This layer contained two large pits, which intruded into the base material. A further discussion of these experiments is given in section 4.8.

After these experiments the lifetime measurements were continued. As a result of the experiments it was decided to minimize the contact area between RBSN bolt and alumina tile or board. The bolts were no longer encapsulated in alumina fibres. In the sixth run it was planned to reach a long lifetime. In this test the tensile stress was kept at a level of approximately 9.7 MPa. At this stress and at a temperature of 1773 K in air one of the bolts failed after 644.000 s at a stress of 14.2 MPa. The other bolt broke during cooling. Both bolts fractured near the bolt head.

In the seventh run the result of the sixth run had to be repeated. The stress was held constant at 9.7 MPa at a temperature of 1773 K. Due to a power failure in the mains of the university the oven cooled down after 4 days. Before cooling down the stress in the bolts was still 9.7 MPa. After detection of the power failure it turned out that both bolts were broken. Again the bolts broke near the bolt head. As had been seen before the bolts break during cooling, perhaps due to cracks formed in the solidifying surface layer.

After runs six and seven another series of long time (100 hours) experiments were carried out to determine, at 1773 K, the reactivity between RBSN of AME versus, Boron Nitride, alumina and RBSN of Elektro Schmelzwerke Kempten. Some of the RBSN test bars were flushed with argon. Details of these experiments are described in section 4.8. The bars that were flushed with argon showed less oxidation than the bars that were tested in air. From this result it was decided to flush the bolts with argon during the following runs.

In the eighth run the load on the bolts was increased. The load was increased stepwise twice a day. This results in an approximation of a quasi static load on the bolts. Run 7 was started with a preload of 9.7 MPa and a temperature of 1773 K. The average load increase velocity was 58 Pa/s. After twelve days the first bolt broke at a stress of 69.7 MPa.

In run nine the stress increase velocity was increased from 58 Pa/s to 116 Pa/s. This run was started at a preload of 9.7 MPa and at a temperature of 1773 K. According to the theory this experiments should last shorter and the failure stress should be higher than in run 7. After eight days the first bolt failed at a stress of 89.7 MPa. The bolt broke again near the bolt head.

Run ten was started with a preload of 9.7 MPa at a temperature of 1573 K. The stress increase velocity was 174 Pa/s. After one day the metal screw-thread teared loose from the RBSN bolt. The experiment was stopped. During cooling the bolt broke near the bolt head.

Run eleven will be the same as run ten. It was started with a preload of 9.7 MPa at a temperature of 1573 K. The stress increase velocity was 174 Pa/s. After 8 days the screw-thread teared loose again. The experiment was stopped. At room temperature the thread was reattached and the experiment was restarted. Because of a hardware failure in the data acquisition computer the experiment stopped after two days. At that time

the stress in the bolt was 35 MPa. The maximum stress in the bolt, during the first part of the run, has been 88 MPa. The bolt broke during the cool down period. This fracture was located near the bolt head.

Run twelve was started at a temperature of 1573 K and with a preload of 6.3 MPa. The stress increase velocity was 95 Pa/s. After $1.106 \cdot 10^3$ s the first bolt failed during adjusting of the load. The fracture was again located near the bolt head, despite of the spring leave system and the ball-and-cup system. The failure stress was 111.0 MPa.

Run thirteen was started at a temperature of 1573 K and with a preload of 6.3 MPa. The stress increase velocity was 164 Pa/s. After $1.175 \cdot 10^3$ s the bolt failed at a stress of 202.0 MPa. Again the fracture was originated near the bolt head.

Run fourteen was started at a temperature of 1573 K and with a preload of 8.8 MPa. The stress increase velocity was 487 Pa/s. After $433 \cdot 10^3$ s the bolt failed at a stress of 211.3 MPa. This time the fracture originated from the saw slit.

Run fifteen was started at a temperature of 1573 K and with a preload of 8.8 MPa. The stress increase velocity was 343 Pa/s. After $660 \cdot 10^3$ s the bolt broke at a stress of 227.0 MPa. The fatal crack originated from the saw slit.

In run sixteen, at a temperature of 1573 K, was started with a preload of 8.8 MPa. The stress increase velocity for this run was 62.3 kPa/s. After 3360 seconds the bolt failed at a stress of 224.0 MPa. The fatal crack was located in the cold part of the bolt, near the metal thread shell. Due to a failure of the spring leaf system a transverse force acted on the bolt at that location.

With an improved spring leaf system run sixteen was repeated in run seventeen. This run started with a preload of 8.8 MPa and a temperature of 1573 K. The stress increase velocity was 59.8 kPa/s. After 4560 s the bolt failed at a stress of 272.8 MPa. The fatal crack was located near the saw slit. On the fracture surface a large (400 μm) natural pore was visible. Clearly visible on the fracture surface was a flat elliptic region around the included pore. The radius of the pore was measured to be equal to 30 μm .

Run eighteen is a verification of run seventeen. It started with a preload of 8.8 MPa at a temperature of 1573 K. With a stress increase velocity of 43.6 kPa/s the bolt failed after

5040 s at a stress of 228.8 MPa. The fatal crack was located at 15 mm away (to the cold side) from the saw slit. Also on this fracture surface a large inclusion (800 μm) was visible.

The bolts from run 19 on had a saw slit radius of 0.03 mm. The starting stress was 8.8 MPa. The oven temperature was 1573 K. With a stress increase velocity of 45.6 kPa/s the bolt failed after 2400 s at a stress of 118 MPa. The crack was located at the saw slit. The bolt failed during reloading of the air cylinder. Before the failure of the bolt it was noted that the ball-and-cup system in the inner tile did not function. After the test it turned out that the ball-and-cup system was completely broken.

Run 20 was started with a preload of 9.8 MPa and an oven temperature of 1573 K. With a stress increase velocity of 49.1 kPa/s the bolt failed after 2820 s at a stress of 138.6 MPa. The bolt broke at the saw slit.

Run 21 was started with a preload of 9.7 MPa and an oven temperature of 1573 K. With a stress increase velocity of 385 Pa/s the bolt failed after $242 \cdot 10^3$ s at a stress of 93.3 MPa. The bolt broke at the saw slit.

Run 22 was started with a preload of 9.7 MPa and an oven temperature of 1573 K. During this run the dynamic load was superposed on the slowly increasing preload. The stress increase velocity of this preload was 48.2 kPa/s. The dynamic load was kept at 10 % of the preload. After 2280 s the bolt failed at a stress of 110 MPa. The crack was located at the saw slit.

Run 23 was started with a preload of 9.7 MPa and an oven temperature of 1573 K. During this run the dynamic load was also applied. The dynamic load was kept at a value of 10 % of the preload. With a stress increase velocity of the preload of approximately 662 Pa/s the bolts failed. Due to a failure of the data acquisition system the failure stress nor the failure time are known precisely. The bolts failed after $101 \cdot 10^3$ s and before $158 \cdot 10^3$ s. The failure stress at these moments was 68.6 MPa respectively 102.9 MPa. The bolts broke at the saw slits.

To acquire more precise information on the failure stress and failure time of the dynamic loaded bolts run 23 was repeated with some bolts that have been used before. In run 24 the preload stress was again 9.7 MPa and the oven temperature was 1573 K. The preload stress increase velocity was 723 Pa/s. The dynamic load was 10 % of the preload. After $159 \cdot 10^3$ s the bolts failed at a stress of 125 MPa. The bolts broke at the saw

slits. The failure stress was higher than expected according to the theory.

Run 24 was repeated in run 25. This run started with a preload of 10 MPa at a temperature of 1573 K. The preload stress increase velocity was 620 Pa/s. The dynamic load was 10 % of the preload. After $151 \cdot 10^3$ s the bolts broke at a stress of 93.7 MPa. The bolts broke at the saw slit. The failure stress is in agreement with the theory.

Samenvatting

Er is een beknopte analyse gemaakt van de eisen aan welke de generatorwanden van een gesloten cyclus MHD generator moeten voldoen. Een van de eisen is dat, om de warmteflux door de wand laag te houden, de binnenwand een hoge temperatuur moet kunnen verdragen. Keramiek kan gebruikt worden als binnenwandmateriaal. Een aantal mogelijk toe te passen keramieken is gepresenteerd. Combinatie van de mogelijkheden van het keramiek en van de eisen voor de wand heeft geleid tot een voorontwerp van een module voor een modulair opgebouwde MHD generatorwand. Een voorontwerp van de module bestaat uit een binnenwandtegel, een isolatielaag, een koellaag en een ondersteuning. De binnenste drie lagen worden door middel van een keramische bout met elkaar verbonden. Van zo'n module is een model gemaakt waarmee de bout als kritiek onderdeel van de constructie op levensduur is getest.

Er is een opstelling gebouwd waarmee de levensduurproeven uitgevoerd kunnen worden. De opstelling bestaat uit een aantal onderdelen met ieder hun eigen specifiek doel. Een oven is gebouwd om het wandelement op "MHD temperatuur" te brengen. Met behulp van een excitator wordt de mechanische belasting op het wandelement nagebootst. Door middel van een rekstrookmeet-huls en een laser-interferometer wordt deze mechanische belasting gemeten. Voor het innemen en het verwerken van de meetgegevens zijn twee computersystemen met elkaar verbonden.

Er is een model opgesteld waarmee de levensduur van de keramische bout berekend kan worden. Alvorens deze levensduur berekend kan worden, moet eerst de spanningsverdeling in de bout bekend zijn. Om deze spanningsverdeling te kunnen berekenen is het nodig om de temperatuurverdeling in de bout te kennen. Voor het berekenen van deze temperatuurverdeling is een thermisch model opgesteld. De mechanische belasting op de bout bestaat uit een wisselspanning gesuperponeerd op een voorspanning. Voor het berekenen van de wisselspanning is een dynamisch model opgesteld. Met behulp van een eindige elementen methode is het nu mogelijk om de spanningsverdeling in de bout te berekenen. Het model waarmee de levensduur van de bout berekend kan worden gaat uit van een bekende relatie ter beschrijving van de langzame scheurgroei in keramiek. Dit model is via een quasi-statisch model uitgebreid tot een dynamisch model. Met dit dynamisch model is het mogelijk om de levensduur van constructie-elementen, die dynamisch belast worden, te berekenen. Ter vereenvoudiging van de dynamische levensduurberekening is een effectieve spanning geïntrodu-

ceerd. De parameters, die de langzame scheurgroei beschrijven, kunnen, volgens het quasi-statisch model, bepaald worden uit de resultaten van proeven waarbij de spanning, op de bouten, langzaam opgevoerd wordt. Er is een spannings-volume-integraal en een spannings-oppervlakte-integraal gepresenteerd, waarmee de toelaatbare spanning in een keramisch onderdeel bepaald kan worden, uitgaande van materiaaleigenschappen en van de kans op falen van dat onderdeel. Voor een generatorwand is de levensduur berekend. Hierbij zijn verschillende constructies met elkaar vergeleken. Tevens is de invloed van materiaaleigenschappen en van een beproevingsmethode op deze levensduur bepaald.

Van een aantal bouten is bij 1773 K de levensduur bepaald onder een mechanische belasting. Aanvankelijk braken vele bouten bij een geringe belasting en op plaatsen waar dat niet verwacht werd. Om de lage sterkte te verklaren werd het keramisch materiaal nader onderzocht op de samenstelling. Twee verschillende oplossingen werden toegepast om de bout op de verwachte plaats te laten breken. Ten eerste werd de zaagsnede (kerf), waarbij de bout moet breken, verdiept en aangescherpt. Ten tweede werden een aantal constructies aan het wand-element toegevoegd, waarmee dwarskrachten op de bout verkleind werden. Uit een analyse bleek dat de buigspanning, in de bout, ten gevolge van deze dwarskrachten, soms groter was dan de aangebrachte trekspanning. Een bladveermechaniek, een kogeloplegging en een kardanische oplegging werden toegevoegd om de dwarskracht te verkleinen. Bij 1573 K en voorzien van deze extra mechanieken braken de bouten bij een hoge spanning en op de juiste plaats. Uit de meetgegevens, van de quasi-statische metingen, werden de scheurgroeiparameters berekend. De levensduur van dynamische metingen vertoonden een grote spreiding rondom de verwachte levensduur.

Dankwoord

Wetende dat niet alle personen genoemd kunnen worden die, bij de totstandkoming van mijn onderzoek en dit proefschrift, van invloed zijn geweest, wil ik toch enkele personen vernoemen.

Ten eerste wil ik prof. Rietjens bedanken voor de mogelijkheid die hij geboden heeft om mij binnen de groep een promotie-onderzoek te laten verrichten. Verder voor zijn objectieve benadering, van het hem vreemde onderzoek, die hij uitstraalde tijdens onze besprekingen.

Prof. Klostermann wil ik bedanken voor zijn wijze adviezen op het gebied van beproevingsmethoden en voor de regelmatige besprekingen over de scheurgroei in keramiek.

Will Balemans en Bram Veeffkind wil ik bedanken voor hun dagelijkse ondersteuning van het onderzoek en Hub Bonné voor zijn technische en mathematische ondersteuning van het onderzoek.

Ad Holten moet ik bedanken omdat hij de diverse computers, met de nodige hulpmiddelen, vrijwel continu aan het draaien heeft weten te houden. Nol van Stratum voor de ondersteuning op elektronisch en werktuigbouwkundig gebied. Loek Baede bedank ik voor zijn hulp bij het optisch gedeelte van de opstelling en Herman Koolmees voor de direkte hulp die hij ten alle tijden leverde. Ad van Iersel voor zijn goede adviezen op kinematisch gebied.

Het wetenschappelijk corps van de groep bedank ik voor het regelmatig willen aanhoren van een voor hun vreemd onderzoek. De rest van de groep bedank ik voor de fijne tijd die ik bij hun heb kunnen doorbrengen.

Verder wil ik bedanken de leverancier van het eindige elementen pakket, voor het gratis ter beschikking stellen van dat pakket. Ik dank ook de diverse groepen van de universiteit waarbij ik regelmatig gebruik heb gemaakt van hun meet- of testapparatuur.

Marleen bedankt voor het maken van de lay-out van dit proefschrift.

Bert.

CURRICULUM VITAE

- 19 februari 1956 geboren te Weert
- juni 1974 diploma Atheneum B,
Bisschoppelijk College Weert
- augustus 1981 doctoraal examen Werktuigbouwkunde
Technische Hogeschool Eindhoven
vakgroep Constructies en Mechanismen
onderwerp: de stabiliteit van de regi-
startie van professionele
kleuren televisie camera's.
- september 1981-
januari 1983 militaire dienstplicht, ROAG aan de
Technische Hogeschool Eindhoven,
onderwerpen: stabilografie, trillingen.
- september 1983-
februari 1984 constructeur bij KOTI borstels,
Weert.
- februari 1984-
augustus 1984 constructeur bij Medical Systems,
Best.
- september 1984-
juni 1992 wetenschappelijk medewerker in de vakgroep
Elektrische Energiesystemen van de facul-
teit Elektrotechniek,
Technische Universiteit Eindhoven.
onderwerp: constructie van MHD generato-
ren.
gevolgd door een promotie onderzoek over
hetzelfde onderwerp.

Stellingen behorende bij het proefschrift van

H.R.M. van Lierop

Eindhoven, 23 juni 1992.

- 1 Gezien het verschijnsel van langzame scheurgroei moeten relatief hoge trekspanningen in langdurig belaste keramische constructies worden vermeden.
(Dit proefschrift, hoofdstuk 5)

- 2 De breedte van een zeer smalle zaagsnede heeft een grote invloed op de gemeten kritische spannings intensiteits factor.
(Pabst, R.F., "Determination of K_{Ic} - factors with diamond-saw-cuts in ceramic materials", Fracture mechanics of ceramics, vol. 2, p. 555-565, Plenum Press, London, 1974.)

- 3 De ontwerper en de gebruiker van een op trek belast keramisch onderdeel zullen moeten wennen aan het feit dat het onderdeel een zekere kans op falen heeft.
(Dit proefschrift, hoofdstuk 3)

- 4 Het verzamelen van materiaalgegevens en het ontwerpen van een constructie kunnen beter in twee verschillende stappen uitgevoerd worden.
(Dit proefschrift, hoofdstuk 1)

- 5 Het feit dat mensen hun voordracht, tijdens een symposium over technische keramiek, omschrijven als 'een verzameling blunders', geeft een indruk over de stand van zaken op keramisch gebied.

- 6 Het wetenschappelijk onderzoek aan universiteiten is vaak een afspiegeling van hedendaagse politieke ideeën. Gezien de korte cyclustijd van deze ideeën is het moeilijk een stadium van gedegen onderzoek te bereiken.

- 7 Er wordt teveel aandacht besteed aan de relatief kleine groep drugsverslaafden in vergelijking met de aandacht die besteed wordt aan de relatief grote groep alcoholverslaafden.
- 8 Het nauwelijks toenemen van de verkeersdrukke, in deze regio, tijdens een treinstaking, geeft aan dat optimalisatie van woon-werkverkeer automatisch verloopt.
- 9 Het begrip spanning wordt door een elektrotechnicus anders ervaren dan door een werktuigbouwkundige.
- 10 De beperkte mogelijkheden tot kinderopvang resulteren in een vergrijzing van de bevolking en in een verspilling van in opleiding geïnvesteerd kapitaal.
- 11 De voortgang van het wetenschappelijk onderzoek kan bevorderd worden door de discriminatie naar geslacht uit te schakelen.